Manipulating and Probing Angular Momentum and Quantized Circulation in Optical Fields and Matter Waves

MANIPULATING AND PROBING ANGULAR MOMENTUM AND QUANTIZED CIRCULATION IN OPTICAL FIELDS AND MATTER WAVES

by

Joseph Daniel Lowney

A Dissertation Submitted to the Faculty of the

COLLEGE OF OPTICAL SCIENCES

In Partial Fulfillment of the Requirements
For the Degree of

DOCTOR OF PHILOSOPHY

In the Graduate College

THE UNIVERSITY OF ARIZONA

2016

THE UNIVERSITY OF ARIZONA
GRADUATE COLLEGE

As members of the Dissertation Committee, we certify that we have read the dissertation prepared by **Joseph Daniel Lowney** entitled **Manipulating and Probing Angular Momentum and Quantized Circulation in Optical Fields and Matter Waves** and recommend that it be accepted as fulfilling the dissertation requirement for the Degree of Doctor of Philosophy.

Date: 15 April 2016

Brian P. Anderson

Date: 15 April 2016

Ewan M. Wright

Date: 15 April 2016

R. Jason Jones

Final approval and acceptance of this dissertation is contingent upon the candidate's submission of the final copies of the dissertation to the Graduate College.

I hereby certify that I have read this dissertation prepared under my direction and recommend that it be accepted as fulfilling the dissertation requirement.

Date: 15 April 2016

Dissertation Director: Brian P. Anderson

STATEMENT BY AUTHOR

This dissertation has been submitted in partial fulfillment of the requirements for an advanced degree at the University of Arizona and is deposited in the University Library to be made available to borrowers under rules of the Library.

SIGNED: Joseph Daniel Lowney

ACKNOWLEDGEMENTS

First and foremost, I would like to thank my advisor, Brian Anderson, for taking me on as a graduate student and for guiding my experimental research over the past several years. Additionally, I would like to thank Ewan Wright, who provided guidance for my nonlinear optics research described in the latter part of this dissertation. I would also like to thank Jason Jones for serving on my committee as well as providing guidance and feedback on all areas of my research. I owe thanks to John Greivenkamp for his guidance as I spent my first year of graduate school prototyping low-coherence interferometers in his lab.

I owe a debt of gratitude to my friends, labmates, and classmates, who in addition to providing friendship and support over the years also taught me a great deal about optics, electronics, programming, and a number of other subjects. Their contribution to my learning has been an essential and immeasurable part of my graduate school education. Without them, I surely would not have made it through.

Most importantly, I owe sincere thanks to my mom and dad, my sisters, Anne and Tedi, and my partner, Kate, for their constant support, love, and patience throughout my academic endeavors.

TABLE OF CONTENTS

TABLE OF CONTENTS – *Continued*

TABLE OF CONTENTS – *Continued*

LIST OF FIGURES

LIST OF FIGURES – *Continued*

LIST OF TABLES

ABSTRACT

Methods to generate, manipulate, and measure optical and atomic fields with global or local angular momentum have a wide range of applications in both fundamental physics research and technology development. In optics, the engineering of angular momentum states of light can aid studies of orbital angular momentum (OAM) exchange between light and matter. The engineering of optical angular momentum states can also be used to increase the bandwidth of optical communications or serve as a means to distribute quantum keys, for example. Similar capabilities in Bose-Einstein condensates are being investigated to improve our understanding of superfluid dynamics, superconductivity, and turbulence, the last of which is widely considered to be one of most ubiquitous yet poorly understood subjects in physics. The first part of this two-part dissertation presents an analysis of techniques for measuring and manipulating quantized vortices in BECs. The second part of this dissertation presents theoretical and numerical analyses of new methods to engineer the OAM spectra of optical beams.

The superfluid dynamics of a BEC are often well described by a nonlinear Schrödinger equation. The nonlinearity arises from interatomic scattering and enables BECs to support quantized vortices, which have quantized circulation and are fundamental structural elements of quantum turbulence. With the experimental tools to dynamically manipulate and measure quantized vortices, BECs are proving to be a useful medium for testing the theoretical predictions of quantum turbulence. In this dissertation we analyze a method for making minimally destructive *in situ* observations of quantized vortices in a BEC. Secondly, we numerically study a mechanism to imprint vortex dipoles in a BEC. With these advancements, more robust experiments of vortex dynamics and quantum turbulence will be within reach. A more complete understanding of quantum turbulence will enable principles of microscopic fluid flow to be related to the statistical properties of turbulence in a superfluid.

In the second part of this dissertation we explore frequency mixing, a subset of nonlinear optical processes in which one or more input optical beam(s) are converted into one or more output beams with different optical frequencies. The ability of parametric nonlinear processes such as second harmonic generation or parametric amplification to manipulate the OAM spectra of optical beams is an active area of research. In a theoretical and numerical investigation, two complimentary methods for sculpting the OAM spectra are developed. The first method employs second harmonic generation with two non-collinear input beams to develop a broad spectrum of OAM states in an optical field. The second method utilizes parametric amplification with

collinear input beams to develop an OAM-dependent gain or attenuation, termed dichroism for OAM, to effectively narrow the OAM spectrum of an optical beam. The theoretical principles developed in this dissertation enhance our understanding of how nonlinear processes can be used to engineer the OAM spectra of optical beams and could serve as methods to increase the bandwidth of an optical signal by multiplexing over a range of OAM states.

CHAPTER 1

Introduction

The studies of nonlinear phenomena for optical fields and for atomic Bose-Einstein condensates (BECs) have developed into broad fields since the first demonstration of second harmonic generation in 1961 [1] and the first realizations of Bose-Einstein condensation in 1995 [2–5]. The two fields, nonlinear optics and experimental Bose-Einstein condensation research, share a broad range of similar properties and in fact an entire field of study known as Nonlinear Atom Optics is dedicated to studying these similarities [6].

In this dissertation I investigate methods to manipulate, model, and measure nonlinear phenomena for both optical fields and BECs. This introductory chapter describes what this research entails.

1.1 Nonlinear wave dynamics

Wave-like behavior has been observed on almost every length scale in the known universe ranging from the quantum mechanical behavior of light and atoms to the recently detected gravitational waves [7]. Furthermore, waves are present in almost every area of physics: statistical descriptions of gases, liquids, and solids, the description of electromagnetism, gravitation, and quantum mechanics all can be interpretted in terms of wave dynamics. The wave equation is

$$\frac{\partial^2 \psi}{\partial t^2} = q^2 \nabla^2 \psi \tag{1.1}$$

where ψ represents an arbitrary field and q represents some proportionality constant. The left hand side refers to a time derivative and the right hand side accounts for spatial variations.

The propagation of electromagnetic fields through a medium in the absence of free charge, free current, and bound current can be described by the electromagnetic wave equation in the following form:

$$\left(\nabla^2 - \frac{1}{c^2}\frac{\partial^2}{\partial t^2}\right)\mathbf{E}(\mathbf{r}, t) = \frac{1}{\epsilon_0 c^2}\frac{\partial^2 \mathbf{P}(\mathbf{r}, t)}{\partial t^2}. \tag{1.2}$$

In this formulation, $\mathbf{E}$ represents the vector electric field, $\mathbf{P}$ represents the polarization density, c is the speed of light and ϵ_0 is the permittivity of free space. The nonlinearity of this wave equation lies in the polarization density, $\mathbf{P}$. Specifically, $\mathbf{P}$ can be expressed in terms of a linear component $\mathbf{P}^{(1)} \propto \mathbf{E}$ and a nonlinear component $\mathbf{P}^{(NL)}$ that can consist of any number of nonlinear terms.

The nonlinear polarization term is attributed to the electromagnetic field modifying the medium, typically a crystal, which then in turn modifies the dynamics of electromagnetic field propagation. In addition to second harmonic generation, a wide variety of other nonlinear phenomena exist including other frequency mixing processes such as parametric amplification, which will be discussed briefly later in this chapter, and self-focusing or defocusing effects, which are mathematically analogous to the nonlinearities in BECs due to inter-atomic scattering contained in the nonlinear parameter of the Gross-Pitaevskii Equation discussed later.

The Klein-Gordon equation serves as a model for relativistic wave dynamics of matter and takes a similar form to the electromagnetic wave equation:

$$\frac{1}{c^2}\frac{\partial^2}{\partial t^2}\psi(\mathbf{r},t) - \nabla^2\psi(\mathbf{r},t) + \frac{m^2c^2}{\hbar^2}\psi(\mathbf{r},t) = 0, \tag{1.3}$$

where ψ represents the complex-valued wave function of a single particle wave, m represents the particle mass, and c the speed of light. In the non-relativistic form, the Klein-Gordon equation reduces to the more well-known Schrödinger equation,

$$i\hbar\frac{\partial\psi(\mathbf{r},t)}{\partial t} = -\frac{\hbar^2}{2m}\nabla^2\psi(\mathbf{r},t) + V(\mathbf{r})\psi(\mathbf{r},t), \tag{1.4}$$

where $V(\mathbf{r},t)$ represents the single-particle potential, which can have both spatial and time dependence. The Schrödinger equation in this form is linear; however, in many-atom systems such as those investigated in this dissertation, the Schrödinger equation often approximates to a nonlinear form,

$$i\hbar\frac{\partial\psi}{\partial t} = -\frac{\hbar^2}{2m}\nabla^2\psi + V(\mathbf{r})\psi(\mathbf{r},t) + Ng|\psi(\mathbf{r},t)|^2\psi(\mathbf{r},t), \tag{1.5}$$

known as the Gross-Pitaevskii equation [8–10] or the nonlinear Schrödinger equation. The nonlinearity in BECs is due to the presence of multiple atoms and inter-atomic scattering, which is characterized in this formulation by the nonlinear parameter g and the atom number N.

The presence of a nonlinear parameter in a wave equation results in a variety of phenomena depending on the type of nonlinearity. In ^{87}Rb BECs for example, the interaction term is repulsive ($g > 0$); however, in other experimental configurations it can take on an attractive ($g < 0$) behavior, which is analogous to self-focusing effects in optical fields resulting from the Kerr nonlinearity. The presence of a strong repulsive nonlinearity in matter waves results in the existence of highly localized quantized vortices, which enables experimental tests of quantum turbulence.

1.2 BEC manipulation and measurement

A single-component scalar BEC's wave function $\psi(\mathbf{r},t)$ is a complex-valued function of position and time. The modulus of the wave function squared, $|\psi(\mathbf{r},t)|^2$, is the probability density and is

perhaps the most easily measured property of the atom cloud; however the phase information of the wave function can not be deduced directly from the probability density. An energetically stable vortex is characterized by a 2π phase winding about an axis in the complex-valued wave function, the existence of which was first predicted by Lars Onsager in 1947 [11] and is one of the most notable features that distinguishes a superfluid from a classical fluid [12, 13]. Superfluid velocity corresponds to the gradient of the wave function's phase and a 2π phase winding corresponds to fluid circulation about an axis. The existence of a 2π phase winding about an axis requires a phase discontinuity at the axis, which forces the axial density to zero in a single-component BEC.

Vortices are of particular interest in studying superfluids and one key reason is their stability; they are topological defects and so they cannot simply vanish through damping mechanisms. They can, however, be destroyed by annihilation with an anti-vortex or by moving to the BEC boundary where the local density approaches zero. Similarly, a single vortex cannot suddenly nucleate in the center of a BEC. On the other hand, vortex-antivortex pairs can be brought into existence in the bulk of a BEC [14],

The mechanisms behind vortex nucleation are an important topic of study for two primary reasons. First of all, knowledge of these mechanisms will serve to improve our understanding of superfluid physics. Second of all, developing the ability to nucleate vortices in a BEC is a step towards engineering an arbitrary wave function in order to study mechanisms involved in a turbulent system's dynamics.

The vortex core, the local density dip at the center of a vortex, makes quantized vortices optically detectable.This is convenient for the study of quantum turbulence, as it allows the position of vortices to be measured, which can help determine the background fluid flow. Quantized vortices have thus been a large area of interest over the past several decades in the field of Bose-Einstein condensation. They were first observed experimentally in 1999 [15]. In 2000 one of the first techniques for forcibly creating vortices by spinning a BEC using a blue-detuned optical barrier was reported [16]. More recently, efforts have been made to characterize and utilize the mechanisms of vortex formation. A method of shedding vortex dipoles off of a barrier moving above a critical velocity has been investigated at length [14, 17, 18]. Additionally, a technique has been developed to nucleate a vortex dipole and use two optical "vortex tweezers" to precisely place the nucleated vortices in predefined positions [19]. Additionally it has been observed that by modulating the intensity of a stationary repulsive barrier vortex dipoles can also be nucleated; however, the physics behind this method are not well understood [20]. In Chapter 4, a new mechanism for imprinting a vortex dipole onto a BEC is investigated numerically and theoretically. Additionally an experimental layout is proposed and prototyped.

An ideal complete measurement of a BEC wave function would fully recover the complex-valued wave function without affecting the BEC's dynamics. Unfortunately, this is fundamen-

tally impossible. Spatial resolution is limited by the physical principles behind optical imaging including the discretized sensor itself, whether it is a CCD, CMOS, or other type of detector. Furthermore, the interaction of the BEC with light is an inherently destructive process; by actively illuminating a BEC sample some fraction of the atoms will always interact with the illumination and thereby undergo a change in dynamics.

The atom probability density, which is measurable through optical imaging methods, is given by the modulus squared of the wave function: $|\psi(\mathbf{r}, t)|^2$. The gradient of the phase $\phi(\mathbf{r}, t)$, on the other hand, corresponds to the local superfluid velocity $\mathbf{v}(\mathbf{r}, t) = \frac{\hbar}{m}\nabla\phi(\mathbf{r}, t)$, and is not as easily measured; however, it is possible with interference measurements to determine phase profiles.

Methods for measuring the shapes of BECs are well established and discussed at length elsewhere [21, 22]. In general, current imaging methods excel at measuring low spatial frequency features of the bulk density profile of BECs without consideration for destructiveness.

In addition to density measurements, extensive work has been done in the field of phase profile measurement. Interference measurements of BECs used to recover phase information were first demonstrated in 1997 [23]. In 1999 the coherence of BECs was measured using Bragg beams in ballistic expansion [24]. The phase dynamics of a BEC can be measured on a chip in an atom Michelson interferometer or in a waveguide Mach-Zehnder atom interferometer [25, 26]. More recently, a Mach-Zehnder atom inteferometry using BECs was demonstrated in microgravity [27]. Several research groups have demonstrated the interference of two BECs separated and later recombined by an optical barrier [28–32]. In Chapter 2 I describe new experimental and analytical methods that we developed for making *in situ* measurements of nonlinear phenomena in BECs with particular attention to quantized vortices.

1.3 Applications to turbulence studies

In addition to the primary goal of studying the physics of superfluid flow and vortex nucleation, the BECs studied here also serve as a medium to study turbulence. A hydrodynamic system is considered turbulent if it has a disordered flow, has energies distributed over a wide range of length scales, has rapid mixing time scales, and for which the time evolution is unpredictable [33]. Put another way, an infinitesimal variation in initial conditions of a turbulent system will result in a completely different time evolution of the system.

When restricted to two rather than three dimensions, the turbulent behavior of a hydrodynamic fluid changes. In particular, energy dissipation at small length scales is inhibited. Consequently, in two-dimensional fluid flow energy tends to transfer to larger length scales, unlike that of a three-dimensional fluid. An interesting consequence of this is the growth of vorticity at large length scales. Using a point-vortex model, Lars Onsager hypothesized that a two dimensional quantum system will exhibit negative temperature states whereby quantized vortices of similar circulation will cluster together [11]. With the appropriate experimental capabilities

to generate arbitrary vortex configurations and to make minimally destructive measurements of vortex locations, new experiments will be able to test Onsager's point vortex model leading to a better understanding of vortex dynamics and energy spectra in two-dimensional quantum turbulence [34, 35].

With the new experimental techniques developed in this dissertation the range of possible studies of two-dimensional quantum turbulence will be expanded, and further developments towards an understanding an quantum turbulence and how it relates to classical turbulence will be within closer reach.

1.4 Modeling nonlinear wave phenomena in optical beams

Some of the most interesting aspects of nonlinear phenomena for matter waves are their analogies to nonlinear phenomena for optical fields. One of the principal differences is that the most commonly discussed nonlinear property for matter waves is a result of inter-atomic interactions or collisions, whereas in nonlinear optics the nonlinearities are the result of interactions with a separate medium, such as a crystal [36]. In Chapters 5 and 6, the nonlinear properties of light are investigated with particular attention to their orbital angular momentum spectra.

Atoms can possess angular momentum in the form of spin angular momentum and orbital angular momentum. The ability of atoms to possess angular momentum is relatively intuitive in the sense that as humans we interact with rotating bodies of mass on a daily basis. Less intuitive is that angular momentum is quantized. Perhaps even less intuitive is that light can also possess quantized angular momentum [37]. It was hypothesized early on that the circular polarization of light is related to the angular momentum of light [38]. In addition to angular momentum due to the circular polarization of light, which can also be referred to as spin angular momentum, light beams possess a quantized orbital angular momentum corresponding to the azimuthal phase winding $e^{i\ell\theta}$, where θ represents the azimuthal angle in position space and comes in discrete units specified by an integer, ℓ. The first mechanical measurement of angular momentum of light was in 1936 [39]. More recently in 1979, the helical wavefront of a beam with orbital angular momentum was measured using optical interference techniques [40]. In the work described in Chapters 5 and 6 I develop techniques for engineering the OAM spectra of optical beams by exploiting the nonlinear optical properties of crystals.

CHAPTER 2

In situ detection of vortices in Bose-Einstein condensates

2.1 Introduction

The goal of the work described in this chapter is to develop methods to make *in situ* observations of quantized vortices and other high spatial frequency features in BECs with particular attention to minimally destructive measurements. Minimally destructive methods of *in situ imaging* are even more challenging because the atom-light interaction affects the dynamics and also induces atom loss. Historically, most vortex detection methods have been completely destructive and executed after ballistic expansion [14–16, 41–47]. Vortices were first observed in Bose-Einstein condensates in 1999 using two-component BECs where the atoms of one component were used to fill the vortices, causing the vortex core radius to increase in size up to a factor of 13 at which point the vortex core size, which would otherwise be on the order of $0.25\mu m$, is large enough to be optically imaged *in situ* [15].

Until recently, the positions of bare vortices in a single-component BEC had not been observed *in situ*. Instead, it was necessary to first expand the condensate in order to make the vortices visible, and in doing so, immediately halt its dynamics. This destructive imaging technique typically limits measurements to one image per condensate. One method developed to record the dynamics of bare vortices is to transfer a small fraction of atoms into an untrapped state where they are permitted to ballistically expand and then be imaged optically while the remaining atoms remain trapped [48]. While this method permits sequential non-destructive measurements of the locations of vortices, it still relies on an expansion of the atoms imaged. The disadvantage of this technique is that the expansion dynamics do not necessarily reproduce the trapped BEC vortex distribution, especially in the case of annular or flat-bottom traps. Furthermore, the vortex core size expands more rapidly than the bulk BEC geometry, potentially reducing the imaging system's ability to resolve and differentiate nearby vortices. More recently, it has been demonstrated that *in situ* phase information can be retrieved from a BEC using magnon interferometry with high enough fidelity to make minimally-destructive measurements of the location and circulation of a vortex in a BEC [49]. This impressive technique permits minimally-destructive *in situ* measurement of vortex locations; however, this method requires an all-optical trap with multiple atomic components. Vortices are located by analyzing interference fringe patterns which could become extremely difficult or impossible for larger numbers of vortices, as is the case for a turbulent BEC.

This chapter describes new methods to image BECs, developed to better characterize vortex dynamics and fluid turbulence, specifically the dynamics of vortices in BECs exhibiting two-dimensional quantum turbulence. The ability to detect and locate vortices in particular is relevant to the understanding of vortex formation [14], two-dimensional quantum turbulence [50, 51], persistent current formation [52–54] and also the Berezinskii-Kosterlitz-Thouless transition [55–57]. A new imaging system is described that permits the real-time imaging of a BEC's fluid dynamics. This new imaging system has enabled real time *in situ* observation bare vortices in Bose-Einstein condensates. The primary benefits of this system are its ability to make *in situ* measurements that do not require ballistic expansion and a spatial resolution that is good enough to resolve very large numbers of vortices, in some instances up to fifty — while still being only partially destructive and permitting multiple images of the same condensate and vortices. The imaging system presented here, and demonstrations of in situ imaging of vortices in BECs, were described in depth in the PhD dissertation of Kali Wilson [58]. This chapter focuses on presenting a new detailed quantitative examination of image quality, image noise factors, and the signal-to-noise ratio that can be expected with in situ imaging of vortices.

The *in situ* imaging of bare vortices in a BEC has proven to be a challenging task. This is particularly true because it is necessary to distinguish between multiple vortex cores, each appearing as density dips in the BEC cloud with a sub-micron diameter and separated by several microns. Furthermore, the BEC is observed by illuminating the atoms with a near-resonant light source, a destructive process, necessitating the use of short exposure times and low illumination power. The remainder of this chapter describes the basics of atom-light interaction, imaging of cold atoms, and then delves into the specifics of the various imaging techniques used to make minimally destructive *in situ* measurements of vortex locations. The methods described here were ultimately capable of taking up to six sequential images of the same BEC with vortex visibility in all images. Not without limitation, these new imaging methods still affect the BEC dynamics by removing atoms from the cloud with every image, vortex circulation is not immediately known, and the maximum image number is limited to about six in its current form. With the advancements discussed in this work in addition to efforts currently underway aimed at developing a BEC lab with the specific intent of vortex studies, new experimental tests of 2D quantum turbulence will be possible [34, 59–61].

2.2 Optical properties of atoms

A ground-state BEC created with atoms having repulsive interatomic interactions confined in a harmonic trap takes on a parabolic density profile. In the case of the University of Arizona BEC lab, which uses ^{87}Rb atoms, cylindrically symmetric harmonic traps are typically used.

Accordingly, the three-dimensional density profile is described by

$$D(r,z) = \max\left[D_0\left(1 - \frac{r^2}{r_0^2} - \frac{z^2}{z_0^2}\right), 0\right]. \tag{2.1}$$

Three terms have been introduced: the peak density D_0, the radial Thomas-Fermi radius r_0, and the axial Thomas-Fermi radius z_0.

Both the dispersive and the absorptive nature of an atom cloud can be exploited for the purpose of imaging and measurement and so a complex index of refraction is considered. For simplicity and the sake of qualitative understanding, we consider a two-level atom in the regime where the real index of refraction is approximately one and the intensity[1] I is much less than the saturation intensity I_{sat}. In this limit,

$$n = n_r + in_i = 1 + \frac{\sigma_0 D(x,y,z)\lambda}{4\pi}\left(\frac{i}{1 + 4\Delta^2/\Gamma^2} - \frac{2\Delta/\Gamma}{1 + 4\Delta^2/\Gamma^2}\right), \tag{2.2}$$

where σ_0 is the resonant atom-photon scattering cross-section and $\lambda = 780$ nm is the atomic resonance.

In the above formulation, $D(x,y,z)$ represents the atom density profile, Δ is the detuning of the probe light from resonance, and Γ is the natural linewidth. In the context of a single-axis imaging system, the full three-dimensional density profile can not be directly recovered; however, with this two-dimensional projection and knowledge of the harmonic trap geometry, a three-dimensional reconstruction of the bulk BEC geometry can be recovered.

In order to analyze the atom-light interaction, I assume a coherent illumination source propagating along the axial (z) direction of the BEC with intensity $I_0(r)$ corresponding to an electric field $E_0(r)$. In practice, the beamfront will have a gaussian profile but for now I assume the beam is large enough such that any spatial variations in intensity can be ignored. In general for a homogeneous medium the electric field varies as

$$E(r,\theta,z,t) = \Re\left\{E_0(r,\theta,z,t)e^{i(2\pi(n_R+in_I)z/\lambda_0 - \omega t}\right\}, \tag{2.3}$$

and the BEC applies a transmission and phase mask to the illumination field,

$$E = \Re\left\{E_0 \exp\left[-\frac{\sigma_0}{2}\frac{1}{1 + 4\Delta^2/\Gamma^2}\tilde{D}(r,\theta)\right]\exp\left[-i\frac{\sigma_0}{2}\frac{2\Delta/\Gamma}{1 + 4\Delta^2/\Gamma^2}\tilde{D}(r,\theta)\right]\right\}, \tag{2.4}$$

where

$$\tilde{D}(r,\theta) = \int_{-\infty}^{\infty} D(r,\theta,z)dz \tag{2.5}$$

is the column density of the atom cloud [21, 22].

The BEC applies a spatially dependent transmission $t = \exp\left[-\frac{\sigma_0}{2}\frac{1}{1+4\Delta^2/\Gamma^2}\tilde{D}(r,\theta)\right]$ and phase mask $\phi = \frac{\sigma_0}{2}\frac{2\Delta/\Gamma}{1+4\Delta^2/\Gamma^2}\tilde{D}(r,\theta)$ to the field where the intensity scales as $I(r,\theta) = I_0|t(r,\theta)|^2$. It is convenient to define the intensity transmission, $T = |t|^2$, and the optical depth, $\mathcal{D} = -\ln(T)$.

[1] Intensity refers to a quantity with units of power per unit area.

2.3 Image quality

There are countless ways to evaluate the quality of an image. In the context of typical cold atom experiments, key metrics could be dynamic range, spatial resolution, and signal-to-noise ratio (SNR). In the case of making minimally destructive *in situ* measurements of vortex locations in BECs, the most relevant metrics could be anything having to do with the system's ability to non-destructively measure vortex location.

I consider three primary metrics: (1) The resolution of the system dictates how close two vortices can be while still being able to separately identify them. The target resolution will be on the order of 2μm, which was found in studies of 2D quantum turbulence to be a characteristic length scale for vortex separation in BECs similar to those studied in our lab [35]. (2) The signal-to-noise ratio (SNR) is another important metric. While the resolution dictates how near two objects can be, the SNR dictates how easy it is to identify a single vortex. (3) A final metric for image quality is the destructiveness of the measurement, which can be characterized as what fraction of the atom number remains after a measurement. A completely nondestructive measurement would have 100% atoms remaining, whereas a completely destructive measurement would have 0% atoms remaining.

2.3.1 Imaging system

The primary imaging system used in these studies consists of a custom imaging objective optimized for 780 nm transmission [58] . The objective's transmission is approximately 88% at 780 nm. The numerical aperture is 0.26. One of the most unique features of this objective is the long working distance of 35.6mm. This is an extraordinarily long working distance for a typical microscope objective and was necessitated by the configuration of the magnetic coils around the BEC cell. The focal length of the imaging objective is 36.7 mm. The theoretical diffraction-limited resolution is 2.2 μm. The custom objective was ordered from Lens-Optics in Germany for approximately 1299 USD.

A layout of the imaging configuration is shown in figure 2.1. Not shown is the 400 mm tube lens and the camera downstream. Additionally a flip mirror is located after the tube lens that is used to select either a Princeton Instruments PIXIS 1024 BR or a Photometrics Cascade 512B EMCCD camera for imaging [62, 63].

A collimated beam of near-resonant or detuned light is directed upwards with a gaussian beam radius of approximately 2 mm. The polarization of this light can be chosen to be circularly or linearly polarized. A half-wave plate (HWP) before the BEC cell is used to further select the angle of linear polarization. The beam propagates through the BEC cell and the BEC itself before entering the objective lens. At the rear focal point behind the objective there is an optional dark field (DF) mask, which is simply an absorptive central obscuration with diameter ranging from

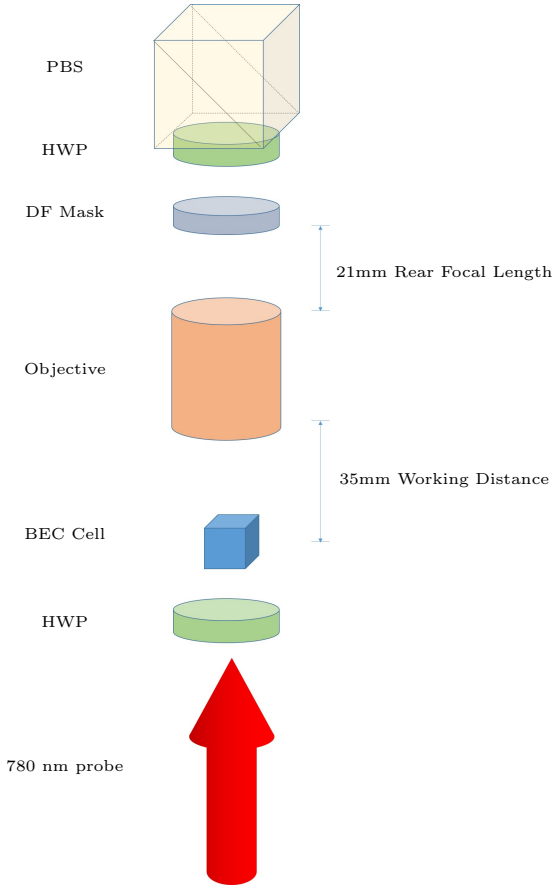

Figure 2.1: This figure illustrates a scale diagram of the imaging system not including the downstream tube lens (400mm) and camera.

400 μm to 1.2 mm. After the optional dark field mask, an additional half wave plate is used to optionally rotate the linearly polarized light before reaching a polarizing beam splitter (PBS) cube. The utility of the polarizing beam splitter cube and the half-wave plates will become clear later in this chapter in the section describing Faraday imaging.

2.3.2 Noise sources

Cold atoms, whether a thermal cloud or a BEC, can be be optically imaged, and based on fitting algorithms, the resulting image can be fit to either a BEC profile (typically Thomas-Fermi) or a thermal cloud profile. With knowledge of the trapping geometry, the only free parameters in the fitting algorithm are the thermal cloud radii, the Thomas-Fermi radii of the BEC, and the relative optical depth of the thermal and BEC components of the cloud. This information can be used to calculate the atom number and atom temperature. Vortices themselves are two orders of magnitude smaller than the Thomas-Fermi radius: their width is on the order of the

healing length of the BEC, about 0.3 μm. Until recently, the primary method for imaging vortices was to first ballistically expand the BEC, during which time the vortices rapidly expanded in size, and then image the expanded atom cloud and expanded vortex cores. While this method can permit the detection of quantized vortices, it is not without limitations. First, the expanded BECs are not necessarily self-similar during expansion, meaning, the expanded BEC and vortex distribution is not necessarily a simple magnification of the *in situ* BEC and vortex distribution. Expansion is not self-similar when BECs are suddenly released from anharmonic traps such as flat-bottom traps [64] and toroidal traps [50], which are both of particular interest in studies of two-dimensional quantum turbulence. Second, the process of ballistic expansion of the entire BEC is completely destructive, whereas minimally destructive *in situ* vortex imaging can be used to capture multiple frames of vortex dynamics.

Signal-to-noise ratio (SNR) is a useful measure for the quality of any signal to be measured and the utility of SNR extends to CCD imaging measurements. In the BEC apparatus, a CCD camera is used to detect photons; this is the main form of optical measurement used in the laboratory. Therefore, a brief overview of the noise sources is provided.

With any CCD imaging sensor, there are three principle noise sources: photon shot noise, readout noise, and dark noise. As will be shown in the following subsections, different noise sources will dominate depending on the imaging technique and requirements of the BEC laboratory. This criteria drives the choice of camera, as will be discussed later in this section.

Shot noise

Shot noise is a consequence of the discretization of both light (in the form of photons) and electric charge (in the form of electrons). Such a noise source boils down to known physical laws and for the purposes of this research, it is assumed that it cannot be eliminated [65]. The specific consequence of shot noise is that, if a given light burst corresponding to N_p photons incident on a detector, if repeatedly measured there will be a Poissonian distribution of photon detection events. For larger photon numbers, the distribution will become Gaussian with standard deviation $\mathcal{N}_{SN} = \sqrt{N_e} = \sqrt{N_p \eta}$, where N_p is the number of photons incident on the pixel and η represents the detector's quantum efficiency. For a shot-noise dominated system the SNR scales with the square root of the average number of photons detected: $\text{SNR} = \eta N_p / \sqrt{\eta N_p} = \sqrt{\eta N_p}$. The absolute shot-noise level increases with signal level and becomes the dominant noise source for high signal levels, because as will be seen next the two other primary noise sources in CCD detection do not scale with signal level. When multiplication gain is used, the shot noise level approaches $\sqrt{2N_e}$ rather than $\sqrt{N_e}$ for high gain [66].

Readout noise

The next noise source of concern is readout noise. After the photon-to-electron conversion, the electrons are counted using an analog-to-digital converter (ADC). This process is not perfect and acts as an additional noise source. The read noise, $\mathcal{N}_{\mathrm{RO}}$, is typically a flat amount independent of signal level. Therefore, it tends to dominate at low signal levels. The Princeton Instruments camera has two different readout speeds: 100 kHz and 2 MHz. At the high readout speed, 2 MHz, the read noise is specified to be 9 electrons. By using the slower readout speed, 100 kHz, the read noise is reduced to 3 electrons rms. Note, however, that for a 1024 x 1024 array, 100 kHz readout would require a ten second readout, whereas the readout is approximately 600 milliseconds at 2 MHz.

Dark noise

The final form of noise introduced by any CCD camera is dark noise. In the absence of light on a CCD detector, there is still some amount of electrical current that is produced due to the random generation of electrons and holes in the depletion region of a pixel's P-N junction. This is referred to as dark current, I_{dark}, and is typically given in units of rms electrons per pixel per second. In its nominal operation, the CCD integrates current generated by the photodetector. Unfortunately, there's no easy way to separate out the current associated with photon detections from this dark current. A consequence of this, then, is that each pixel will collect an additional amount of charge or number of electrons, $N_{\mathrm{dark}} = I_{\mathrm{dark}}\Delta t$, where Δt is the exposure time. The dark current is the same in every frame, so a secondary frame with the shutter closed can be taken and then subtracted off from the main image. As with shot noise, the accumulation of dark charge is a statistical process with a Poissonian distribution and introduces an additional noise source known as dark noise: $\mathcal{N}_{\mathrm{Dark}} = \sqrt{I_{\mathrm{dark}}\Delta t}$. By cooling the PIXIS 1024 BR's sensor down to -70 degrees C, the sensor's dark current is reduced to be $I_{\mathrm{Dark}} = 0.02$ rms electrons per pixel per second. The sensor's quantum efficiency is lower at lower temperatures. Our typical camera exposure times are on the order of 10 milliseconds. Our dark noise is computed to be $\mathcal{N}_{\mathrm{Dark}} = \sqrt{0.02\ \mathrm{sec}^{-1} \times 10^{-2}\ \mathrm{sec}} \approx 0.01$ electrons per pixel rms. This noise level turns out to be two orders of magnitude lower than readout noise and shot noise when any appreciable signal is present and furthermore it is far below the quantization value of one electron and therefore is negligible in this case. For scientific experiments requiring much longer exposures, as is the case for astronomical observations, dark current can be a dominant noise source.

Dark noise is negligible at the operating temperature of the CCD for our exposure times in both the case of a Photometrics Cascade 512B and a Princeton Instruments PIXIS 1024. In principle, because the temperature is significantly lower than it needs to be for our applications, the system performance may be increased by raising the CCD temperature slightly to improve

quantum efficiency.

Noise level prediction

The CCD detection is subjected to three noise sources. The total noise level is computed by summing the individual noise sources in quadrature, the least of which, dark noise, is negligible:

$$\mathcal{N}_{\text{tot}} = \sqrt{\mathcal{N}_{\text{Shot}}^2 + \mathcal{N}_{\text{RO}}^2 + \mathcal{N}_{\text{Dark}}^2} \approx \sqrt{\mathcal{N}_{\text{Shot}}^2 + \mathcal{N}_{\text{RO}}^2}. \tag{2.6}$$

The relative readout noise levels for the cameras available in the lab are shown in table 2.1. The Cascade 512B can achieve effective readout noise levels of less than 1 e- when EM gain is enabled. This capability proves useful for minimally destructive *in situ* detection of vortices.

Camera	Readout	Noise
PIXIS 1024BR	100 kHz	3 e- RMS
PIXIS 1024BR	2 MHz	9 e- RMS
Cascade 512B	1 MHz	< 1 e- RMS (effective)

Table 2.1: Noise levels specified by manufacturer for Photometrics Cascade 512B and Princeton Instruments PIXIS 1024 BR Cameras [62, 63]

Minimizing noise

The effect of photon shot noise is minimized by increasing the photons incident on each pixel. In the scenarios described here, this is done primarily by increasing the system quantum efficiency, exposure time, or illumination intensity. With the exception of quantum efficiency, these other parameters all necessitate more photons interacting with the atom sample — in other words, this corresponds to an increase in destructiveness.

Readout noise is a fundamental property of the analog signal chain including the analog-to-digital conversion process. In the case of our apparatus, this is effectively eliminated through the use of electron multiplying (EM) gain; however, high EM gain will increase the photon shot noise by a factor of up to $\sqrt{2}$ [66] and so it is only advantageous to use EM gain when readout-noise limited.

Dark noise is effectively eliminated by using a very short exposure time and actively cooling the CCD sensor to -50 deg C in the case of the Photometrics Cascade or -70 deg C in the case of the Princeton Instruments PIXIS.

The remaining noise is dominated by photon shot noise. For simplicity, we consider a system with only photon shot noise and assume high EM gain. In this scenario, for a given pixel and exposure, the pixel collects N_e electrons, has a noise level of $\sqrt{2N_e}$ and a SNR of $\sqrt{N_e/2}$ assuming

high multiplication gain. Fundamentally, the only way to increase the SNR in this system is to increase the total electron count per pixel. Under these constraints, this can be done by improving the QE, increasing the fill factor, or by increasing the pixel size in general.

The PIXIS camera has a 100% fill factor [62]. The fill factor of the Cascade camera is unknown but is assumed to be on the order of one, which is typical for scientific cameras. The temperature of a CCD can be increased slightly to improve the quantum efficiency since dark current is not a limiting factor [67].

2.3.3 Image subtraction and noise

Frequently in absorption imaging three images are taken. The shadow image of the atoms with N_S electron counts on a given pixel, the background image with N_I counts on the pixel, and the dark image with N_D counts.[2] The transmission corresponding to that pixel is calculated as

$$T = \frac{N_S - N_D}{N_I - N_D}. \tag{2.7}$$

The optical depth[3] is calculated to be

$$\mathcal{D} = -\ln(T). \tag{2.8}$$

Typically, it is the final result $\mathcal{D}$ that is inspected to analyze the BEC. In this case, the atom signal itself is contained in the first frame. This image is subjected to noise. The noise in this frame can be estimated as $\mathcal{N}_S = \sqrt{\mathcal{N}_{\mathrm{RO}}^2 + \mathcal{N}_{\mathrm{S,SN}}^2} = \sqrt{\mathcal{N}_{\mathrm{RO}}^2 + (N_S - N_D)}$, in the absence of stray light. The background image will have an additional noise level, $\mathcal{N}_I = \sqrt{\mathcal{N}_{\mathrm{RO}}^2 + \mathcal{N}_{\mathrm{I,SN}}^2} = \sqrt{\mathcal{N}_{\mathrm{RO}}^2 + (N_I - N_D)}$. The dark frame will only contain readout noise: $\mathcal{N}_D = \mathcal{N}_{\mathrm{RO}}$.

Image subtraction – particularly when illumination is highly nonuniform and high spatial frequency artifacts are present in the illumination beam – proves useful. Furthermore, it is necessary to accurately quantify the transmission, optical depth, and atom column density. However, for very low signal-to-noise environments such as minimally destructive imaging of vortices *in situ*, the additional noise acquired from performing image subtraction is at times significant enough to obscure the vortex signal.

One potential solution to this problem that would allow numerically accurate post-processing without adding additional noise that has not been tried. A background frame could be taken with a much longer exposure time increased by a factor β to improve the SNR and the signal could then be divided by the same factor β to provide a time averaged background frame. Increasing the exposure time will only hurt the dark frame; however, a large number of dark frames could

[2] From here forward I assume the camera gain to be 1 count per electron.

[3] Optical depth uses a base e logarithm and differs from optical density, which uses a base 10 logarithm.

be taken and an averaged dark frame could then be used to reduce dark frame noise. One disadvantage of this approach is that air currents could blur out high spatial frequency features in the background image, introducing artifacts into the processed data.

This source of noise may seem like a minute detail; however, it was not obvious at first that our data contained signatures of vortices because we defaulted to looking at the post-processed data. Upon inspection of the raw data, it was clear that there were vortices in the images.

2.4 Stray light

Stray light is an umbrella term that accounts for any photons that are incident on the photodetector that are not directly due to the object being imaged or the direct imaging light. Stray light can be a problem for a variety of reasons. If the stray light level is extraordinarily high, the gain will have to be turned down on the camera and the dynamic range of the data could be severely compromised. Stray light could also destructively interact with the BEC by causing atom loss or changing the superfluid dynamics. Lastly, stray light can add unwanted signal to the images and must be properly subtracted off. Furthermore, image subtraction only removes the mean stray light level and cannot subtract off noise due to stray light.

In the previous section, a brief overview of noise sources was given and the noise level in a signal frame was found to be

$$\mathcal{N}_{\text{tot}} \approx \sqrt{\mathcal{N}_{\text{SN}}^2 + \mathcal{N}_{\text{RO}}^2}. \tag{2.9}$$

Stray light contributes to the term $\mathcal{N}_{\text{SN}}$ and proves to be non-negligible in the system, particularly when trying to observe weak signals such as those arising form vortex cores.

2.4.1 Stray light sources

Stray light in the BEC imaging system can be attributed to at least four different sources. First of all, ambient light from the room can leak in through holes in the enclosure. A well designed enclosure will minimize this. Second of all, some percentage of the imaging light that we intend to use will always scatter off of optical defects, dust, and residual reflections from transmissive optics. For this reason, it is important to use anti-reflection coated surfaces whenever possible and to keep optical surfaces in the imaging path as clean as possible. Thirdly, the 1090-nm optical trapping beam has the potential to scatter off of optical elements. Lastly, when in use, the 660-nm and 850-nm laser beams can also scatter off of optics and send unwanted stray light to the camera sensor. The amount of stray light is difficult to predict accurately because most of the stray light is the result of difficult-to-quantify misalignments, defects, and contaminants.

The camera exposure time is typically set to around $\Delta t_{\text{CCD}} \approx 10$ msec which permits timing jitter for shutters to open and close as well as the illumination source to turn on and off. The illu-

mination itself, the near-resonant light that illuminates the BEC, is typically enabled for around $\Delta t_{\mathrm{AOM}} \approx 10\ \mu$sec. Because the CCD exposure time is three orders of magnitude longer than the illumination light, light sources other than the illumination beam can be especially problematic. A stray light source that is continuously on will be active for the duration of the camera exposure. Furthermore, the illumination beam itself is very low power — on the order of 100 μW, whereas the power in the 1090-nm trapping laser, for example, is on the order of 100 mW or 1 W. Thus the total optical energy entering the enclosed system due to the trapping laser over the course of one camera exposure can be six orders of magnitude larger than the energy in the illumination beam itself and if 1 part in one million of this optical power is scattered onto the CCD there could be significant image quality degradation. It is therefore essential to ensure that the 1090-nm trapping beam is properly aligned and properly baffled; even a beam block could scatter a significant amount of light onto the imaging sensor.

Another source of stray light is the optical stirring beams which are brought to focus at the BEC in order to manipulate atoms and thus are also refocused at the image plane. These beams are attenuated with a bandpass filter. Prior to 2016, the filter in use had an optical density of 3, corresponding to a 1000X attenuation. While this is a very large attenuation, the camera will be exposed to this beam for 1000X longer than the illumination beam if they remain on during the imaging sequence, and so it is not sufficient attenuation. Recently, an additional filter was put in place and should serve to nearly completely eliminate stray light due to the optical stirring beams. A total optical density of about 6 should be used to attenuate stirring beams in the imaging path if their intensity is on the order of the illumination intensity.

There are two sources of photons incident on the detector: signal photons and stray light photons. Only the signal photons contribute to signal level. In a typical imaging sequence, the first image is taken with the atoms illuminated, the second image is taken with the illumination on but no atoms present, and the third image is taken without the illumination source. In order to account for stray light photons, if a light source such as the 1090 nm, 660 nm, and 850 nm perturbing lasers must be enabled during the first image, it should also be left on during both the background frame (in the case of absorption imaging) and the dark frame — otherwise the stray light will cause the atom density to appear lower than it actually is. This is particularly evident if a beam is left on during the absorption and background image but turned off during the dark frame — with the post-processing algorithms this will be interpreted as illumination light that is transmitted through the cloud and therefore suggest that the local density is very low. By imaging the stray light source in the dark frame as well, this light is not interpreted as transmitted illumination light and the measurement will be more accurate quantitatively.

2.4.2 Dark frame subtraction

The third image of the imaging sequence is essential for two reasons. It serves to measure the illumination intensity by subtracting off the bias. Secondly, the bias varies over the course of a day and this third frame serves as a means to measure the bias for a given image.

The CCD sensor has a 16 bit analog-to-digital converter. Accordingly, it bins the analog voltage into 65536 different digital levels at each pixel. During the collection of a bias frame, there is zero exposure time: no dark current is integrated and no photons are captured. The collected charge (zero) is converted by the camera electronics to an analog voltage. During the conversion process, a nonzero DC voltage offset is added before conversion to digital counts. This results in the bias counts. In both the Princeton Instruments camera and the Photometrics Cascade camera, the DC offset corresponds to approximately 500 counts. This DC bias requires a loss of dynamic range: 500 levels of the 65536 are now dedicated to measuring the offset. However, this represents a less than one percent loss in dynamic range. In principle and under ideal operating conditions, the bias should not vary over the course of the day. Due to environmental fluctuations, however, the bias voltage does drift. For this reason, a dark frame is captured with every data point in the experiment. This improves the overall SNR.

Originally, only one camera was used in making our BEC measurements: the Princeton Instruments PIXIS 1024BR. The recent introduction of a second camera into the apparatus enclosure raised the ambient ambient temperature to about 79 degrees Fahrenheit which caused the the bias counts on the Princeton Instruments camera to vary significantly throughout the day.

2.5 Noise vs spatial resolution

Ideally, an imaging system will have both unlimited resolution and infinite SNR. In practice, however, this is far from the case. In fact, the two metrics will often compete with each other. The SNR can be increased at the expense of spatial resolution and vice versa.

An increase in pixel size will typically improve the SNR of an imaging system; however, this is not without tradeoff. So far, emphasis has been placed entirely on SNR and spatial resolution has been mostly ignored. The number of electrons collected scales with the square of the pixel pitch – assuming constant fill factor. The SNR, which scales with the square root of the electrons collected, scales linearly with pixel pitch, δx (again assuming constant fill factor). The cost being that the spatial Nyquist frequency — the frequency above which a signal cannot be accurately registered without aliasing — scales as $f_N = 1/2\delta x$ in image space.

The subject of resolution is an important one, and the system's design parameters determine how necessary spatial resolution is. In the cases studied here, the bulk BEC geometry is approximately 100 μm wide. Bulk BEC measurements could in principle be made with as few as two or three samples across the spatial extent of the BEC in order to fit data to the Thomas-Fermi profile

per the Shannon-Nyquist sampling theorem [68–71]. However, it is of interest to detect vortex cores. With a BEC healing length of approximately $\xi \approx 0.3\mu$m, the diameter of a vortex can be approximated as twice the healing length, $2\xi \approx 0.6\mu$m.

It is important to distinguish between detecting a feature, measuring the structure of a feature, and distinguishing one feature from another. The easiest task is to detect an object. It is more difficult to distinguish two nearby objects from each other. And it is generally even more difficult to measure the internal structure of a small feature. Because it is prohibitively difficult to measure the structure of a vortex core at this point in time, in this study we limit our goals to detecting vortices and to distinguishing neighboring vortices. This goal raises two questions: is there an optimal pixel size and magnification combination for detecting a single vortex and is there an optimal pixel size and magnification combination for detecting a vortex pair separated by a distance d, and what separation distance d is relevant?

Based on experimental measurements and images after ballistic expansion, it appears that vortices are statistically typically at least several healing lengths apart. Vortex-antivortex pairs are increasingly lower energy as their separation decreases. For smaller separation there will also be less dipolar fluid flow and ultimately for small enough vortex-antivortex separation they collide and annihilate. Neely *et al* identified numerically a vortex dipole separation of approximately 6.7ξ to be a lower bound for vortex dipole self-annihilation in their experimental configuration [35]. On the other hand, vortices of similar circulation are increasingly higher energy as their separation is reduced.

If a single vortex core is estimated as being a point source in an imaging system there is actually no resolution requirement for single vortex detection. This is similar to how the existence of a single star in the night sky could be detected by a single-pixel-detector with a wide field-of-view lens. Thus, for single-vortex detection, there is no lower limit for the necessary Nyquist frequency. On the contrary, in order to distinguish two point sources, they must be at least a distance of $1/f_N$ apart, where f_N is the spatial Nyquist frequency. For the sake of choosing a Nyquist frequency on a relevant length scale, one could specify the Nyquist frequency based on the findings of Neely [35]. I define the lower bound of vortex dipole distance to be $d_{\mathrm{VD}} = 6.7\xi$ and assume a system with magnification M. The point separation in image space is then Md_{VD} and the Nyquist frequency will be chosen such that $1/f_N = Md_{\mathrm{VD}}$.

The numerical aperture is essentially limited based on geometrical constraints of the apparatus. The magnification of the system can be chosen to match the diffraction-limited spot size in image space to correspond to the sensor Nyquist frequency. The spatial resolution of a diffraction-limited objective lens is $d = 0.61\lambda/\mathrm{NA}$ where $\mathrm{NA} = D_{\mathrm{EP}}/f$, D_{EP} is the entrance pupil diameter, and f is the objective focal length. This distance d refers to the radial distance from an imaged point source corresponding to the first zero of the Airy pattern in object space. In image space, this resolution is magnified to $d_M = M0.61\lambda/\mathrm{NA}$. For our system, the magnification is $M = 11$

and the numerical aperture is NA = 0.26, thus the resolution limit in object space is 1.83 μm and the resolution limit in image space is 20.1 μm. Ideally, magnification is chosen such that the resolution limit is equal to twice the pixel pitch. In this apparatus, two cameras are used: occasionally the PIXIS with $x_p = 13$ μm is used with this imaging system, but primarily the Cascade with $x_p = 16$ μm is used. Twice the pixel pitch corresponds to 26 μm or 32 μm respectively, which suggests that the detector is undersampling the resolution limit in the case of our system. In general, a theoretical ideal magnification for a given sensor size and numerical aperture is given by:

$$M_I = \frac{2x_p \,\mathrm{NA}}{0.61\lambda} \approx 17.5. \tag{2.10}$$

This magnification is ideal in the sense that any higher magnification will not produce higher resolution because the system is diffraction-limited at this point. For particular applications, a lower magnification may be desirable in order to increase SNR. In either case, the magnification can be easily corrected without modifying the objective by exchanging the 400 mm tube lens for a 630 mm tube lens, for example.

2.6 Absorption imaging

2.6.1 Overview

The most straightforward method of imaging a BEC is on-resonant or near-resonant absorption imaging. This standard method requires taking three images: first a transmission image is taken of the BEC. The BEC is illuminated only briefly, $\sim 10\mu$sec, with a laser beam of intensity $I(x, y)$. Because the coherent illumination contains ringing features and intensity fluctuations due to diffraction from dust, defects, and other contaminants, $I(x, y)$ is a function of position. In order to then calculate the transmission, a second image is taken with the same illumination, $I(x, y)$. A third image is taken without any illumination to record the dark counts on the camera. The transmission is then calculated as follows:

$$T_{\mathrm{atoms}} = \frac{I_{\mathrm{transmission}}(x, y) - I_{\mathrm{dark}}(x, y)}{I_{\mathrm{background}}(x, y) - I_{\mathrm{dark}}(x, y)}. \tag{2.11}$$

From the absorption profile, the optical depth $\mathcal{D}(x, y) = -\ln T_{\mathrm{atoms}}$ is computed. From the optical depth and knowledge of the trapping geometry, the BEC's bulk profile can be inferred.

2.6.2 Photon detection and digitization

In analyzing measurements, it is essential to consider the photon detection and digitization processes.

In the previous subsection, we derived an intensity distribution $I_{\text{transmission}}(x, y)$ that contains a shadow of the BEC and atoms. At this point, we must introduce the system magnification, M, sensor pixel width dx (which is equal to the pixel pitch x_p when there is a 100% fill factor, which I assume per the Princeton Instruments PIXIS specifications [62]), detector quantum efficiency η and exposure time dt. Furthermore, I also introduce the imaging system transmission, T_{imaging}, which represents the net transmission of all optical elements after the BEC. Transmission of optical elements before the BEC is not as important because the imaging intensity can be increased to overcome these losses without affecting SNR. Given these parameters, the average number of photons incident upon the detector with an atom transmission profile T_{atoms} is computed as:

$$N_{\text{photons}} = \frac{T_{\text{imaging}} T_{\text{atoms}} I(x, y)(dx)^2 dt}{\hbar\omega_0 M^2}. \tag{2.12}$$

I compute the number of electrons $N_{\text{electrons}}$ by considering the sensor's quantum efficiency:

$$N_{\text{electrons}} = \frac{\eta T_{\text{imaging}} T_{\text{atoms}}(x, y) I(x, y)(dx)^2 dt}{\hbar\omega_0 M^2}. \tag{2.13}$$

It is during the conversion from photons to electrons that one of the main sources of noise, photon shot noise, is introduced. Photon shot noise scales with the square root of electron count as

$$\mathcal{N}_{\text{SN}} = \sqrt{\frac{\eta T_{\text{imaging}} T_{\text{atoms}}(x, y) I(x, y)(dx)^2 dt}{\hbar\omega_0 M^2}}. \tag{2.14}$$

With an understanding of photon shot noise, it is now clear that the choice of detuning is essential. The SNR is given by

$$\text{SNR} = \frac{N_{\text{electrons}}}{\mathcal{N}_{\text{SN}}} = \sqrt{N_{\text{electrons}}} = \sqrt{\frac{\eta T_{\text{imaging}} e^{-\mathcal{D}(x,y)}(x, y) I(r, \theta)(dx)^2 dt}{\hbar\omega_0 M^2}}, \tag{2.15}$$

where the optical depth, $\mathcal{D}(x, y) = -\ln[T_{\text{atoms}}]$, is given by

$$\mathcal{D}(x, y) = \sigma_0 \frac{1}{1 + 4\Delta^2/\Gamma^2} \tilde{D}(r, \theta) \tag{2.16}$$

in the limit of $I \ll I_{\text{sat}}$. Large optical depths will reduce SNR; this can be reversed by increasing either intensity (though only slight in order to maintain $I \ll I_{\text{sat}}$), exposure time, or detuning. Increasing intensity or exposure time when close to resonance increases the destructiveness of the image, therefore it is preferable to increase the detuning.

Of interesting and important note in this expression is that the SNR is a function of atom column density. If the system is designed to optimize the SNR for the peak atom column density, it will not be optimized for low column density regions and vice versa. This comes into play when

measuring vortex location; vortex cores are regions with very low column density. Accordingly, higher SNR for vortex detection is achieved by using very low imaging intensities. In fact, the imaging intensities are so low that the system is in some cases no longer shot noise limited, which is when the EMCCD's multiplication gain can be used to further improve SNR by overcoming readout noise.

2.6.3 Modeling vortex SNR

In order to understand the imaging of BECs and to corroborate experimental observations, it is essential to have some idea of what one is looking for. In the University of Arizona BEC lab, an anisotropic harmonic trap is used with radial trapping frequency $f_R \approx 8$ Hz and axial trapping frequency $f_z \approx 90$ Hz. The overall single-particle potential of the trap is thus

$$V_0 = \frac{1}{2}m\omega_R^2 r^2 + \frac{1}{2}m\omega_z^2 z^2 \tag{2.17}$$

where $\omega_R = 2\pi f_R$ and $\omega_z = 2\pi f_Z$ are the radial and axial trapping angular frequencies. In the limit of no inter-atomic interaction, the atoms assume the single-particle gaussian ground state in all three dimensions. In the case of a strongly repulsive interaction, the Thomas-Fermi approximation provides an adequate starting point for a BEC geometry:

$$|\Psi_g^{(TF)}(r,z)|^2 = \max\left\{\frac{1}{gN}\left[\mu - \frac{1}{2}m\left(\omega_R^2 r^2 + \omega_z^2 z^2\right)\right], 0\right\} \tag{2.18}$$

where $g = 4\pi\hbar^2 a/m$ is the interaction term, a represents the s-wave scattering length, m the atomic mass, N is the atom number, and

$$\mu = \frac{15^{1/2}}{2}\left(\frac{Na}{\bar{r}}\right)^{2/5}\hbar\bar{\omega} \tag{2.19}$$

is the chemical potential. Note that $\bar{r}$ and $\bar{\omega}$ represent the geometric mean oscillator length and the geometric mean oscillator frequency respectively [12].

The radial structure of a vortex in a BEC's wavefunction is approximated by [12]

$$f(\rho,z) = \frac{\rho/\xi}{\sqrt{2+(\rho/\xi)^2}} \tag{2.20}$$

where the healing length, ξ, is given by $\xi(x,y,z) = \sqrt{\frac{1}{8\pi a D(x,y,z)}}$, $D(x,y,z)$ represents the local atom density and ρ represents the distance away from the center of a vortex core [12]. Because the healing length ξ is a function of the local density $D(x,y,z)$, both ξ and the core structure f are functions of x, y, and z.

For the sake of studying the optical transmissive and absorptive properties of a BEC with a vortex, I consider a BEC within the Thomas-Fermi approximation and a vortex oriented

in the axial direction (which minimizes energy) located in the center of the BEC so that $r = \sqrt{x^2 + y^2} = \rho$. I further assume that the vortex is small enough such that the bulk BEC density does not vary significantly over the area immediately surrounding the vortex. The atom density in the vicinity of the centrally located vortex is approximated by

$$D_V(x, y, z) = D_g(x, y, z) f(r, z)^2, \tag{2.21}$$

where $D_g(x, y, z)$ represents the ground state density profile with no vortex. The column density is found by integrating the probability density with respect to z,

$$\tilde{D}_V(x, y) = \int D_g(x, y, z) f(r, z)^2 \, dz. \tag{2.22}$$

From this expression, the optical depth, which is a function of the integrated atom column density as shown in equation 2.16, can be written as:

$$\mathcal{D}_V(x, y) = -\frac{\sigma_0}{2} \frac{1}{1 + 4\Delta^2/\Gamma^2} \tilde{D}_V(x, y). \tag{2.23}$$

I define the peak optical depth to be

$$\mathcal{D}^{\text{Peak}} = -\frac{\sigma_0}{2} \frac{1}{1 + 4\Delta^2/\Gamma^2} \tilde{D}^{\max}, \tag{2.24}$$

where $\tilde{D}^{(\max)}$ represents the peak column density in the absence of a vortex,

$$\tilde{D}^{\max} = \int D_g(x, y, z) dz = \frac{\mu}{gN} \frac{4z_0}{3}, \tag{2.25}$$

and where z_0 is the axial Thomas-Fermi radius.

The illumination without the atoms present is assumed to be perfectly uniform intensity I_0. The illumination transmitted by the atoms is then: $I(r, \theta) = I_0 e^{-\mathcal{D}(r,\theta)}$. This distribution is numerically sampled at 0.0446 microns, much less than the BEC healing length which is approximately 0.23 μm. The illumination distribution is convolved with an Airy pattern, $A(x, y)$, with first zero at $1.22\lambda/2NA = 1.83\mu$m, which corresponds to the diffraction-limited spot size of the microscope objective used in the apparatus, to produce the convolved intensity distribution

$$I_c(r, \theta) = I(r, \theta) * * A(r, \theta) \tag{2.26}$$

where $**$ denotes a two-dimensional convolution operation. This distribution is binned into a grid of pixels with with $\Delta x/M$ where $\Delta x = 16\mu$m is the pixel pitch in image space and M is the system magnification. This computation yields a two-dimensional matrix $I_c[j, k]$ containing the energies per pixel per unit time in regions where a vortex exists and in regions where there is no vortex. The variables j and k represent discrete indices. The energy per pixel $E[j, k]$ is

found by multiplying the energy per pixel per unit time $I_c[j,k]$ by the exposure time Δt. The energy per unit pixel is converted to photons per pixel $P[j,k]$ by dividing through by photon energy hc/λ. The electrons per pixel $N[j,k]$ is found by multiplying the photons per pixel by the quantum efficiency η. In the absence of stray light, it is the electrons per pixel $N[j,k]$ that serves as the signal. The shot noise is the square root of the electrons: $\mathcal{N}_{\mathrm{SN}}[j,k] = \sqrt{N[j,k]}$ or in the case of high electron multiplying gain, the shot noise is increased by a factor of $\sqrt{2}$: $\mathcal{N}_{\mathrm{SN}}^{(EM)}[j,k] = \sqrt{2N[j,k]}$. The total noise is assumed to be shot noise limited when EM gain is in use: $\mathcal{N}_{\mathrm{tot}} = \mathcal{N}_{\mathrm{SN}}^{(\mathrm{EM})}$. When EM gain is not in use, as is the case for the PIXIS, the total noise must include readout noise $\mathcal{N}_{\mathrm{RO}}[j,k] =$ constant and the total noise is then quantified as $\mathcal{N}_{\mathrm{tot}}[j,k] = \sqrt{\mathcal{N}_{\mathrm{SN}}[j,k]^2 + \mathcal{N}_{\mathrm{RO}}[j,k]^2}$.

With these calculations in mind, a spatially dependent SNR is calculated. I am mainly interested how the presence of a vortex affects the signal. I therefore perform the above calculations twice: once to calculate the signal counts with a vortex imprinted on the density profile N_V and once without N_{NV}. The vortex signal is computed to be the difference $S_V = N_V - N_{NV}$ and the noise on the signal is given by the noise associated with N_V, which may or may not include readout noise and may or may not have multiplication noise due to EM gain. I define the vortex signal-to-noise ratio to be

$$\mathrm{SNR}_V = \frac{S_V}{\mathcal{N}_{\mathrm{tot}}}. \tag{2.27}$$

With an analytical prediction for SNR, the SNR can be readily computed as a function of any variable. The calculated SNR is shown in figure 2.2 as a function of the peak optical depth of the BEC. This figure assumes that EM gain is on so that readout noise is negligible, the quantum efficiency is $\eta = 0.70$, the exposure time is 30 μs, the beam power is 25 μW, beam waist is 2 mm and the system magnification is 11.2. It appears that the optimal peak OD is about 2.2 for vortex detection given these imaging parameters.

Figure 2.3 shows the predicted SNR vs system magnification assuming EM gain is on so that readout noise is negligible, the quantum efficiency is $\eta = 0.70$, the exposure time is 30 μs, the beam power is 25 μW, beam waist is 2 mm and the peak OD is 2.2. It appears that the optimal system magnification is about 11 for vortex detection given these imaging parameters for absorption imaging. The initial increase in SNR with magnification for low magnification is because larger magnification will correspond to the blurred vortex core filling a larger fraction of the pixel, thus the pixel will contain less bulk BEC signal, which would otherwise spatially average out the vortex signal. For very high system magnification, the SNR decreases; this is because the shot noise becomes increasingly problematic as the number of photons decreases per pixel as magnification increases.

In both of the plots shown above the SNR for vortex detection tops out at about 3.3. This is good enough to detect a regularly spaced lattice of features, however, the confidence level in

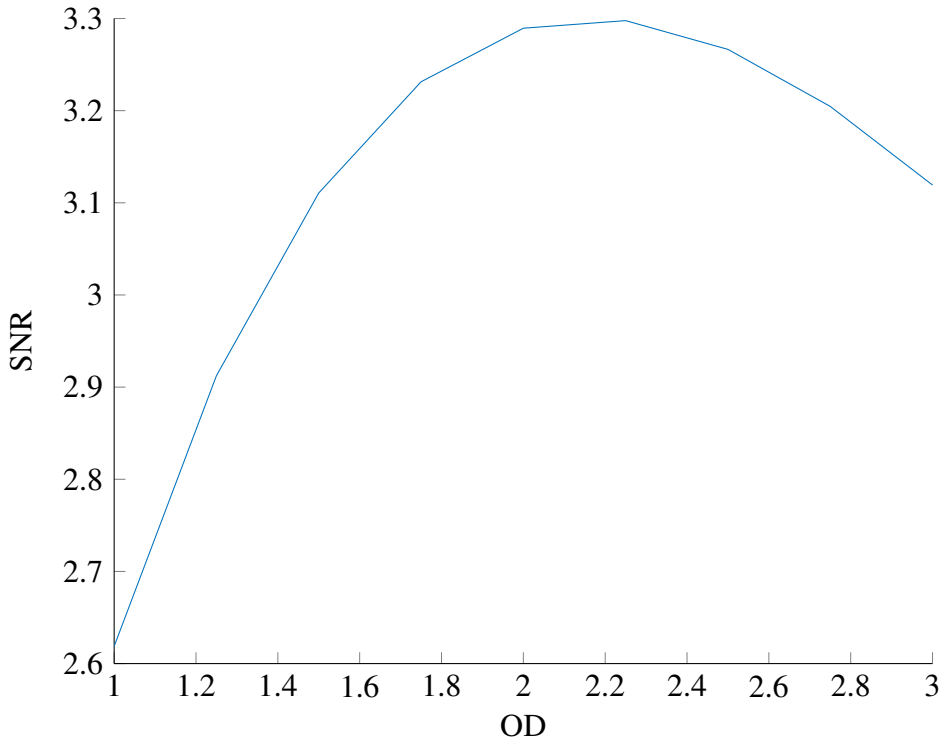

Figure 2.2: SNR Prediction as a function of peak optical depth with EM gain on, 0.70 QE, 30 μsec exposure, 25μW beam power, 2mm beam waist and magnification 11.2.

detecting a single vortex is much lower. A desirable SNR for single vortex detection would be on the order of 10.

2.7 Example images

The primary goal in this imaging study was to detect vortices *in situ*. For the purposes of understanding how vortex detection differs from bulk BEC measurements, it is helpful to first look at processed BEC images with high frequency spatial features such as soliton trains. In this case, an optical barrier was used to separate a BEC into two regions. The barrier was then lowered, allowing the two regions to crash into each other forming a soliton train. The resulting images are shown in figure 2.4. The observations were made with bright field absorption imaging with $\Delta t = 30\mu$s, optical pumping intensity $I/I_{\text{sat}} \sim 2$ near resonance with $|F = 1\rangle \rightarrow |F' = 2\rangle$ transition with probe light with intensity $I/I_{\text{sat}} \sim 2$ at detuning $\Delta = +2\Gamma$ from the $|F = 2\rangle \rightarrow |F' = 3\rangle$ transition.

These images illustrate typical *in situ* measurements of BEC parameters. In these data sets, a shadow image, background image, and dark frame are used to calculate the transmission and thus

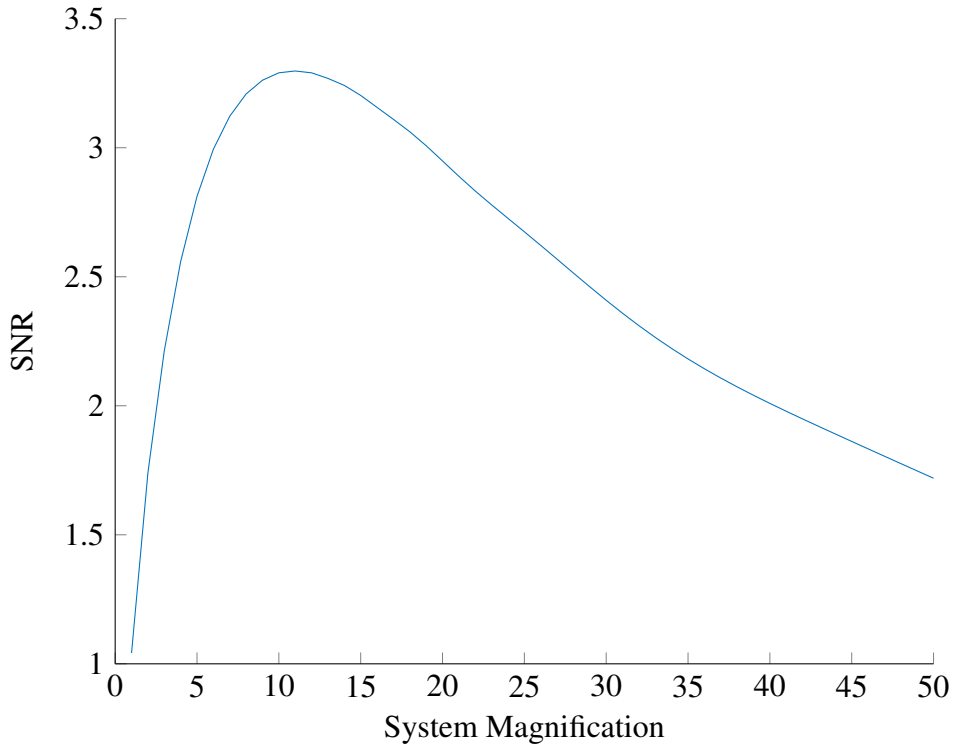

Figure 2.3: SNR Prediction as a function of peak optical depth with EM gain on, 0.70 QE, 30 μsec exposure, 25μW beam power, 2mm beam waist and peak optical depth of 2.2

optical depth. Shown in the figures is the calculated optical depth rather than the raw data. The key things to note are that the presence of atoms corresponds to a brighter signal when viewed in this manner. The high frequency features of note are shown in the center of the right image. The fringes are visible but their apparent contrast is low; in actuality, the density dips must go to zero because they correspond to a phase discontinuity in the waveform. Lastly, note the dark marks located sporadically around the BECs. These dark marks are not density features but instead imaging artifacts most likely resulting from non-uniform illumination due to contaminants or defects in the imaging path.

Representative images of BECs with vortex lattices are shown in figure 2.5. In these images the raw unprocessed data are shown. The images shown here are of approximately 10^6 atoms harmonically trapped in the $\left|F = 1, m_f = -1\right\rangle$ state with $f_{\text{Radial}} = 8$ Hz and $f_{\text{Axial}} = 16$ Hz. The atoms are illuminated with light near resonance with the $|F = 1\rangle \rightarrow |F' = 2\rangle$ transition with intensity $I/I_{\text{sat}} \sim 1$ and exposure time of 20 μs. The three images shown in this figure are the unprocessed absorption images only and are of the same BEC with the same vortex lattice — a demonstration of minimally destructive *in situ* imaging.

As mentioned earlier in the analysis of noise sources, the vortex cores were not easily identi-

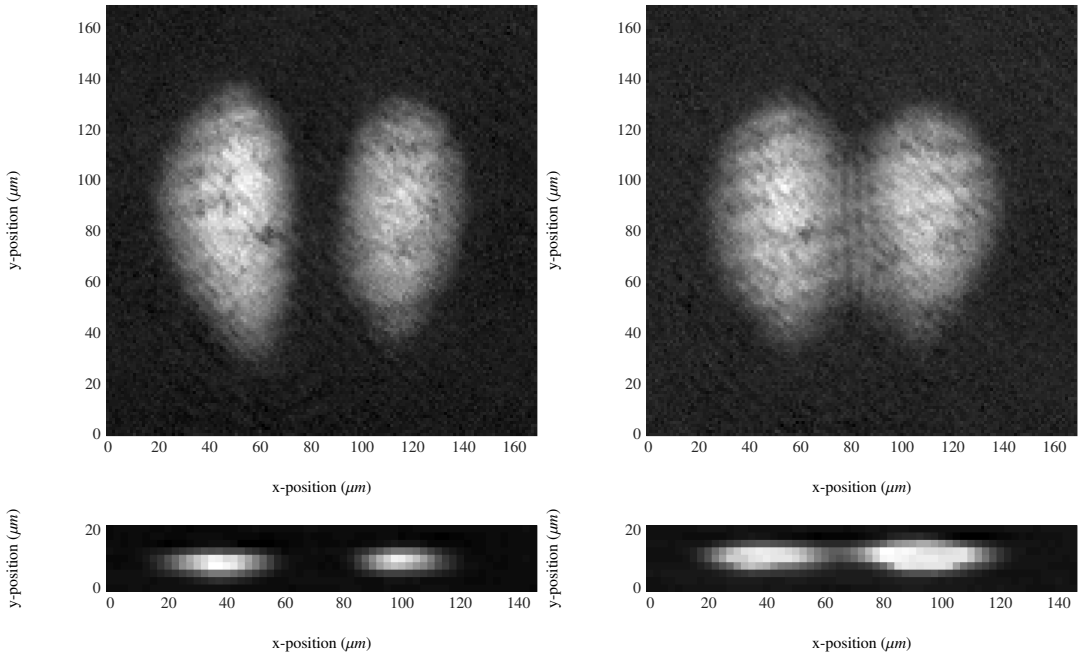

Figure 2.4: Observation of soliton train *in situ*. Top row is view from above. Bottom row is view from side using phase contrast imaging. Left column is with optical barrier raised and right column shows the collision of the two clouds and formation of the soliton train.

fiable after typical post-processing, but are clearly visible before processing. This is because the standard post-processing algorithm, which involves both a background frame and a dark frame, adds additional noise to the data, particularly when light levels are low. Note that the vortices are sized on the order of a pixel. The 16 micron pixel pitch corresponds to 1.43 μm in object space assuming a magnification of 11.2. Furthermore, the diffraction-limited spot size in object space is $d = 1.22\lambda f/\# \approx 1.83$ μm assuming a numerical aperture of 0.26.

2.7.1 Signal-to-noise measurements

Earlier in this chapter, calculations were done to predict the SNR for vortex detection. The SNR can also be measured directly by analyzing an image of a vortex lattice. The advantage of the vortex lattice is that because lattice is a regular pattern of vortices, the lattice site locations are known regardless of the SNR at that location.

Specifically, in a single BEC image with a vortex lattice, there are N_V vortices, each labelled with an index i. The average vortex signal, $\langle S_V \rangle$, is found by calculating the mean of the electron

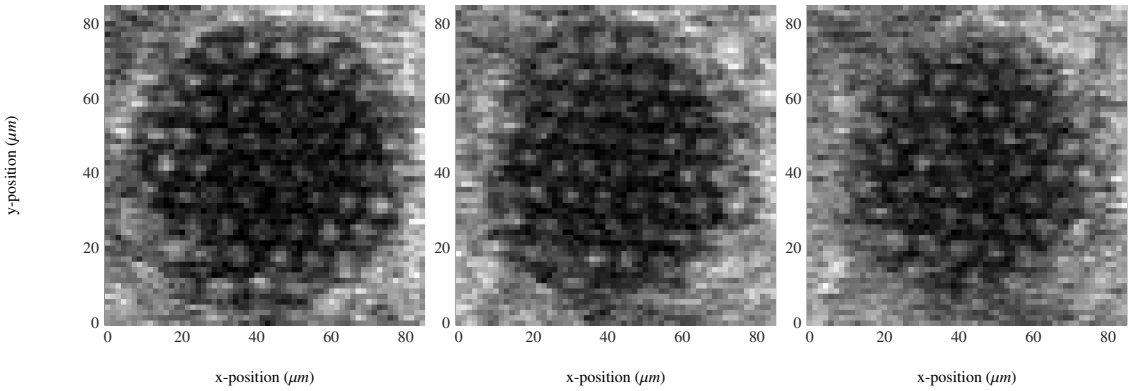

Figure 2.5: Representative *in situ* absorption images of a lattice of vortices in a BEC

counts at each vortex site,

$$\langle S_V \rangle = \frac{1}{N_V} \sum_{i=1}^{N_V} S_V^{(i)}, \tag{2.28}$$

where the electron counts at an individual vortex site is $S_V^{(i)}$. The signal due to a single vortex often spans multiple pixels; typically one of which is bright enough to subjectively say there is a vortex present, whereas the less bright pixels are typically much darker and would not suggest to the viewer the presence of vortex. For the purposes of this computation, the brightest pixel at a vortex site is used. In the event that one single pixel is not significantly brighter than the others, a pixel at the lattice site will be chosen at random. Without perfect knowledge of the BEC wave function, this method does overlook the possibility of a vortex lattice defect by assuming the presence of vortices at every lattice site; if there is indeed no vortex at a lattice site, we assume that there is a vortex present simply with low signal level because there is no way to know for certain.

The mean bulk BEC signal level, $\langle S_B \rangle$, is estimated in a similar way by finding the average pixel value at N_{NV} randomly chosen pixels corresponding to non-vortex sites in the bulk BEC. Because the bulk BEC is continuous, a sample size is chosen on the order of $N_{\mathrm{NV}} = 50$ of the bulk BEC to perform the same measurement. The average bulk signal, $\langle S_B \rangle$, is found by calculating the mean of the electron counts at a large sampling of N_{NV} non-vortex sites $S_B^{(i)}$:

$$\langle S_B \rangle = \frac{1}{N_{NV}} \sum_{i=1}^{N_{NV}} S_B^{(i)}. \tag{2.29}$$

With the mean number of counts at a lattice site and in the bulk BEC known, the signal due to a vortex can be computed explicitly:

$$\text{Vortex Signal} = \langle S_V \rangle - \langle S_B \rangle. \tag{2.30}$$

Furthermore, the noise is defined to be the standard deviation of the data set $\{S_V^{(i)}\}$:

$$\sigma_V = \sqrt{\frac{1}{N_{NV}} \sum_{i=1}^{N_{NV}} \left(S_V^{(i)} - \langle S_V \rangle\right)^2}. \tag{2.31}$$

Lastly, the experimental SNR is given by:

$$\text{SNR} = \frac{\langle S_V \rangle - \langle S_B \rangle}{\sqrt{\frac{1}{N_V} \sum_{i=1}^{N_V} \left(S_V^{(i)} - \langle S_V \rangle\right)^2}}. \tag{2.32}$$

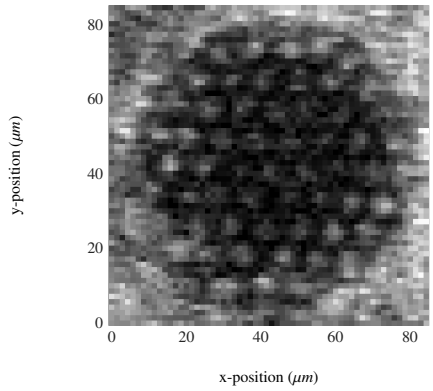

Figure 2.6: The first of a three image sequence, each containing a clear vortex lattice. This image was taken with on resonance illumination with $I/I_{\text{sat}} \sim 1$ on the $|F = 1\rangle \rightarrow |F' = 2\rangle$ transition with a 20 μs exposure time. The SNR is calculated by evaluating 35 vortex sites and 35 non-vortex sites to be SNR $\sim$ 2.28.

This SNR can be evaluated for a given image. Figure 2.6 shows a minimally destructive image taken of a vortex lattice. This is the first image of a three image sequence, each of which contained a clearly visible vortex lattice. This image was taken with on resonance illumination with $I/I_{\text{sat}} \sim 1$ on the $|F = 1\rangle \rightarrow |F' = 2\rangle$ transition with a 20 μs exposure time. Using the method just described, the SNR is calculated by evaluating 35 vortex sites and 35 non-vortex sites to be $SNR \sim 2.28$. In this example image it is very clear to the observer that a vortex lattice is present despite the low SNR. There regularity of this pattern absolutely makes it easier to identify. Some of the vortices in this image would not be easily identified as vortices if they were not in such a regular pattern.

2.8 Dark field imaging

2.8.1 Qualitative description

The previous section discussed the concept of absorption imaging, which is the conceptually most simple and familiar imaging technique used in the lab. As it turns out, absorption imaging

worked quite effectively and perhaps better than any other imaging technique, depending on what metrics are used to quantify image quality.

Another technique, known as a dark field imaging, was also employed in an attempt to image vortices *in situ*. This was not the first use of dark field imaging in BEC science; in fact, some of the first observations of BEC were done with dark field imaging [72]. Dark field imaging has also been used to make high sensitive measurements of BECs with very low atom numbers, in some instances as low as 7 atoms [73]. Dark field imaging is discussed at length in [21, 22].

A single lens optically performs a Fourier transform on the input field. Thus, if one were to place a sensor at the rear focal plane of an imaging objective, the image observed on the sensor would be the Fourier transform of the object plane. In dark field imaging, this fact is exploited by using this Fourier plane to filter out low spatial frequencies. In a two-dimensional Fourier transform, the lowest spatial frequencies are centrally located and higher spatial frequencies correspond to larger radial distances from the optical axis in this case.

In the BEC imaging techniques described in this paper, the BEC serves both as a transmission mask and a phase mask. In both cases, the BEC is actively illuminated. The illumination source itself serves as the lowest spatial frequency in the system. The BEC profile consists of higher spatial frequencies than the illumination source, because the illumination source is oversized such that the BEC is approximately uniformly illuminated.

Some of the earliest BEC measurements were made with dark field imaging using a small central obscuration — either a wire or a dot — designed to block the lowest spatial frequencies such as those corresponding to the illumination beam only, while permitting spatial frequencies corresponding to the bulk BEC to be passed by the filter [72]. In traditional absorption imaging, the BEC cloud corresponds to a dark cloud on a bright illuminated background. In the aforementioned use of dark field imaging, the illumination profile is filtered out and therefore the background is observed to be dark. The BEC itself will cause a bright cloud to appear on the sensor rather than a shadowed area. The primary benefit of this technique is that the BEC will now correspond to a larger photon count on the sensor, which directly results in a higher signal to noise ratio in the presence of atoms.

In the interest of observing vortices *in situ*, feature sizes of interest are not only much smaller than the illumination profile, but also much smaller than the BEC profile itself — thus we explored larger central obscurations. The theoretical outcome of a properly sized obscuration is that not only the illumination beam, but also the bulk BEC profile, will be filtered out. What will ideally remain is only the signal due to very small spatial features such as vortices. The different behaviors of the illumination beam, light refracted by the bulk BEC, and light refracted by small features such as vortices is illustrated in figure 2.7.

The BEC is treated as a phase object that coherently refracts light from an imaging probe beam. The atoms are stroboscopically illuminated with a probe beam with approximately uniform

intensity I propagating along the axial direction of the BEC. The phase shift $\phi(x, y)$ acquired as the probe passes through the BEC is a function of the integrated column density $\tilde{D}(x, y) = \int D(x, y, z)dz$ and is given by [74]

$$\phi(x, y) = -\tilde{D}(x, y)\sigma_0 \left(\frac{\Delta/\Gamma}{1 + 4(\Delta/\Gamma)^2 + I/I_{\text{sat}}} \right). \tag{2.33}$$

In this expression, σ_0 represents the atom-light scattering cross-section, $\Delta = \omega - \omega_0$ is the detuning of the probe beam of optical frequency ω from the atomic resonance ω_0, Γ is the natural linewidth of the atomic resonance, and I_{sat} is the saturation intensity.

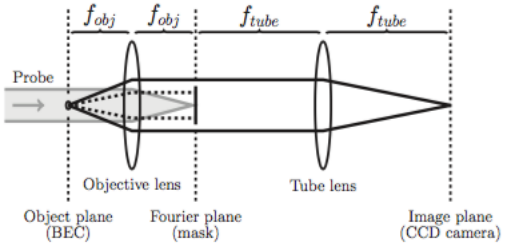

Figure 2.7: Layout of dark field imaging [74]. The light gray collimated input beam is shown coming to a focus at the dark field mask and is completely obscured. The light interacting with the bulk BEC profile is scattered into a relatively narrow angular region, which is depicted by the dotted line and is terminated at the dark field mask. The light interacting with small features such as vortices is scattered into a larger angular region, depicted with a solid line. This light is able to bypass the dark field mask because it is scattered into a much larger angular region.

With absorption imaging the maximum SNR should be obtained with on-resonant imaging light such that in the vicinity of a vortex, the only light seen on the sensor is light that is scattered by the vortex itself: a bright signal on a dark background will generate a high SNR for feature detection. Imaging close to resonance has a major disadvantage: this should in principle be highly destructive because each photon used will have a high probability of causing an atom to change spin states and be released from the trap. On the other hand, dark field imaging will yield a bright spot on a dark background regardless of the detuning used. Therefore, by choosing a detuning far from resonance that is minimally destructive but still allows vortices to be detected may be a more effective solution for non-destructive *in situ* imaging. The parameters for such a non-destructive dark field imaging technique were explored extensively.

2.8.2 Example images

Representative images of BECs with vortex lattices are shown in figure 2.8. The images shown here are of approximately 10^6 atoms harmonically trapped in the $\left|F = 1, m_f = -1\right\rangle$ state with

$f_{\text{Radial}} = 8$ Hz and $f_{\text{Axial}} = 16$ Hz. The atoms are illuminated with light detuned $\Delta \approx +3\Gamma$ with respect to the $|F = 1\rangle \rightarrow |F' = 2\rangle$ transition with intensity $I/I_{\text{sat}} \sim 0.07$ with an exposure time of 100 μs per frame. The three images shown in this figure are the unprocessed dark field images only and are of the same BEC with the same vortex lattice — another demonstration of minimally destructive imaging. These images were taken with the Photometrics Cascade 512B with EM gain enabled, thus reducing the sensor readout noise to effectively less than one electron. The frames are separated temporally by approximately 102 msec.

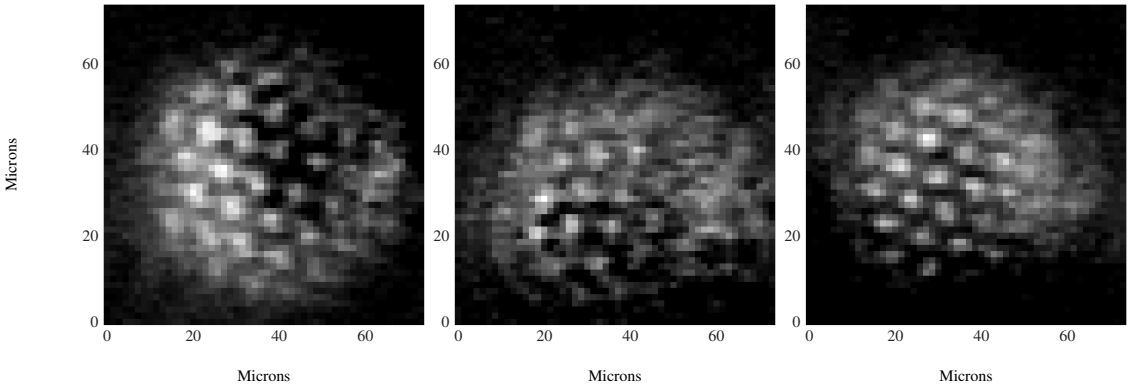

Figure 2.8: Representative *in situ* dark field images of a lattice of vortices in a BEC

2.9 Faraday imaging

A third imaging technique that is different altogether was successfully used for imaging vortices *in situ*. Faraday imaging shares the advantage of dark field imaging in that background illumination is essentially attenuated to zero.

2.9.1 Qualitative description

Faraday imaging works by illuminating the BEC with linearly polarized light.The BEC is in a nonzero magnetic field. The linearly polarized light can be written as the super position of σ_+ and σ_- light. In the presence of the magnetic field, the σ_+ and σ_- light experience different phase shifts, which manifests in this scenario as a rotation of the linear polarization angle of the illumination light that depends on the local column density of the BEC. A polarizing beam splitter is placed after the imaging objective, which dumps un-rotated light into an unused port and transmits the Faraday rotated light down the imaging path. Therefore, field points in the object plane that do not contain atoms and therefore do not rotate the linear polarization of the illumination light, are not imaged onto the camera. In the presence of atoms, however, the illumination light is Faraday rotated and is imaged onto the camera. For this reason, the presence of atoms appears

as a bright signal. Furthermore, background subtraction is not necessary in this form of imaging; however, a dark frame can be subtracted off to account for the DC bias on the sensor readout. The method of Faraday imaging was described in the first BEC experiments by Randy Hulet using Lithium and is described in greater length in their observations [5]. Gajdacz *et al* demonstrated their Faraday imaging system to produce upwards of one thousand spatially resolved images of a single BEC [75]. We have seen in our lab upwards of one hundred sequential spatially resolved images of a single BEC using Faraday imaging; however, not with the SNR needed to detect vortices.

2.9.2 Example images

Four example images taken using Faraday imaging are shown in figure 2.9. The left two images are *in situ* and the right two images are after $\sim$ 20 ms of ballistic expansion. These images are unique from the previous images in that first of all, the atoms are confined in a different trapping geometry: 8 Hz radial by $\sim$ 32 Hz axial where as earlier there atoms were confined in 8 Hz by 16 Hz and second of all the vortices are a disordered arrangement in all of these images.

For reasons that are not yet fully understood vortex visibility in highly oblate BECs has proven to be more difficult than in less oblate BECs. These images, which are of BECs with a 4:1 aspect ratio, show vortices in the most oblate BECs that we were able to detect vortices in. Increasing the aspect ratio to 6, 8, or 10 resulted in no obvious vortex detection. It is unclear why; the predicted vortex core size and bulk optical depth are not expected to be significantly difference in these scenarios.

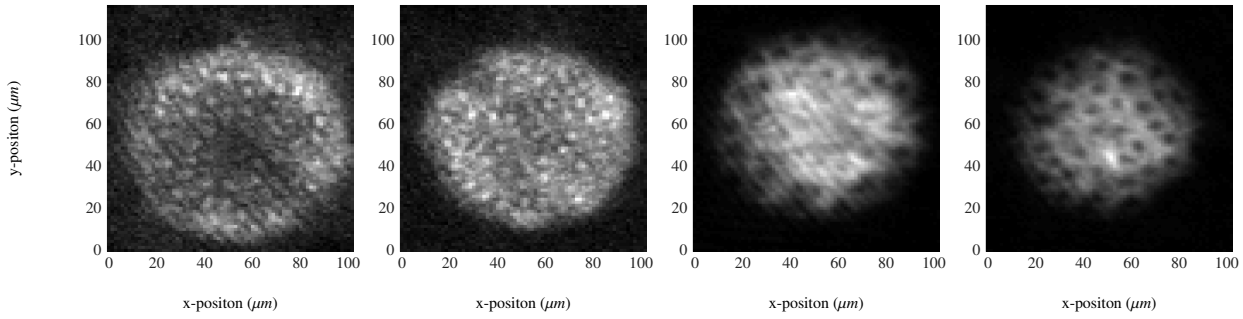

Figure 2.9: Example Faraday images taken of a BEC with a 4:1 aspect ratio. The left two images are taken *in situ* and the right two images are taken after expansion.

In Faraday images of vortices in a BEC, the optimum vortex signal was achieved by defocusing the BEC by approximately 20-30 μm from the optimal location for on resonance absorption imaging. This could be because the density profile of a vortex can act as a lens for off-resonant light.

2.9.3 Vortex as a microlens

The atom density in the vicinity of a vortex varies approximately as

$$D \propto \frac{(\rho/\xi)^2}{2 + (\rho/\xi)^2}, \tag{2.34}$$

which in the vicinity of small (ρ/ξ) can be approximated as the first element of the Taylor series expansion,

$$D \approx \frac{(\rho/\xi)^2}{2}. \tag{2.35}$$

The phase shift imprinted on the probe beam in the vicinity of the vortex core is then,

$$\phi(\rho) = \frac{\sigma_0}{2} \frac{}{1 + 4\Delta^2/\Gamma^2} \tilde{D}(r,\theta) \frac{(\rho/\xi)^2}{2}, \tag{2.36}$$

where I assume that variations in bulk column density ($\tilde{D}$) will be negligible compared to the variations due to the vortex core. The phase variation applied to a field by a vortex core is approximately quadratic, just like that of a positive thin lens: [76]

$$\phi_{\text{Thin Lens}}(r) = \frac{\pi}{\lambda f_{\text{lens}}} r^2, \tag{2.37}$$

where λ is the imaging wavelength and f_{lens} is the focal length of the thin lens. In other words, a vortex in a BEC can function as a thin lens for off-resonant probe beams with focal length

$$f_{\text{vortex}} = \frac{\pi}{\lambda} \frac{2}{\sigma_0} \frac{1 + 4\Delta^2/\Gamma^2}{2\Delta/\Gamma} \frac{1}{\tilde{D}} 2\xi^2. \tag{2.38}$$

This effective focal length can be on the order of tens of microns and could account for the vortex visibility being more prominent when defocused on the order of twenty to thirty microns.

Specifically, as the density of the BEC falls parabolically towards the edge of the BEC, the "focal length" of a vortex shifts. Furthermore, the local healing length ξ is inversely proportional to the local density $\xi \propto D^{-1}$ and therefore increases parabolically with the radius: $\xi \propto r^2$. And lastly, the effective entrance pupil area of the vortex lens scales with the healing length squared. This measure is significant because the brightness of a vortex detection event scales directly with the effective entrance pupil area of the vortex lens when appropriately defocused from the nominal on resonance focus position.

2.10 Conclusion

Three techniques for making *in situ* observations of quantized vortices in BEC were demonstrated in this chapter: absorption imaging, dark field imaging, and Faraday imaging. A side-by-side comparison of the three imaging techniques is shown in figure 2.10.

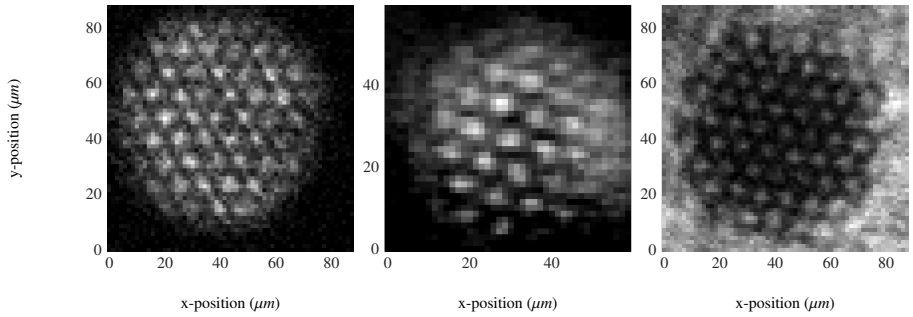

Figure 2.10: Comparison of absorption, dark field, and faraday images of vortices *in situ*, respectively.

Of the three imaging techniques, the Faraday imaging technique had the most repeatable high SNR results, with a typical SNR of 3.1 calculated according to the method described earlier; however, multiple images of a single vortex or vortex lattice were never observed for Faraday imaging. In order to observe vortices *in situ* using Faraday imaging, the atoms were first pumped to a secondary atomic state. It is likely that this link in the imaging chain served as the most destructive part of Faraday imaging, thus making non-destructive imaging with this technique more difficult. Faraday imaging using the $|F = 1\rangle \rightarrow |F' = 2\rangle$ transition was attempted; however, the SNR was consistently low and *in situ* observation of vortices using this technique was unsuccessful.

Dark field imaging permitted upwards of four consecutive images of a single vortex lattice *in situ* with degrading image quality for later images. However, the spatial uniformity of the vortex brightness was relatively low as seen in figure 2.8. In particular, often times vortices on one side of the BEC were brighter than the other side of the BEC. This could be attributed to the dark field mask being slightly off center or alternatively the illumination beam not being precisely orthogonal to the BEC and imaging objective. Additionally, the vortex visibility dropped off near the perimeter of the BEC. This is not necessarily unexpected. The dark field mask size is chosen specifically to match the anticipated vortex size. Both the vortex size and the integrated column density of the BEC will vary over the extent of the BEC: vortices towards the perimeter of the BEC will correspond to a larger healing length and also a lower integrated column density of bulk BEC. Both of these facts would cause light to refract into a smaller angular distribution than a vortex at the center of the BEC with a smaller healing length and larger integrated column density of the bulk BEC. Thus, a dark field mask optimized to observe vortices in the center of a BEC will be oversized for vortices on the perimeter of the BEC, thus causing perimeter vortices to appear dark or not appear at all. The SNR calculated for the example dark field image shown was found to be about 1.5.

Lastly, standard absorption imaging with low light levels near the atomic resonance proved

to consistently permit the observation of vortices in the BEC while being minimally destructive. Like dark field, this method permitted upwards of four consecutive *in situ* images of a vortex lattice in a BEC while also having uniform signal across the extent of the BEC as seen in figure 2.5. The SNR for the absorption imaging, as mentioned earlier, was calculated to be approximately 2.2.

To conclude this chapter, it has been demonstrated that *in situ* stroboscopic imaging of vortices is possible. The highest SNR was achieved with Faraday imaging techniques and least destructive imaging was achieved with bright-field-absorption imaging. We have not yet found parameters for tracking vortices in highly oblate traps in a non-destructive manner.

Going forward, there are several areas that can be improved upon for the next generation of quantum vortex microscope. First of all, the atoms could be trapped in a state such as $|F = 2, m_F = +2\rangle$ that has direct access to a cycling transition. As mentioned earlier, Faraday imaging proved to have the highest SNR; however, in order to access the high SNR faraday imaging it was necessary to first pump atoms to a state that has direct access to a cycling transition. This pumping procedure is thought to be the limiting factor for minimally-destructive imaging. By initially trapping atoms in a state with access to a cycling transition, the pumping procedure will be unnecessary and thus higher SNR non-destructive Faraday imaging may be possible. Secondly, a more optimal EMCCD camera that has a QE optimized for 780 nm would reduce the photon shot noise, permitting lower imaging powers and thus less-destructive illumination. Thirdly, weaker trapping frequencies could be used with the same aspect ratio to increase the healing length and vortex size, which would improve the imaging SNR. A more significant apparatus redesign could be done to permit closer optical access to the BEC cell permitting the use of potentially superior commercially available objectives and higher numerical aperture imaging. A different trap geometry could be used that has a static magnetic field vector optimized for the imaging technique, whether Faraday, dark field, or absorption, rather than using a time-varying off-axis magnetic field as is the case currently with the TOP trap. Lastly, vortex detection could be improved by minimizing the number of optical surfaces between the BEC and the camera sensor in addition to using narrow bandwidth V-coatings, which would be suitable because of the very narrow imaging bandwidth and can have upwards of 99.9% transmission rather than 98.5%, which is typical for a broadband NIR filter anti-reflection coating [77]. The current surfaces, their respective coatings, and approximate respective transmissions are listed in table 2.10 by assuming 4% reflectance of uncoated surfaces, measured reflectances, assuming 1.5% reflectance per surface of broadband IR coatings, assuming 99% reflectance of silvered mirrors, and the measured reflectance of the objective (88.5%) which is consistent with a 1.5% reflectance per surface of the assumed broadband coatings. The net system transmission including all surfaces is less than 0.6. If a particular imaging such as absorption imaging is pursued, no longer relevant optical elements such as polarizing optics could be removed from the system reducing the total

surface count. By using a V-coating on all remaining surfaces, the system transmission could be increased to greater than 0.95. This is relevant because as discussed earlier the shot noise limited vortex SNR scales with the square root of the optical transmission after the BEC $\sqrt{T_{\text{opt}}}$.

Element/ Subassembly	Assumed Coating	Surfaces	Surface Transmission (Reflection for mirror)	Subassembly Transmission
Pyrex Wall	Uncoated	2	0.96	0.92
Objective	Broadband NIR	8	0.985	0.89
Half wave plate	Broadband NIR	2	0.985	0.97
Chromatic filter	Uncoated	2	0.96	0.92
Polarizing beam splitter cube	Broadband NIR	3	0.985	0.955
Mirror	Broadband NIR	1	0.99	0.99
Tube Lens (Achromat)	Broadband NIR	3	0.985	0.96
Mirror	Broadband NIR	1	0.985	0.99
Flip in mirror	Broadband NIR	1	0.985	0.99
Camera cover glass	Broadband visible	2	0.985	0.922

Table 2.2: Optical surfaces between the BEC and the camera sensor and their respective coatings.

CHAPTER 3

A brief guide to numerical simulation of the damped Gross-Pitaevskii equation in the two-dimensional vortex regime

For the purpose of simulating the dynamics of the BECs in our lab, the two-dimensional (2D) damped Gross-Pitaevskii Equation (GPE) is propagated numerically using the split step method (also known as the Fourier or Spectral Method) [78]. The goal of this chapter is to review the methods used to model the University of Arizona's BEC system for the sake of future graduate students interested in modeling the vortex dynamics of our system. The specific methods described here are not new, but rather this chapter serves to consolidate resources and information found in other literature.

3.1 Time-dependent Gross-Pitaevskii equation: 3D, 2D, and dimensionless 2D formulations

The nonlinear Schrödinger equation, also known as the Gross-Pitaevskii Equation (GPE) is a wave equation, which arises from the Hartree-Fock approximation and can be used to model the dynamics of Bose-Einstein condensates: [12]

$$i\hbar\frac{\partial\psi(\mathbf{r},t)}{\partial t} = -\frac{\hbar^2}{2m}\nabla^2\psi(\mathbf{r},t) + V_1(\mathbf{r})\psi(\mathbf{r},t) + g(N-1)|\psi(\mathbf{r},t)|^2\psi(\mathbf{r},t). \tag{3.1}$$

In the context of this equation, $\psi(\mathbf{r},t)$ represents the complex-valued scalar wave function of the BEC and is normalized to unity, $\hbar$ represents the reduced Planck constant, m the mass of a single atom, $g = \frac{4\pi\hbar^2 a}{m}$ the nonlinear interaction strength where a is the inter-atomic s-wave scattering length, and N is the atom number. $V_1(\mathbf{r})$ is the single-particle potential. Since $N \gg 1$ in our apparatus, I approximate $N-1 \approx N$ in the remainder of this chapter.

In this section, we consider a cylindrically symmetric harmonic single-particle potential: $V_1(\mathbf{r}) = \frac{1}{2}m\omega_r^2 r^2 + \frac{1}{2}m\omega_z^2 z^2$. Under sufficiently tight axial confinement, the wave function $\psi(\mathbf{r},t)$ can be treated as separable and the z-dependent component is assumed to be in the single-particle ground state. The wave function can then be written as

$$\psi(\mathbf{r},t) = \psi_\perp(x,y,t)\psi_z(z,t), \tag{3.2}$$

where the axial wave function $\psi_z(z,t)$ can be expressed as a stationary state in the form

$$\psi_z(z,t) = \psi_g^{(z)}(z)e^{-iE_g^{(z)}t/\hbar} \tag{3.3}$$

The Laplacian operator, $\nabla^2 = \frac{\partial^2}{\partial x^2} + \frac{\partial^2}{\partial y^2} + \frac{\partial^2}{\partial z^2}$ can be written as the sum of a transverse Laplacian $\nabla_\perp^2 = \frac{\partial^2}{\partial x^2} + \frac{\partial^2}{\partial y^2}$ and an axial Laplacian $\nabla_z^2 = \frac{\partial^2}{\partial z^2}$. The single-particle potential can be written as $V_1(x, y, z) = V_1^\perp(x, y) + V_1^{(z)}(z)$, giving

$$i\hbar\psi_z\frac{\partial}{\partial t}\psi_\perp + E_g^{(z)}\psi_\perp\psi_z = -\frac{\hbar^2}{2m}\psi_z\nabla_\perp^2\psi_\perp - \frac{\hbar^2}{2m}\psi_\perp\nabla_z^2\psi_z + V_1^\perp\psi_\perp\psi_z + V_1^{(z)}\psi_\perp\psi_z + gN|\psi_\perp\psi_z|^2\psi_\perp\psi_z. \tag{3.4}$$

For a harmonic potential in z, $E_g^{(z)}\psi_g^{(z)} = -\frac{\hbar^2}{2m}\nabla_z^2\psi_g^{(z)} + V_1^{(z)}\psi_g^{(z)}$ and this equality permits the elimination of several terms, yielding the form

$$i\hbar\psi_z\frac{\partial}{\partial t}\psi_\perp = -\frac{\hbar^2}{2m}\psi_z\nabla_\perp^2\psi_\perp + V_1^\perp\psi_\perp\psi_z + gN|\psi_\perp\psi_z|^2\psi_\perp\psi_z. \tag{3.5}$$

Multiplication by ψ_z^* and integration with respect to z, noting that ψ_z is normalized to unity, yields the following form:

$$i\hbar\frac{\partial}{\partial t}\psi_\perp = -\frac{\hbar^2}{2m}\nabla_\perp^2\psi_\perp + V_1^\perp\psi_\perp + gN|\psi_\perp|^2\psi_\perp\int_{-\infty}^{\infty}|\psi_g^{(z)}|^4dz. \tag{3.6}$$

Using $\psi_g^{(z)} = \left(\frac{m\omega_z}{\pi\hbar}\right)^{1/4} e^{-m\omega_z z^2/2\hbar}$, I define a length parameter,

$$\ell = \left[\int_{-\infty}^{\infty}|\psi_g^{(z)}|^4dz\right]^{-1} = \sqrt{\frac{2\pi\hbar}{m\omega_z}}, \tag{3.7}$$

which is used to express the 2D GPE as follows:

$$i\hbar\frac{\partial}{\partial t}\psi_\perp = -\frac{\hbar^2}{2m}\nabla_\perp^2\psi_\perp + V_1^\perp\psi_\perp + \frac{gN}{\ell}|\psi_\perp|^2\psi_\perp. \tag{3.8}$$

The two-dimensional single-particle potential $V_1^\perp = \frac{1}{2}m\omega_r^2r^2$ is harmonic and has circular symmetry. Beginning with the 2D GPE for a harmonic trap,

$$i\hbar\frac{\partial}{\partial t}\psi_\perp = -\frac{\hbar^2}{2m}\nabla_\perp^2\psi_\perp + \frac{1}{2}m\omega_r^2r^2\psi_\perp + \frac{gN}{\ell}|\psi_\perp|^2\psi_\perp \tag{3.9}$$

a dimensionless time scale, $\tau = \omega_r t$, is defined. The harmonic oscillator has a natural length, $r_0 = \sqrt{\frac{\hbar}{m\omega_r}}$, which is used to define dimensionless lengths $\tilde{x} = x/r_0$, $\tilde{y} = y/r_0$, and $\tilde{r} = r/r_0$. A dimensionless differential operator, $\tilde{\nabla}^2 = r_0^2\nabla^2$, is also defined. Lastly, the transverse wave function has units of inverse length. I introduce a dimensionless wave function: $\tilde{\psi}_\perp = r_0\psi_\perp$. Using the nonlinear parameter $g = 4\pi\hbar^2a/m$, I arrive at a dimensionless 2D GPE:

$$i\frac{\partial}{\partial\tau}\tilde{\psi}_\perp = -\frac{1}{2}\tilde{\nabla}_\perp^2\tilde{\psi}_\perp + \frac{1}{2}\tilde{r}^2\tilde{\psi}_\perp + \frac{4\pi aN}{\ell}|\tilde{\psi}_\perp|^2\tilde{\psi}_\perp. \tag{3.10}$$

This convenient formulation depends only on one dimensionless variable $\eta^{(2D)} = \frac{4\pi Na}{\ell}$ that regulates the strength of the nonlinearity,

$$i\frac{\partial}{\partial\tau}\tilde{\psi}_\perp = -\frac{1}{2}\tilde{\nabla}_\perp^2\tilde{\psi}_\perp + \frac{1}{2}\tilde{r}^2\tilde{\psi}_\perp + \eta^{(2D)}|\tilde{\psi}_\perp|^2\tilde{\psi}_\perp. \tag{3.11}$$

At this point, a two-dimensional Gross-Pitaevskii Equation has been identified and is known in a dimensional form as well as a dimensionless form. The two-dimensional GPE in dimensionless form will prove useful for simulations.

In simulations it is convenient to have an energy scale in the 2D GPE. One convenient natural energy is the dimensionless chemical potential $\tilde{\mu}$, which can be determined analytically for the ground state of the BEC in the harmonic trap. To do so, I consider the dimensionless ground state of the GPE,

$$\tilde{\psi}_\perp = \tilde{\psi}_{\perp,0}e^{-i\tilde{\mu}_\perp\tau}, \tag{3.12}$$

in the limit where interaction energy dominates kinetic energy and the kinetic energy term can be neglected. Substitution of this form into the 2D GPE results in

$$\tilde{\mu}_\perp = \frac{1}{2}\tilde{r}^2 + \eta^{(2D)}|\tilde{\psi}_{\perp,0}|^2, \tag{3.13}$$

valid for $\tilde{r} \leq \sqrt{2\tilde{\mu}}$, which is the Thomas-Fermi radius for the symmetric harmonic 2D GPE. Equivalently, the wavefunction probability density can be expressed in terms of the radial parameter and the chemical potential:

$$|\tilde{\psi}_{\perp,0}|^2 = \tilde{\mu}_\perp - \frac{1}{2}\tilde{r}^2, \tag{3.14}$$

again valid for $\tilde{r} \leq \sqrt{2\tilde{\mu}}$. By normalizing the wave function to one, $\int |\psi(\mathbf{r},t)|d\mathbf{r} = 1$, the chemical potential is found to be:

$$\tilde{\mu}_\perp = \sqrt{\eta^{(2D)}/\pi}. \tag{3.15}$$

This convenient expression for chemical potential will be used as a dimensionless energy scale.

3.2 Dynamical regimes

In the previous section a 2D GPE was derived from the 3D GPE for an axially symmetric harmonic potential. The dimensional reduction is highly advantageous from a computational standpoint. To illustrate the need for dimensional reduction, consider the case of a computational grid that allows resolution on the order of the healing length over the extent of the entire atom cloud.

The axial Thomas-Fermi radius in our experiments is approximately 5 μm, the radial Thomas-Fermi radius is approximately 51 μm. The healing length ξ, which is the length over which the waveform restores itself from a zero-value boundary condition and serves as a metric for the radius of a vortex core, can be found by equating the kinetic energy per particle ($\hbar^2/2m\xi^2$) with the nonlinear interaction energy $4\pi\hbar^2 Da/m$ where D represents the local density: [12]

$$\frac{\hbar^2}{2m\xi^2} = \frac{4\pi\hbar^2 Da}{m}, \tag{3.16}$$

and solving for the healing length yields

$$\xi = \sqrt{\frac{1}{8\pi Da}}, \tag{3.17}$$

which is approximately 280 nm in the center of the BEC with a radial trapping frequency $\omega_r = 2\pi \times 8$ Hz, axial trapping frequency $\omega_z = 2\pi \times 90$ Hz and atom number $N = 1.7 \times 10^6$ atoms. To ensure appropriate resolution over the extent of the BEC, I choose a grid size with sampling distance less than the healing length. For a fully three-dimensional grid, this becomes computationally expensive because the computation time of fast Fourier transforms (FFTs) scales with number of elements and it is therefore advantageous to reduce the dimensionality of the simulation whenever possible. The reduction of the computational domain to two dimensions in the case of our system can increase the processing speed by more than an order of magnitude.

For fully three-dimensional systems with aspect ratios on the order of unity and many atoms, the Thomas-Fermi approximation serves as a good approximation for the ground-state profile of a BEC [12]. For sufficiently anisotropic systems with cylindrical symmetry, there exist regimes wherein the wave function's dynamics are restricted to one or two dimensions. The reason for this is that in highly anisotropic systems, the trapping frequency can be made sufficiently strong such that excitations in the tight dimensions are energetically forbidden or energetically highly improbable. Being forced into the ground state in the tight dimensions, the matter wave assumes the single-particle gaussian ground state for harmonic trapping in those dimensions — and the Thomas-Fermi approximation is no longer valid in these dimensions. This is the assumption that was made in the previous section in order to derive the 2D GPE [79]. The applicability of the 2D GPE rests on the assumption that the trap is sufficiently anisotropic such that the matter wave will not have any excitations in the tightly trapped dimension. For highly anisotropic systems with cylindrical symmetry, there exists a crossover atom number, $N_{\text{crossover}}$. If $N < N_{\text{crossover}}$, the dynamics can be assumed frozen in the tight axial dimension. For oblate BECs, [79]

$$N_{\text{crossover}} = \frac{a}{\bar{r}}\Gamma^{-5/3}\sqrt{\frac{32}{225}}, \tag{3.18}$$

where $\Gamma = \omega_r/\omega_z$ is the trapping aspect ratio for cylindrically symmetric harmonic trapping, and is less than one for an oblate disk geometry. The quasi-two-dimensional crossover atom

number for our experimental system is approximately 10^4, or two orders of magnitude less than the experimental atom number of about 1.7×10^6 and so our system is well within the 3D regime. This crossover is determined by equating the chemical potential (computed using the Thomas-Fermi approximation) with the energy necessary to excite an atom in the tight dimension to the first excited state, $\hbar\omega_z$. The significance of this is that the energy necessary for an excitation in this dimension is set to be approximately the energy necessary for an atom to enter or exit the BEC. The experimental parameters studied in this dissertation are not within this limit, but the 2D GPE can still be suitable for modeling dynamics of BECs in our highly oblate traps.

3.3 Defining a nonlinear parameter

In our highly oblate traps, the BEC is not in the quasi-two-dimensional regime. However, the *vortex dynamics* are in a two-dimensional regime and therefore the 2D GPE can serve as a useful model for vortex dynamics [80]. In this two-dimensional vortex regime Kelvin waves, which correspond to the bending modes of a vortex core, are suppressed, therefore keeping vortices aligned along the axial dimension of the BEC. To implement 2D GPE simulations an appropriate effective nonlinear coefficient must first be established.

Rather than using $\ell = \sqrt{2\pi\hbar/m\omega_z}$, where ω_z is the actual axial trap frequency, we take an alternative approach. We define an effective number of atoms N_{eff}, an effective radial trap frequency ω_{eff}, and an effective length parameter ℓ_{eff} that collectively match the central density, chemical potential, and radial Thomas-Fermi radius of our experimental system of interest to the same measures of our numerics. By matching the Thomas-Fermi radius, central density, and chemical potential of the experiment, the speed of sound of the numerical system is also matched to the experimental system and direct comparison of time, velocity, and length scales between experimental and numerical results is facilitated [81].

3.3.1 The effective 2D chemical potential

In this subsection I compute the two-dimensional chemical potential, μ_{eff}. I begin with the two-dimensional GPE:

$$i\hbar\frac{\partial\psi_\perp}{\partial t} = -\frac{\hbar^2}{2m}\nabla^2\psi_\perp + V\psi_\perp + \frac{N_{\text{eff}}g}{\ell_{\text{eff}}}|\psi_\perp|^2\psi_\perp, \tag{3.19}$$

where $V = \frac{1}{2}m\omega_{\text{eff}}^2 r^2$ is the single particle potential. I neglect the kinetic energy term per the Thomas-Fermi approximation and assume a stationary state $\psi_\perp = \psi_{\perp 0}e^{-i\mu_{\text{eff},\perp}t/\hbar}$, leading to

$$\mu_{\text{eff},\perp} = V + \frac{N_{\text{eff}}g}{\ell_{\text{eff}}}|\psi_{\perp 0}|^2. \tag{3.20}$$

Solving for the probability density gives

$$|\psi_{\perp 0}|^2 = \frac{\ell_{\text{eff}}}{N_{\text{eff}} g}\left(\mu_{\text{eff},\perp} - \frac{1}{2}m\omega_{\text{eff}}^2 r^2\right)\Theta(r - r_{\text{TF}}), \tag{3.21}$$

where $\Theta(x)$ is the Heaviside step function and $r_{\text{TF}} = \sqrt{\frac{2\mu_{\text{eff},\perp}}{m\omega_{\text{eff}}^2}}$ is the radial Thomas-Fermi radius. To solve for the chemical potential, I use the normalization of $\psi_{\perp 0}$:

$$1 = \int_0^\infty r\, dr \int_0^{2\pi} d\theta\, |\psi_{\perp 0}|^2 = \int_0^\infty r\, dr \int_0^{2\pi} d\theta\, \frac{\ell_{\text{eff}}}{N_{\text{eff}} g}\left(\mu_{\text{eff},\perp} - \frac{1}{2}m\omega_{\text{eff}}^2 r^2\right)\Theta(r - r_{\text{TF}}), \tag{3.22}$$

giving

$$\mu_{\text{eff},\perp} = 2\hbar\omega_{\text{eff}}\sqrt{\frac{N_{\text{eff}} a}{\ell_{\text{eff}}}}. \tag{3.23}$$

The corresponding effective 3D chemical potential is found by adding the single-particle axial ground state energy:

$$\mu_{\text{eff}} = \mu_{\text{eff},\perp} + \frac{1}{2}\hbar\omega_{z,\text{eff}}. \tag{3.24}$$

Using the approach from earlier, the effective length parameter is now found to be to be $\ell_{\text{eff}} = \sqrt{2\pi\hbar/m\omega_{z,\text{eff}}}$, where $\omega_{z,\text{eff}}$ is an effective trapping frequency in the axial dimension, and so the full effective chemical potential is found to be [82]

$$\mu_{\text{eff}} = 2\hbar\omega_{\text{eff}}\sqrt{N_{\text{eff}} a/\ell_{\text{eff}}} + \frac{\pi\hbar^2}{m\ell_{\text{eff}}^2}. \tag{3.25}$$

3.3.2 The effective 2D radial Thomas-Fermi radius

The Thomas-Fermi radius of the effective two-dimensional system corresponds to where the wave function goes to zero:

$$r_{\text{TF,eff}} = 2\sqrt{\frac{\hbar}{m\omega_{\text{eff}}}}\left(\frac{N_{\text{eff}} a}{\ell_{\text{eff}}}\right)^{1/4}. \tag{3.26}$$

3.3.3 The effective 2D central density

The two-dimensional GPE requires that atoms be in the z-dimensional harmonic oscillator ground state; however, in the radial dimensions, the atoms assume a Thomas-Fermi profile:

$$\psi(r,\theta,z) = \mathcal{N} e^{-\pi z^2/\ell_{\text{eff}}^2}\text{Max}\left(\sqrt{1 - r^2/r_{\text{TF}}^2}, 0\right) \tag{3.27}$$

where

$$\mathcal{N} = 2^{3/4}\pi^{-1/4}\ell_{\text{eff}}^{-1/2}r_{\text{TF}}^{-1} \tag{3.28}$$

is a normalization constant. The peak atom density is found by multiplying the normalized central probability density $|\psi(r = 0, z = 0)|^2$ by the effective number of atoms:

$$N_{\text{eff}}|\psi(r = 0, z = 0)|^2 = N_{\text{eff}}m\omega_{\text{eff}}\frac{1}{\pi\hbar}\sqrt{\frac{N_{\text{eff}}}{2a\ell_{\text{eff}}}}. \tag{3.29}$$

3.3.4 The 3D chemical potential

To compute the 3D chemical potential of the experimental BECs, I use [12]

$$\mu = \frac{15^{2/5}}{2}\left(\frac{Na}{\bar{r}}\right)^{2/5}\hbar\bar{\omega}. \tag{3.30}$$

This expression is a good approximation for BECs in anisotropic harmonic traps where the Thomas-Fermi approximation is valid. In this form, $\bar{r}$ is the geometric mean of the natural oscillator lengths and $\bar{\omega}$ is the geometric mean of the oscillator frequencies.

3.3.5 The 3D radial Thomas-Fermi radius

With an analytical expression for the full 3D chemical potential, the radial Thomas-Fermi radius can be expressed explicitly in terms of trap geometry and atom number as

$$r_{\text{TF:}r} = \sqrt{\frac{\hbar\bar{\omega}}{m\omega_r^2}}15^{1/5}\left(\frac{Na}{\bar{r}}\right)^{1/5}. \tag{3.31}$$

3.3.6 The 3D peak density

For the experimental parameters that are in the 3D regime, the probability density,

$$|\psi|^2 = \frac{1}{Ng}\text{Max}\left\{(\mu - V), 0\right\} = \frac{1}{Ng}\text{Max}\left\{\left(\mu - \sum_i \frac{1}{2}m\omega_i^2 x_i^2\right), 0\right\}, \tag{3.32}$$

is normalized to one. By multiplying the total number of atoms N by the normalized probability density, the peak density is evaluated to be

$$N|\psi|^2_{\text{max}} = N\frac{m}{4\pi\hbar^2 a}\frac{15^{2/5}}{2}\left(\frac{Na}{\bar{r}}\right)^{2/5}\hbar\bar{\omega}. \tag{3.33}$$

3.4 Solving for the effective two-dimensional parameters

In the previous section analytical expressions were found for the chemical potential, peak density, and Thomas-Fermi radius of both the three-dimensional case as well as the effective two-dimensional case. The experimental system corresponds to a three-dimensional matter wave, though in the two-dimensional vortex dynamics regime. An effective atom number,

$$N_{\text{eff}} = \frac{15^{3/5}}{16}\frac{\sqrt{\pi}}{a}\sqrt{2+\sqrt{2}}\sqrt{\frac{\hbar\bar{\omega}^3}{m\omega_r^4}}\left(\frac{Na}{\bar{r}}\right)^{3/5}, \tag{3.34}$$

effective radial trapping frequency,

$$\omega_{\text{eff}} = 2^{-1/4}\omega_r, \tag{3.35}$$

and effective length parameter

$$\ell_{\text{eff}} = \sqrt{\frac{\pi\hbar}{m\bar{\omega}}}\sqrt{2}\sqrt{2+\sqrt{2}}15^{-1/5}\left(\frac{Na}{\bar{r}}\right)^{-1/5} \tag{3.36}$$

$$\tag{3.37}$$

are found by equating the three-dimensional Thomas-Fermi radius, chemical potential, and peak density with the effective two-dimensional Thomas-Fermi radius, chemical potential, and peak density respectively in a system of equations. In the above expressions, N denotes the experimental atom number, $\bar{\omega}$ denotes the geometric average experimental trapping frequency, $\bar{r}$ denotes the geometric average natural harmonic oscillator length of the experimental system, ω_{eff} denotes the effective two-dimensional radial trapping frequency, ℓ_{eff} corresponds to the effective length parameter described earlier, and N_{eff} describes the effective two-dimensional atom number.

The dimensionless effective two-dimensional nonlinear parameter found earlier can now be written explicitly in terms of the effective atom number and the effective length parameter as

$$\eta^{(2D)} = \frac{4\pi a N_{\text{eff}}}{\ell_{\text{eff}}}. \tag{3.38}$$

The role of ω_{eff} is to scale the dimensionless time: $\tau = \omega_{\text{eff}}t$. A dimensionless phenomenological damping parameter, γ, can also be used in simulation. The inclusion of the damping parameter serves a dual purpose: firstly to account for phenomenological dissipation and secondly, by damping out higher energy modes, higher dissipation factors permit the simulation to run at a lower temporal resolution and so requiring fewer calculations per simulation. In this work a dissipation factor of $\gamma \approx 0.003$ is used and is on the upper end of experimentally realistic phenomenological damping parameters [83, 84]. The final form of the GPE used in the numerical study described in the following chapter is:

$$i\frac{\partial}{\partial\tau}\tilde{\psi}_\perp = (1-i\gamma)\left[-\frac{1}{2}\tilde{\nabla}_\perp^2\tilde{\psi}_\perp + \frac{1}{2}\tilde{r}^2\tilde{\psi}_\perp + \eta^{(2D)}|\tilde{\psi}_\perp|^2\tilde{\psi}_\perp\right]. \tag{3.39}$$

CHAPTER 4

A method for nucleating vortex dipoles in BECs

In the previous chapter, the numerical methods for simulating the GPE in the two-dimensional vortex regime were reviewed. In this chapter, a mechanism for imprinting a vortex dipole onto a BEC is investigated numerically and theoretically. Additionally an experimental layout is proposed and prototyped.

The method developed in this chapter seeks to push the state-of-the-art wave function engineering to include the ability to imprint a vortex dipole on demand arbitrarily within a BEC. While other methods currently exist to nucleate a vortex dipole, they either require a barrier moving above a critical velocity that disturbs a significant portion of the BEC or in the case of a modulating repulsive barrier, the physics behind vortex dipole nucleation are not understood and therefore the method is not yet very precise. An experimentally-realizable method using stationary barriers to imprint vortex dipoles in a BEC on demand is investigated numerically in this chapter and a corresponding experimental method is outlined and prototyped.

4.1 Vortex dipole basics

A vortex dipole is an isolated vortex-antivortex pair: one vortex with positive circulation and another with negative circulation about a common axis. This is particularly interesting in two-dimensional superfluid dynamics where all vortex circulation vectors must be oriented in one of two directions (up or down). The energy of a vortex dipole in a two-dimensional BEC can be expressed analytically: [12]

$$E_{\mathrm{VD}} \approx \frac{2\pi\hbar^2 n_{2\mathrm{D}}}{m} \ln\left(\frac{d}{\xi}\right) \tag{4.1}$$

where $n_{2\mathrm{D}}$ is the number of atoms per unit area of the ground-state BEC in the vicinity of the vortex dipole, m is the atomic mass, d is the vortex-anti-vortex separation, and ξ is the BEC healing length. The energy scales logarithmically with vortex-anti-vortex separation. This corroborates the observation in numerical simulations described later in this chapter that weaker perturbations lead to smaller dipoles and for slightly underpowered perturbations, a Jones-Roberts soliton [85].

4.2 Overview of method

The mechanism used to nucleate vortex dipoles in this chapter requires two optical dipole barriers to manipulate the local single particle potential seen by the atoms. The atomic resonance of ^{87}Rb is approximately 780nm. The presence of an optical beam detuned far from resonance functions as either an attractive potential or a repulsive potential. Specifically, a red-detuned beam with wavelength longer than that of the atomic resonance serves as an attractive potential, whereas a blue-detuned beam with wavelength shorter than that of the atomic resonance serves as a repulsive potential. Specific wavelengths are typically chosen based on what is commercially available.

Previously, a blue-detuned repulsive beam has been focused to a tight spot and pushed across a BEC above a critical velocity to nucleate a vortex dipole [14, 17]. In this chapter, I describe a method to introduce a vortex dipole into a BEC using a stationary but time-varying obstacle. In order to compensate for the beam being stationary, I use a combination of a red-detuned and a blue-detuned beam.

The ^{87}Rb BECs studied in the U of A BEC lab have an oblate cylindrically symmetric geometry with 11:1 aspect ratio, an axial Thomas-Fermi radius of approximately 4.5 μm and a radial Thomas-Fermi radius of approximately 50 μm. Two gaussian beams are vertically incident upon the BEC. The first beam is a 660-nm beam with a e^{-2} beam radius of approximately 10 μm. The second beam is a 850-nm beam, also with a e^{-2} beam radius of approximately 10 μm. Both beams are linearly polarized and sufficiently far-detuned from the atomic resonance (780 nm) such that the dominant atom-light interaction is the optical dipole interaction. For very large detunings, ignoring both the hyperfine and fine structure splitting, the optical dipole potential for a given beam is: [86]

$$U_{\text{dipole}} = \frac{3\pi c^2}{2\omega_0^3}\frac{\Gamma}{\Delta}I(\mathbf{r}). \tag{4.2}$$

In the above formulation, $I(\mathbf{r})$ represents the spatially dependent intensity, and $\Gamma = 2\pi(6.07 \times 10^6$ Hz) represents the natural linewidth for ^{87}Rb [87] .

The net potential induced by the two beams is:

$$U(\mathbf{r}) = \frac{3\pi c^2}{2\omega_0^3}\frac{\Gamma}{\Delta_{\text{Red}}}I_{\text{Red}}(\mathbf{r}) + \frac{3\pi c^2}{2\omega_0^3}\frac{\Gamma}{\Delta_{\text{Blue}}}I_{\text{Blue}}(\mathbf{r}). \tag{4.3}$$

The individual intensities are not equal; their respective intensities are given by

$$I_{\text{Red}}(\mathbf{r}) = I_{0,\text{Red}} \exp\left[-2(\mathbf{r} - \mathbf{r}_{0,\text{Red}})^2/\sigma^2\right] \tag{4.4}$$

and

$$I_{\text{Blue}}(\mathbf{r}) = I_{0,\text{Blue}} \exp\left[-2(\mathbf{r} - \mathbf{r}_{0,\text{Blue}})^2/\sigma^2\right]. \tag{4.5}$$

The peak amplitude of the beam intensities are chosen in this study so that the absolute dipole potential amplitudes are equal:

$$U_0 = \left|\frac{3\pi c^2}{2\omega_0^3}\frac{\Gamma}{\Delta_{\text{Blue}}}I_{0,\text{Blue}}\right| = \left|\frac{3\pi c^2}{2\omega_0^3}\frac{\Gamma}{\Delta_{\text{Red}}}I_{0,\text{Red}}\right|. \tag{4.6}$$

For our parameters, $\omega_{\text{Red}} \approx 2.2 \times 10^{15}$ s^{-1}, $\omega_{\text{Blue}} \approx 2.86 \times 10^{15}$ s^{-1}, $\omega_0 \approx 2.42 \times 10^{15}$ s^{-1}, $\Delta_{\text{Red}} \approx -1.99 \times 10^{14}$ s^{-1}, and $\Delta_{\text{Blue}} \approx 4.39 \times 10^{14}$ s^{-1}. The blue (660-nm) light source will be chosen to have an intensity higher than the red (850-nm) light source by a factor of ≈ 2.21:

$$I_{0,\text{Blue}} = \left|\frac{\Delta_{\text{Blue}}}{\Delta_{\text{Red}}}\right| I_{0,\text{Red}}. \tag{4.7}$$

Each of the two beams can be independently and arbitrarily placed. For the sake of the studies in this dissertation, however, the beams are placed an equal distance d from the BEC center and along a line that bisects the cross-section of the BEC: $\mathbf{r}_{0,\text{Blue}} = -d\hat{x}$ and $\mathbf{r}_{0,\text{Red}} = +d\hat{x}$. The net potential induced by the combined beams is:

$$U = U_0 \exp\left[-2((x-d^2)+y^2)/\sigma^2\right] - U_0 \exp\left[-2((x+d)^2+y^2)/\sigma^2\right]. \tag{4.8}$$

Lastly, the potential is time dependent. Specifically, it is ramped on and off smoothly according to:

$$\mathcal{T}(t) = \begin{cases} \sin^2\left(\frac{\pi t}{T_P}\right) & 0 < t < T_P \\ 0 & \text{otherwise} \end{cases}, \tag{4.9}$$

where T_P represents the duration of the perturbation. Thus, the time-dependent potential is:

$$\mathcal{U}(\mathbf{r}, t) = U(\mathbf{r})\mathcal{T}(t). \tag{4.10}$$

The time dependence of the perturbation geometry is shown visually in figure 4.1. Numerical renderings of the single-particle potential seen by the atoms are shown at five points in time during the perturbation. The left column uses color to qualitatively illustrate the red and blue beams ramping up and then down in intensity. The center column shows a vertical cross-section of the potential through the center of the trap. The right column is a two-dimensional map of the single-particle potential. In all three illustrations, the position coordinates are in units of the natural oscillator length. Accordingly, the BEC will be slightly smaller than the window shown.

There are several parameters of interest in this numerical study. The peak potential U_0, the beam separation $2d$, the perturbation time T_P, the beam width σ. From an experimental perspective, the most difficult parameter to alter is σ, which requires swapping out an optical telescope. The beam separation can be changed by adjusting folding mirrors, the perturbation time can be changed on the fly by adjusting numbers in the timing control sequence, and similarly the beam

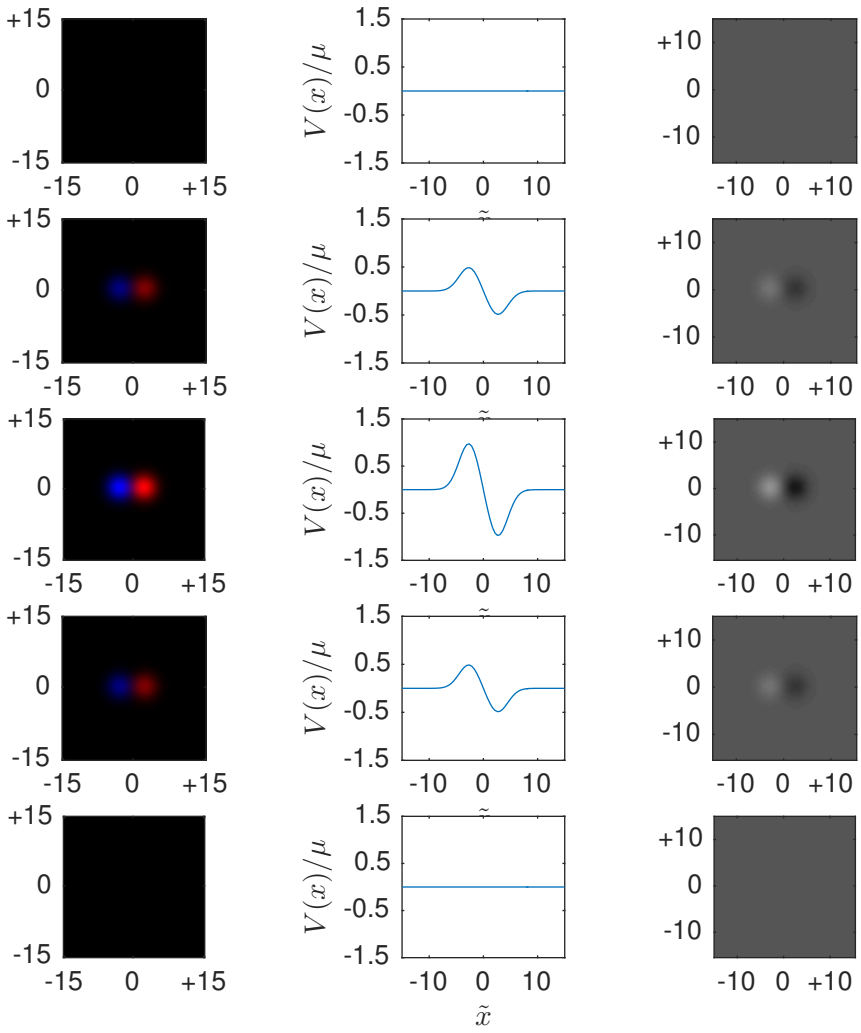

Figure 4.1: Visual illustration of the time varying perturbation. The left column illustrates the locations of the red and blue detuned beams. The central column depicts a horizontal cross-section of the potential perturbation seen by the atoms due to the perturbation. The right column depicts a two-dimensional view of the perturbation seen by the atoms. Lengths are scaled by the harmonic oscillator length.

amplitude can be changed by adjusting numbers in the timing control sequence. This study will focus on a single beam size ($\sigma = 10\mu m$), which corresponds to the beam sizes typically used in ^{87}Rb BEC experiments at the University of Arizona that involve optical stirring beams. The 10μm beam waist corresponds to approximately 25ξ, where $\xi \sim 0.28\ \mu$m is the healing length of the BEC.

4.3 Experimental configuration & constraints

The experimental setup is illustrated in figure 4.2. Two lasers are configured on separate optical breadboards. They are housed separately for two reasons: space constraints on the primary experiment table and to minimize stray light near the imaging camera. Each laser is capable of outputting about 150 mW. This is far more power than will be necessary. Both lasers are controlled with laser diode current drivers. Both current drivers accept an input voltage to modulate the diode current (20 mA/V). This input voltage will be controlled from the timing computer, which uses a Viewpoint DIO 128 Digital output card with 10 μsec time step resolution through a 16 bit 0-10V digital-to-analog converter in order to establish a time-dependent perturbing potential. The current drivers are preset to a base current that is just above the lasing threshold for each diode. This is done because over the course of the day the current will be ramped up and down tens or hundreds of times. Repeatedly and rapidly ramping the current through the lasing threshold can cause premature diode failure and should be avoided. Furthermore, the laser's output response is slow below the lasing threshold and nonlinear near the lasing threshold, whereas the laser's output power is approximately linear and relatively much more rapid above the lasing threshold. It is therefore much easier to predict the time-dependent perturbing potential's output power as a function of time if operated strictly within the lasing regime.

Each laser can be brought to focus through an AOM. The AOMs are electronically controlled by the timing computer and act as high speed shutters. In practice, the 850-nm beam uses an AOM as a shutter and the 660-nm beam uses a mechanical shutter, however, it is preferred to use AOMs for both shutters because of the much faster actuation. The AOMs have a rise time on the order of 20 ns, which is much faster than the 6 ms open/close time of the mechanical shutters.

Both lasers are independently coupled into single-mode optical fibers (F1,F2) to bring the light over to the optical table where the fiber is affixed to a fiber coupler/collimating package, which outputs a collimated beam. Each beam is then directed through a polarizing beam splitter cube. This serves two purposes: first to ensure the polarization of the light is known and secondly to pick off some light from each beam to send to a photodiode that is used to actively monitor laser power during the timing sequence.

The 850-nm laser is reflected by two steering mirrors (SM1 and SM2). These mirrors are steered by piezo-electric actuators. The piezo-electric actuator on the first mirror controls one axis and the piezo-electric actuator on the second mirror controls the other axis. These actuators are controlled by a voltage driver which is in turn controlled by an analog voltage from the timing computer. For the purpose of this specific experiment, the beams are held stationary; however, these actuators permit the 850-nm beam to be actively steered independent of the 660-nm beam during the timing sequence in time steps on the order of a ms.

The 660-nm laser is reflected by a flat mirror, M1, before being resized by a Newtonian telescope that consists of two lenses L5 and L6. This Newtonian telescope is used to resize the

660-nm beam such that when focused by the focusing objective, L9, both beams will focus down to the same spot size.

The two beams are combined with a non-polarizing beam splitter cube. A non-polarizing beamsplitter is preferred so that both beams have the same polarization. This is convenient because polarizing optics are used further down the optical path and it is desirable to have both perturbing beams interact with the polarizing optics in the same way.

After the two beams are combined by the non-polarizing beam splitter cube, there is a secondary Newtonian telescope that consists of two achromatic lenses. The purpose of this telescope is to increase the size of both beams such that the final focused beam size is smaller. The final focusing objective could also be adjusted to serve this purpose, however, geometry and space constraints require that the final focusing objective have no shorter than 90 mm focal length, which sets a lower bound on the input beam size for the desired focused beam size.

After the second Newtonian telescope there are two additional steering mirrors, SM3 and SM4, which again are outfitted with piezo-electric actuators and can be actively steered during the experiment. The previous set of steering mirrors adjusts the relative position of the 850-nm and the 660-nm beams to set the beam separation. This second set of steering mirrors, however, steers both beams simultaneously and is therefore used to position the perturbation on the BEC. This can be done actively during the experiment so that, for example, two vortex dipoles could be sequentially imprinted in different areas of the same BEC.

Finally, the achromatic focusing objective L9 is used to focus both the 660-nm and the 850-nm beams on to the BEC. As mentioned earlier, there is a geometric constraint that imposes a lower bound on the available focal lengths due to a beamsplitter cube that is necessary to permit a secondary light path to illuminate the BEC with collimated imaging light.

4.3.1 Choice of beam size

In general, the system has been designed with a final focused beam size in mind, a e^{-2} radius of $\sigma_r = 10\mu$m. The choice of beam size is for consistency with prior experiments in our lab that were conducted with a single 660-nm beam. Furthermore, much larger beam sizes are less favorable because they will be comparable to the BEC size itself, which would cause boundary effects to play a larger role in the observed dynamics and may also not produce dipoles as well. Much smaller beam sizes are increasingly difficult to achieve. The diffraction-limited focusing beam diameter is given by

$$d = \frac{\lambda}{2 \times \mathrm{NA}}, \tag{4.11}$$

where $\mathrm{NA} = D/f$ represents the numerical aperture of the focusing objective, D represents the diameter of the focusing objective, and f represents the focal length of the focusing objective. The same beam size is desired for both the 660-nm beam and the 850-nm beam, necessitating

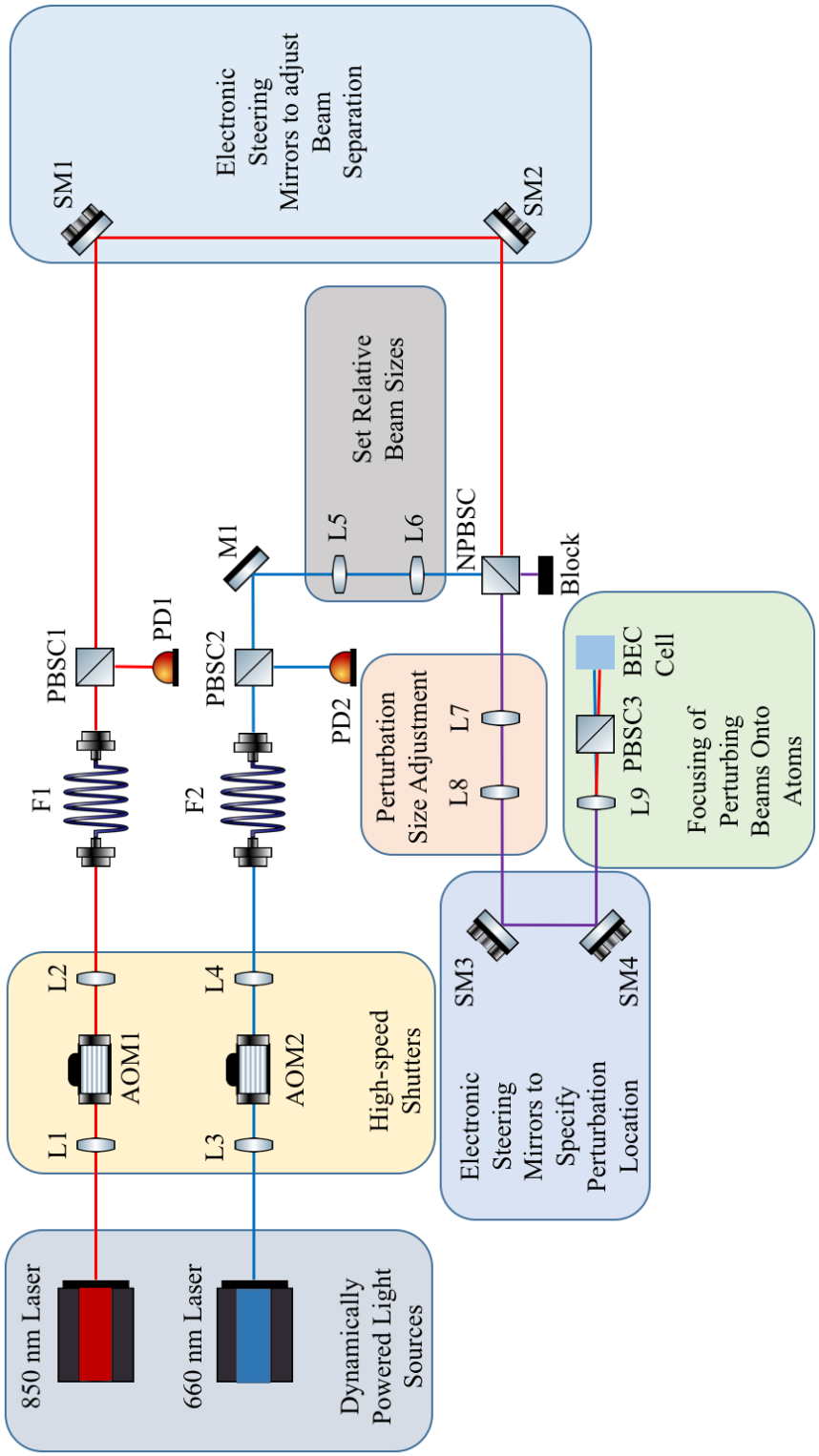

Figure 4.2: Experimental configuration.

that common path optics be achromatic. Geometric constraints set a lower bound on the final focusing objective to $f_{\text{obj}}^{(\text{min})} \approx 90$ mm.

Each beam will have a unique Rayleigh range:

$$z_r^{(\lambda)} = \frac{\pi \sigma_r^2}{\lambda}. \tag{4.12}$$

The focusing objective has a diameter of 25.4 mm, focal length 100 mm, and NA = 0.125. This corresponds to a 4.15 μm diffraction-limited spot size for 850-nm. The 10 μm experimental spot size is more than a factor of two above the theoretical minimum spot size in the current configuration, however, when keeping in mind that we desire to have steerable beams over a relatively wide field of view, it is increasingly difficult to maintain a small unaberrated spot size over the steering range.

Due to the inverse relationship between Rayleigh range and wavelength, the 850-nm laser will have a shorter Rayleigh range. Assuming a 10 μm e^{-2} spot radius, the 660-nm spot will have a 475 μm Rayleigh range and the 850-nm spot will have a 370 μm Rayleigh range. With knowledge of the Rayleigh ranges, the input beam radius is calculated according to:

$$\sigma_{\text{input}} = \sigma_r \sqrt{1 + \left(\frac{f_{\text{obj}}}{z_r}\right)^2}. \tag{4.13}$$

Assuming a 100-mm focal length objective and a 10 μm e^{-2} spot size, the upstream optical configuration must produce a 660-nm beam with 2.1 mm e^{-2} radius and a 850-nm beam with 2.7 mm e^{-2} radius. The 850-nm beam must be a factor of 1.3 larger than the 660-nm beam. This ratio will be constant regardless of desired final beam spot size. This will be convenient later if a different spot size is desired because only the final Newtonian telescope will need to be adjusted in order to achieve the new perturbation geometry.

In its current form, the final Newtonian telescope consists of two achromatic lenses with focal lengths of 100 mm and 150 mm. Together, they form a magnification 1.5X telescope. Because this telescope is achromatic, it will offer the same magnification to both the 850-nm and the 660-nm beams. Prior to the 1.5X magnification, the 660-nm and 850-nm e^{-2} beam waists $\sigma_1^{(\lambda)}$ must be 1.4 mm and 1.8 mm respectively, again maintaining the 1.29 ratio in relative beam sizes.

In order to set the proper beam size ratio, it is only necessary to adjust one of the optical paths and it should not matter which one. In the diagram shown in figure 4.2, the 660-nm beam is adjusted.

The initial beam size coming out of the fiber will be a function of the fiber mode, which will be approximately gaussian. The 660-nm laser and the 850-nm laser will each have different profiles coming out of the fiber. In particular, the 660-nm laser will have a fiber mode with radius $\sigma_f^{(660)}$ and the 850-nm laser will have a fiber mode with radius $\sigma_f^{(850)}$. Furthermore, the 660-nm path

will have a fiber coupler with focal length $f_{c,660}$ and the 850-nm laser will have a fiber coupler with focal length $f_{c,850}$. The initial collimated beam waists can again be calculated by considering the Rayleigh range of the respective fiber modes,

$$z_{r,f}^{(\lambda)} = \frac{\pi \sigma_f^{(\lambda)2}}{\lambda}. \tag{4.14}$$

From the Rayleigh range of the fiber, the initial collimated beam size is calculated.

$$\sigma_0^{(\lambda)} = \sigma_f^{(\lambda)} \sqrt{1 + \left(\frac{f_{c,\lambda}}{z_r^{(\lambda)}}\right)^2}. \tag{4.15}$$

In the experimental diagram shown, the 850-nm beam size is not adjusted with a telescope and therefore must be 1.8 mm at this point, which was a design constraint during the layout development. On the other hand, the 660-nm beam need not be the correct size because a Newtonian telescope with magnification $M = \frac{\sigma_1^{(660)}}{\sigma_0^{(660)}}$ is used to bring the beam up or down to size.

4.3.2 Choice of beam intensities

The 660-nm and the 850-nm beams serve as repulsive and attractive perturbations respectively. In the absence of the 850-nm beam, the 660-nm beam can serve as either a penetrable or an impenetrable barrier. A penetrable barrier serves as a sort of bump in the potential experienced by the atoms. This bump will in general reduce the local atom density, however, the local density will not necessarily be reduced by an order of magnitude or more. On the other hand, an impenetrable perturbation will forbid the presence of atoms in the locality of the perturbation. A useful metric for comparison is the chemical potential, which, like the amplitude of the perturbation, has units of energy. If the perturbation has an amplitude on the order of the chemical potential, an atom with a significant probability density at the peak of the perturbation will have potential energy on the order of the chemical potential. For an atom trap, this is a signifiant amount of excess energy for an atom to have. Consider the possibility of the atom density moving off the unstable equilibrium position that is the perturbation: this potential energy is then converted to kinetic energy. The chemical potential, by definition, is the amount of energy needed for an atom to enter or exit the trap. It therefore stands to reason that any atoms that have a significant probability density in the immediate vicinity of the peak perturbation will also have enough energy to leave the system.

The chemical potential thus serves as a useful scale by which to measure the perturbation amplitude. The perturbation itself is the result of the optical dipole force, which is the dominant effect of a far-detuned light source. What is meant by far-detuned is that the detuning from the atomic resonance (~780 nm) is much greater than the width of the atomic resonance (~ 6 MHz)

[87]. Both 850-nm and 660-nm light correspond to detuning at least six orders of magnitude larger than the atomic resonance, which is sufficient to be considered far-detuned.

It is helpful to know what optical intensity and optical powers correspond to the chemical potential for both the 660-nm and 850-nm beams and so I define reference intensities:

$$I_{\mu}^{(\lambda)} = \frac{2\omega_0^3}{3\pi c^2}\frac{\Delta}{\Gamma}\mu_{\mathrm{sys}}, \tag{4.16}$$

where μ_{sys} represents the chemical potential of the BEC. Within the Thomas-Fermi approximation, the ground-state chemical potential is given by [12]

$$\frac{\mu_{\mathrm{sys}}}{\hbar\bar{\omega}} = \frac{1}{2}\left(\frac{15Na_s}{\bar{r}}\right)^{2/5}, \tag{4.17}$$

where $\bar{r}$ is the geometric mean harmonic oscillator length, $\bar{\omega}$ represents the geometric mean harmonic oscillator frequency, N is the atom number, and $g = 4\pi\hbar^2 a/m$ where a is the s-wave scattering length. Using this form for the chemical potential and assuming experimental trap frequencies of 8 Hz and 90 Hz with an atom number of 1.7 million the reference beam intensities are calculated to be $I_{\mu}^{660} = 1.2 \times 10^5$ W/m^2 and $I_{\mu}^{850} = 6.52 \times 10^4$ W/m^2. The corresponding reference beam powers assuming a 10 μm beam waist are $I_{\mu}^{660} = 22.5\,\mu$W and $I_{\mu}^{850} = 13\mu$W.

4.3.3 Choice of beam separation

The spatial dependence of the perturbation is characterized by two parameters: beam waist and beam separation. The spatial dependence of the potential cross-section with beam separation $2x_0$ and beam radii σ, is given by

$$V \propto e^{-(x-x_0)^2/\sigma^2} - e^{-(x+x_0)^2/\sigma^2}. \tag{4.18}$$

The beam offset, x_0, can be chosen to maximize the central gradient. The central gradient is the derivative of the potential:

$$\left.\frac{\partial V}{\partial x}\right|_{x=0} \propto \frac{2(x_0)}{\sigma^2}e^{-x_0^2/\sigma^2} - \frac{2(x_0)^2}{\sigma^2}e^{-x_0^2/\sigma^2}. \tag{4.19}$$

The on-axis gradient can be maximized with respect to the beam offset parameter x_0:

$$\frac{d}{dx_0}\left[\left.\frac{\partial V}{\partial x}\right|_{x=0}\right] \propto \frac{8x_0}{\sigma^2}e^{-x_0^2/\sigma^2}\left(1 - \frac{x_0^2}{\sigma^2}\right). \tag{4.20}$$

The gradient is maximized when the beam offset, x_0, is set to the beam radius, σ. This will serve as a baseline beam offset; however, different offsets are examined numerically and the offset is found to affect the vortex dipole nucleation thresholds.

4.3.4 Choice of perturbation times

For the purpose of engineering arbitrary BEC wave functions, shorter time scales are more favorable. Any of the time scales discussed here are short enough to not be noticed by the equipment operators: the experiment itself has an approximately four minute duration and so whether this mechanism takes ten ms or ten seconds is insignificant. More importantly, however, it is desirable to have the vortex dipole nucleation method be as fast as possible so that another dipole could be placed elsewhere by the same mechanism without the system time evolving significantly. A good metric for the system's rate of time evolution is the radial trapping period, which is approximately 125 ms and corresponds to the 8 Hz radial trapping frequency. Ideally, the perturbation time will be much less than the radial trapping period. As will be seen later in the numerical results, however, it is found that the most stable regimes are for perturbation times slightly longer than the radial trapping period. This will still suffice, so long as the perturbation time is not much greater than the radial trapping period. A second reason that short perturbations are desirable is because of the limited BEC lifetime; however, the BEC lifetime is on the order of a minute and is not a limiting factor at this point in time.

4.4 Overview of explored parameter space

As was mentioned earlier, there are four characteristic parameters for the perturbation mechanism described in this chapter: beam width, beam separation, perturbation time, and perturbation amplitude. Beam width and beam separation both are relevant length scales. Perturbation time is a time scale, and perturbation amplitude is an energy scale.

The harmonic oscillator system has two characteristic length scales: the natural oscillator length r_0 and the healing length ξ. The healing length ξ is a function of the nonlinear parameter that depends on atom number in addition to the species, and so the more general natural oscillator length $r_0 = \sqrt{\hbar/m\omega}$ is the preferred length scale. The system has one characteristic timescale: the trap oscillator period $T = 2\pi/\omega$ and one characteristic energy scale: the chemical potential, μ. These characteristic scales serve as a starting point for guessing ideal parameters. For example, an initial trial guess could be a perturbation amplitude of μ, a perturbation time of $T_P = T$, and beam width on the order of the diffraction limit and a similar beam separation.

4.4.1 Time dependence

The initial trial configuration used is a beam width of $\sigma \approx 2.63 r_0$, which corresponds to a 10μm beam waist in the experimental apparatus. Initial beam separation is chosen to be $d = 3\sigma \approx 7.89 r_0$. The initial perturbation time is varied between $T_P = T/16$ and $T_P = 2T$. For each choice of perturbation time, simulations are run with varying intensities in an attempt to map out the threshold amplitude for vortex dipole nucleation as well as the upper threshold, above

which additional vortices or solitons are introduced beyond simply a vortex dipole. As expected, the threshold for vortex dipole nucleation varies significantly with the perturbation time. The resulting dataset is shown in figure 4.3.

The threshold intensity for dipole nucleation appears to be approximately linear with perturbation time. Below a perturbation time of $T_P \approx T$, or one period of the radial trap frequency, it is difficult to generate a stable dipole without other excitations such as sound waves or additional dipoles. For a perturbation lasting approximately one period of the radially trapping geometry and longer, a window in parameter space opens up where dipoles are easily introduced without many other excitations. This has been observed for all of the parameters explored and I hypothesize that it has to do with the system allowing time for the fluid to be pushed to one side and then return. Vortex dipoles could be nucleated for shorter perturbation times; however, it appears to be a different and less favorable mechanism at work that tends to also introduce large quantities of sound waves.

4.4.2 Dependence on beam separation

The threshold intensities for vortex dipole nucleation were also checked against the spatial separation of the red and blue beams. Once again, there is a lower bound below which only sound waves are generated and an upper bound above which vortex dipoles are nucleated with additional sound waves, Jones-Roberts solitons, and/or vortices.

The numerical data for these thresholds are illustrated in figure 4.4. Of note, for wide enough beam separation there is no stable regime to create a single vortex dipole with minimal other excitations. This is not surprising and most likely because significant edge effects come into play. For increasingly small beam separations, the intensity threshold increases exponentially. This is again not surprising because for increasingly small separations the two beams increasingly negate each other's effect. For zero beam separation, the two beams would be overlapped and there would be exactly zero shift in the local single-particle potential energy seen by the atoms.

The effect of underpowered, critically powered, and overpowered perturbation intensities are shown in figure 4.5. For the case of underpowered, residual excitations are seen on the perimeter of the BEC, however, no vortices are present. In the critically powered case, there are fewer sound excitations than in the underpowered case, and additionally, there is a vortex dipole present. In the overpowered case, there is a vortex dipole present but also sound waves are visible on the perimeter in addition to two additional edge-vortices that can be seen at the 2 o'clock and 4 o'clock positions.

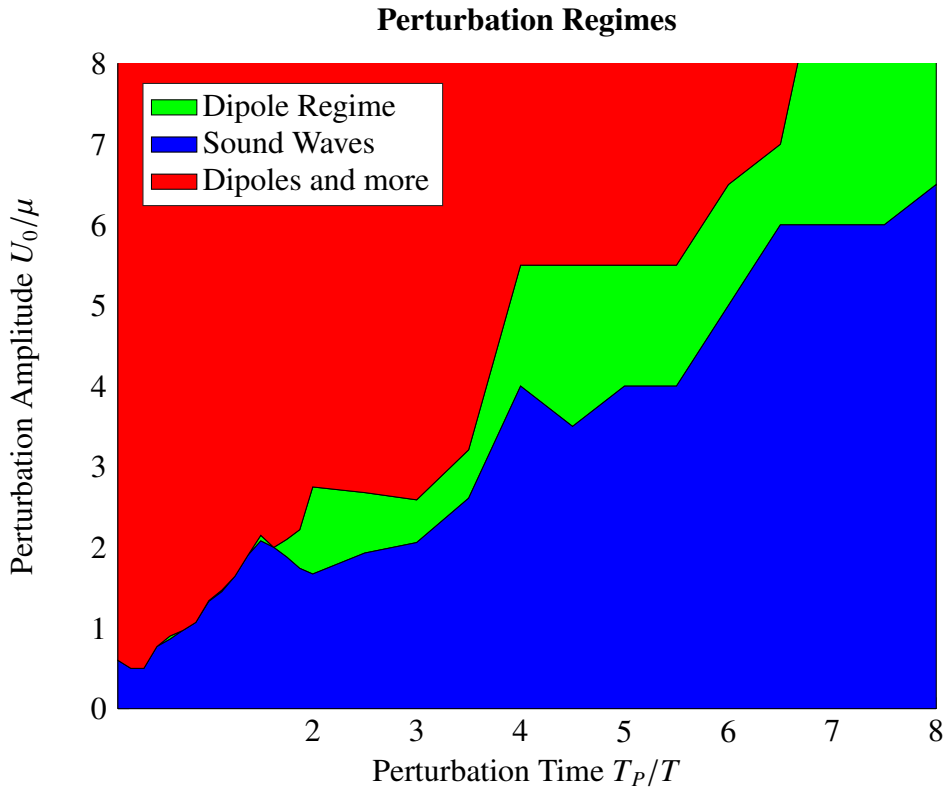

Figure 4.3: Investigation of intensity and time dependence of perturbation on vortex dipole nucleation. Below a threshold (blue region) only sound waves are formed. In some instances, these sound waves take the form of Jones-Roberts solitons. At lower intensities these excitations damp out, whereas at intensities closer to the vortex dipole nucleation threshold they decay into vortex dipoles near the BEC perimeter. Sufficiently high intensities introduce extraneous excitations in the form of sound waves, Jones-Roberts solitons, or vortices in addition to the desired vortex dipole. This region in parameter space is shown here in red. The beam waist is $\sigma = 2.63r_0$ where r_0 is the natural harmonic oscillator length and the beam separation is $d_{\text{sep}} = 3\sigma$.

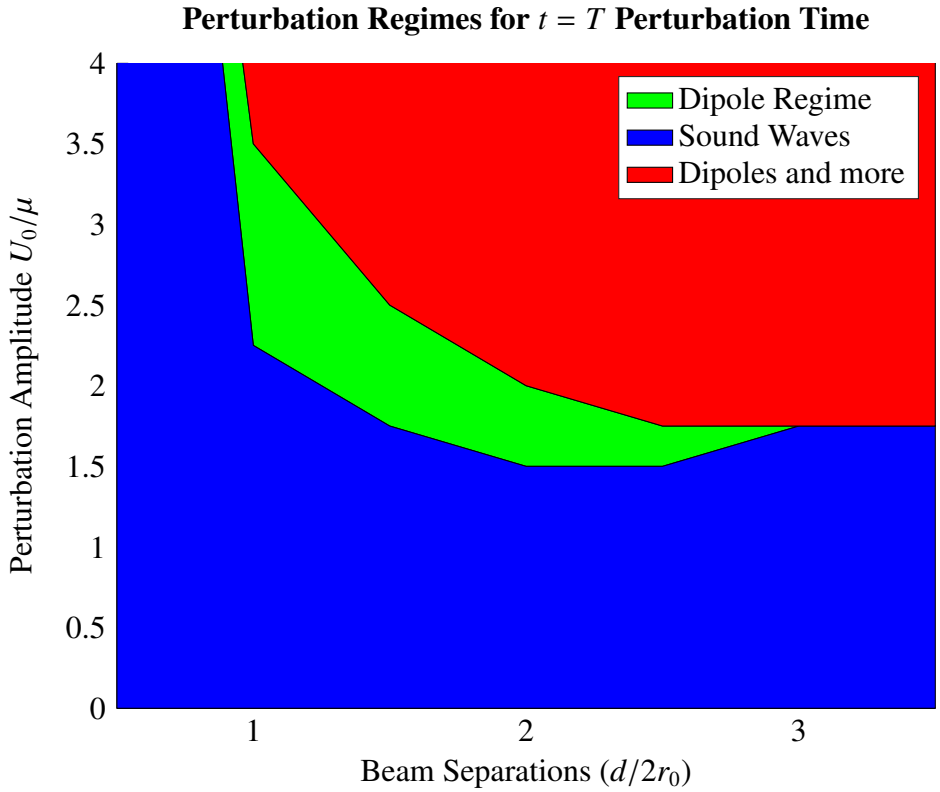

Figure 4.4: Dependence on separation between repulsive and attractive perturbations on vortex dipole nucleation threshold. The beam waist is $\sigma = 2.63r_0$ where r_0 is the natural harmonic oscillator length. The perturbation time is $T_P = T$.

4.4.3 Dependence on beam size

In this subsection, the dependence of threshold intensities on beam size is investigated. In order to do a controlled study, the beam separations are scaled with beam size: $d = 2\sigma$. Furthermore, the perturbation time is held constant at $T_P = 5T/4$, which corresponds to one of the most promising areas in parameter space explored earlier as depicted in figure 4.3. The beam size was varied from r_0 to $3.5r_0$ in steps of $0.5r_0$ where r_0 is the natural oscillator length. In the corresponding experiment, the actual beam size (10μm) corresponds to approximately $2.63r_0$.

The numerical findings are shown in figure 4.6. In this controlled numerical study, there was no stable vortex dipole nucleation regime for beam waists $\sigma/r_0 < 1.5$. Instead, weak perturbations yielded only sound waves and stronger perturbations yielded a mix of vortices and sound waves, but with no clear dipolar fluid flow.

As the beam waist is increased, an area of parameter space opens up where vortex dipoles are nucleated without excessive acoustic excitations. The optimal beam waists appear to be

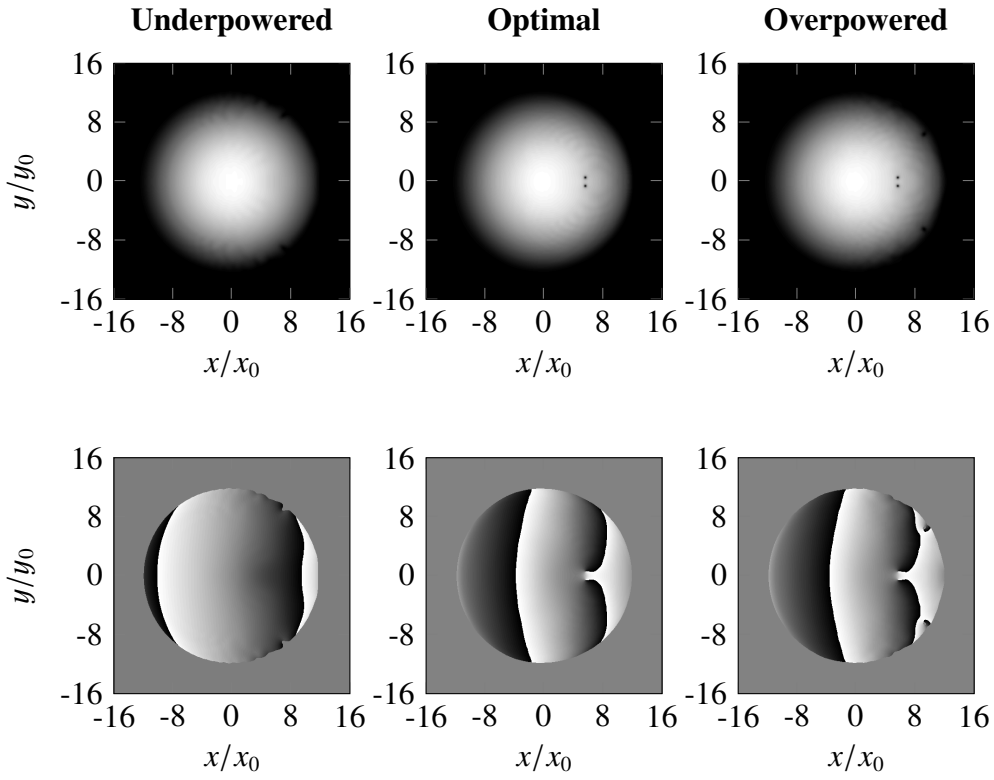

Figure 4.5: The leftmost image depicts a simulated BEC with an underpowered perturbation. Small acoustic wave ripples are visible, especially around the perimeter. In center, a simulated BEC after an optimally powered perturbation is shown. Note the presence of a vortex dipole and the absence of acoustic wave ripples around the perimeter. On the right, a simulated BEC after an overpowered perturbation is shown. Note that in addition to a vortex dipole, acoustic waves are seen, and in particular, additional vortices are seen on the perimeter; these are the result of an acoustic wave that broke up into vortices in the low density cloud perimeter. The top row depicts the local density profile and the lower image depicts the local phase.

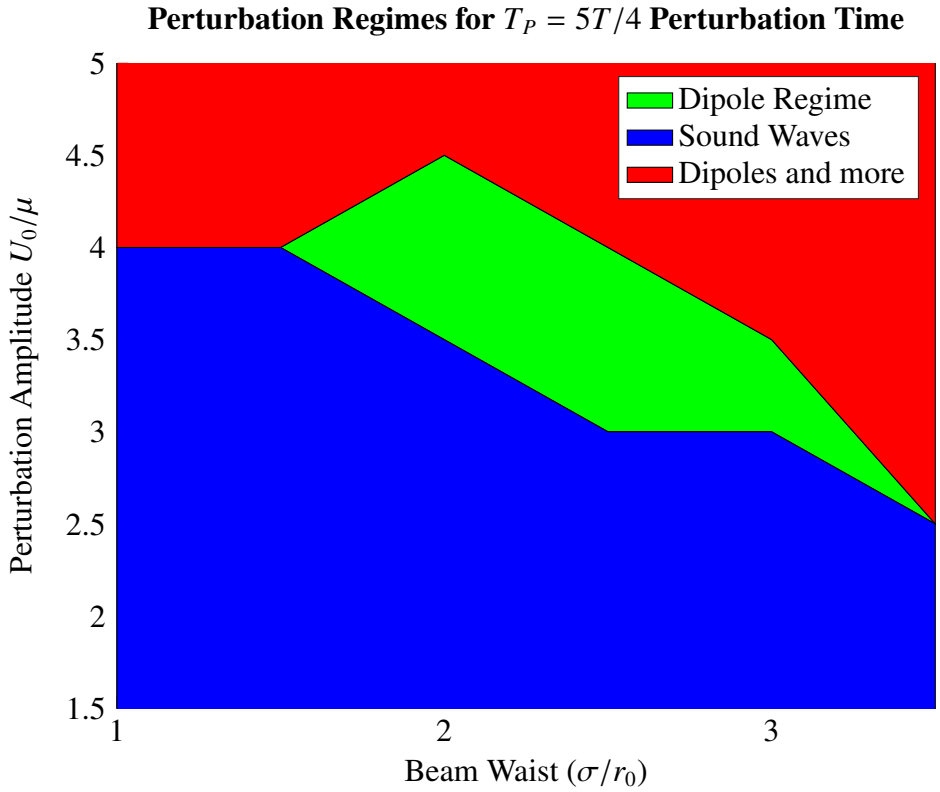

Figure 4.6: This figure illustrates the perturbation intensity thresholds for vortex dipole nucleation as a function of perturbation beam waist. The beam offset is scaled with the beam waist as $\Delta x = \sigma$ in this dataset. The perturbation time is held constant at $T_P = 5T/4$.

between $2r_0$ and $3r_0$ in this configuration. Increasingly larger perturbation sizes come with a lower threshold for vortex dipole nucleation and also a lower threshold for additional excitations. This is not surprising because a larger perturbation with the same amplitude will have a larger net energy exchange with the atoms due to the larger effective interaction area. Ultimately, large enough beams close the gap between vortex dipole nucleation and more chaotic systems with unwanted excitations. This is likely due to boundary effects. A further study of this mechanism in a homogeneous medium would improve our understanding of the mechanisms at work here by ruling out boundary conditions.

To further understand the dependence on beam separation, the numerical investigation of intensity threshold as a function of perturbation time which was discussed briefly earlier in the temporal dependence subsection is extended to identify the regions for vortex dipole nucleation with three different beam separations: $d = 2\sigma$, $d = 3\sigma$, and $d = 4\sigma$, where $\sigma = 2.63r_0$ is the beam size which corresponds approximately to the experimental beam and r_0 is the natural oscillator length of the radial trapping geometry. This dataset is shown in figure 4.7. In all three

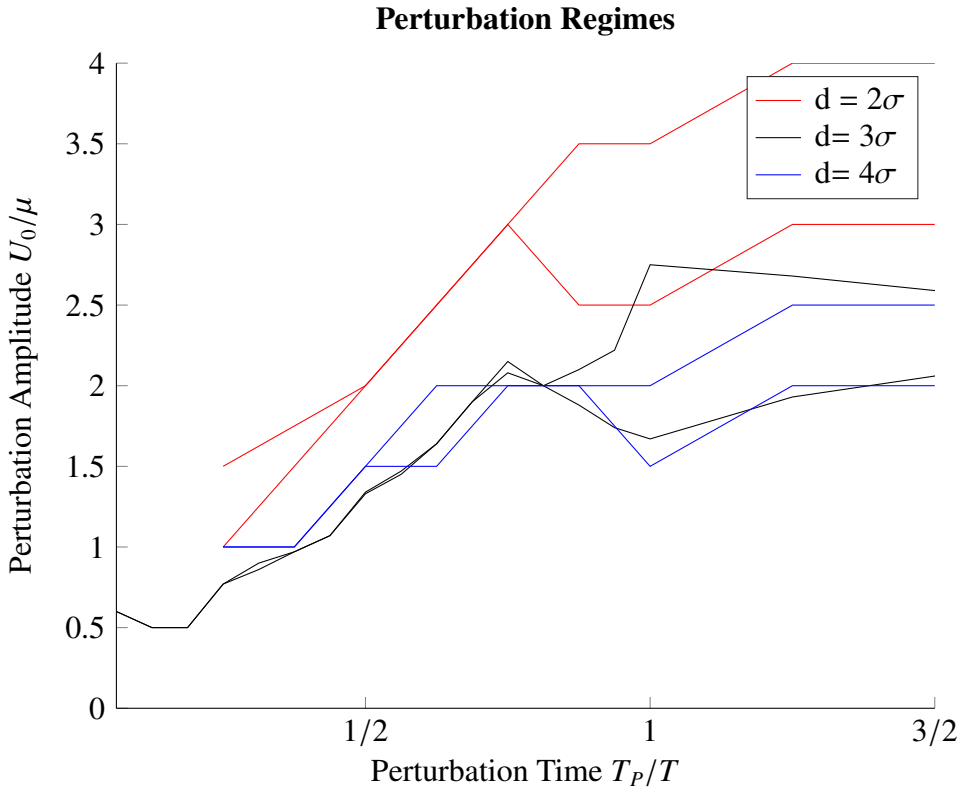

Figure 4.7: The intensity threshold as a function of perturbation time is investigated for three different beam separations: $d = 2\sigma, d = 3\sigma$, and $d = 4\sigma$. In each case, the lower threshold for vortex dipole nucleation and the upper threshold before additional undesirable excitations (large sound waves, vortices, and solitons) are shown. In all three cases the beam separations from center are scaled with beam size: $d = 2\sigma$.

cases vortex dipoles are not nucleated for short perturbation times $T_P \lesssim 7/8T$ without excessive unwanted excitations. The smaller beam separation consistently has higher intensity thresholds. This is unsurprising because the smaller beam separations have smaller interaction areas and a smaller net energy transfer to the atoms. The cases of $d = 3\sigma$ and $d = 2\sigma$ have about the same threshold for vortex dipole nucleation; however, the threshold for undesirable excitations is lower for the $d = 4\sigma$ scenario, presumably because boundary effects are playing a larger role in the dynamics. This finding suggests that larger beam separations simplify the vortex dipole nucleation process; however, there is a diminishing return when pursuing larger beam separations in a finite sized BEC due to boundary interactions.

4.5 Analysis

In the previous section the parameter space for vortex dipole nucleation was explored with specific regard to beam size, beam separation, and perturbation time. In this section, the dynamics of a single vortex dipole nucleation event via this perturbation method are investigated in greater detail.

Figure 4.8 shows a sequence of three snapshots taken at different times during one numerical wave propagation that ultimately results in the nucleation of a vortex dipole. In the first snapshot (top row) the perturbation is being ramped on. In the second snap shot (middle row), the perturbation is being ramped off. In the third and final snap shot (bottom row), the perturbation has been ramped off completely. For each snapshot, four images are shown. The leftmost column illustrates the probability density of the wave function. The second column illustrates the phase. The third column illustrates momentum vectors, which is the velocity vector multiplied by the local density profile in the leftmost column. The momentum illustration shows only a subregion in the vicinity of where the vortex dipole nucleates. The subregion shown is ensquared by red in the leftmost column. The far right column illustrates the single particle potential as seen by the atoms.

In the first snapshot, as the perturbations are both ramped on, there are two phenomena taking place. The repulsive barrier on the left is pushing atoms radially outward from its center position. Second of all, the attractive well created by the 850-nm beam on the right pulls the atoms in. The attractive nature of this well pulls the wave function past and around the repulsive barrier. In some ways, the wave function in the immediate vicinity of the repulsive barrier is similar to what would be seen by an atom wave moving past a stationary barrier or a moving barrier slicing through the atom wave. Both of these scenarios are known methods for nucleating a vortex dipole [14].

In the second frame (middle row) the potential barrier on the left and the potential well on the right are ramping down. As a result, superfluid flow in the vicinity of the attractive well reverses direction and is now directed leftward; however, the fluid immediately to the left of the repulsive barrier, which was previously shielded from the attractive well by the repulsive barrier, is now flowing toward the right to fill in the vacuum where the repulsive barrier was. This position dependence of velocity direction results in a rotation of the vector field.

In the third frame (bottom row) the fluid flow breaks down into a vortex dipole. Of particular note is the highly localized nature of the fluid flow; the viewing windows is zoomed in by a factor of eight in order to identify the flow pattern and the uniform highly dipolar bulk fluid flow in general.

In order to form a vortex dipole, the integrated phase gradient over some finite region must exceed π in order to establish a 2π phase winding around a quantized vortex and so this spatial phase change can be used as a metric to analyze what is physically happening in the case of a critically powered, underpowered and overpowered perturbation. To illustrate this further, I examine

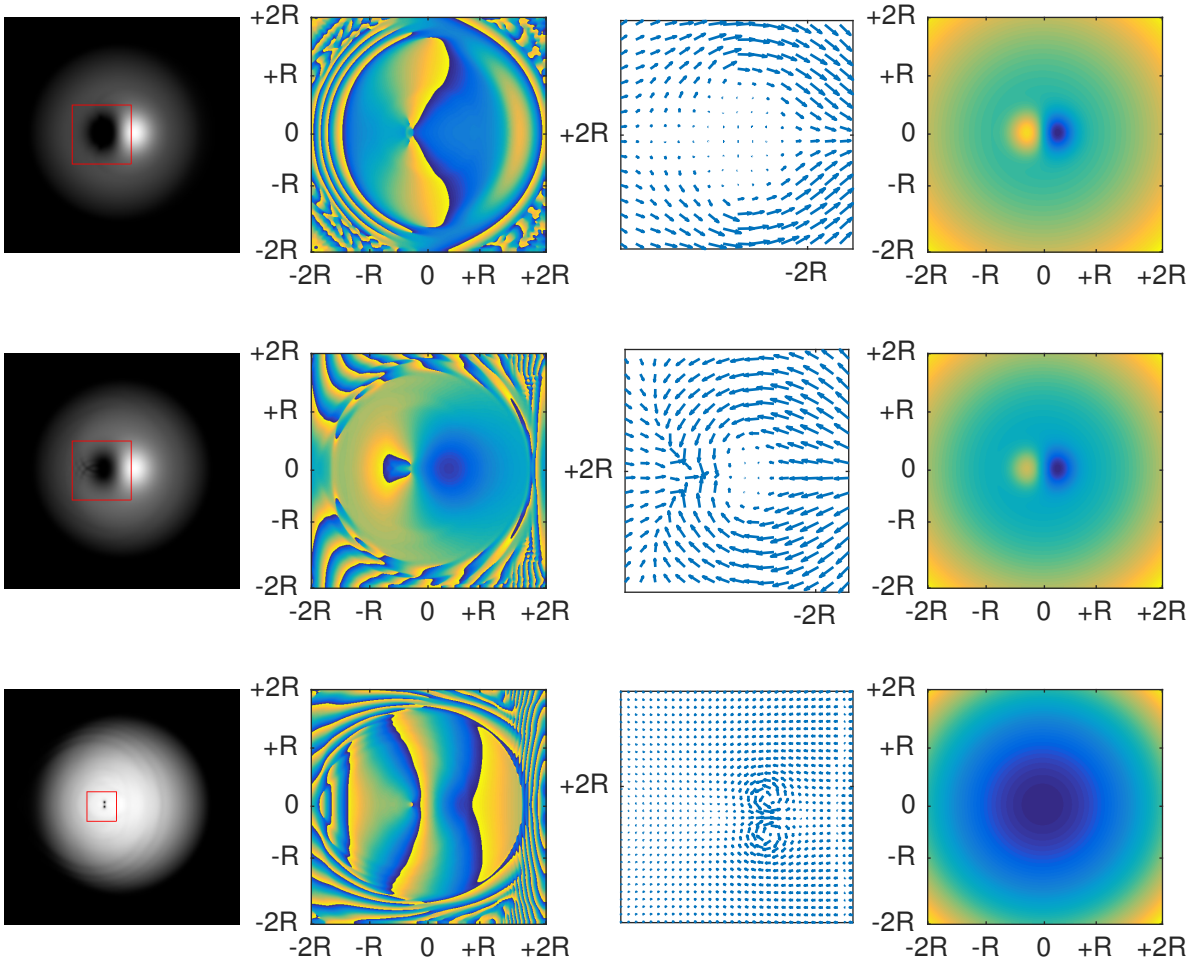

Figure 4.8: A more detailed description of this figure is in section 4.5. The left column shows column density, second from left shows phase, third from left shows local momentum vectors, and fourth column shows a cross-section of the phase from left to right. Top row is shown as the perturbation is ramping up, middle row is during perturbation ramp down, and the bottom row is after the perturbation is completely ramped off.

snapshots in fine time steps (1/20 of the natural harmonic oscillator period) of the dynamics in the critically powered, underpowered, and overpowered perturbations in figures 4.9-4.12, 4.13-4.16, and 4.17-4.20 respectively.

4.5.1 The critically powered case

Figures 4.9, 4.10, 4.11 and 4.12 illustrate 16 time steps surrounding the imprinting of a vortex dipole using this perturbation process for the critically powered case with peak amplitude $V = 2\mu$, beam waist $\sigma = 2.63r_0$ where r_0 is the natural oscillator length, beam separation $2d = 3\sigma$ and

perturbation time equal to the natural oscillation period of the harmonic oscillator. The beginning of a vortex dipole is visible in the phase diagram starting in frame 6 (row 2 of figure 4.10) as two localized phase discontinuities. Dipolar fluid flow can be seen beginning in frame 12 (row 4 of figure 4.11 and furthermore a phase variation develops that exceeds π but for the majority of the time does not exceed 2π except for very briefly in frame 8 (row 4 of figure 4.10) and again in frame 11 (row 3 of figure 4.11).

The first of these two instances of high phase gradient (frame 8, which is row 4 of figure 4.10) corresponds to a relatively steep phase gradient but also a change in the phase derivative sign: the phase derivative (left to right) sign changed from negative in frame 7 to positive in frame 8 and goes negative again in frame 9. Frame 8 corresponds to $t = 0.55T$ and because the perturbation time is exactly one period of the natural oscillator frequency in this case, this frame corresponds to the first frame when the perturbation is being ramped down rather than up and so it is not surprising that the phase gradient and thus fluid velocity would change direction at this point in time.

From frame 11 to frame 12 the sign of the phase derivative changes again from negative to positive and this time remains positive as the fluid begins to sustain dipolar fluid flow. This instance corresponds to $t = 0.70T$, which is also significant. The perturbation maximum amplitude in this case is 2μ and is modulated with respect to time such that $V(t) = 2\mu \sin^2(t/2T_P)$; as the perturbation ramps down it will drop below the chemical potential at $t \approx 0.79$. In the time frame corresponding to frames 11-13 (figure 4.11 rows 3-4, figure 4.12 row 1), the cross-sectional area of the repulsive barrier that exceeds the chemical potential of the system in amplitude is decreasing rapidly and as such the cross-sectional area of the repulsive barrier that is effectively impenetrable barrier ($V > \mu$) is also rapidly decreasing. It is no surprise then that the fluid flow comes crashing in rapidly. It is at this point in time that dipolar fluid flow becomes clearly visible and shortly thereafter in frames 15-16 (figure 4.12 rows 3-4) an energetically stable vortex dipole is clearly visible in the density profile.

4.5.2 The underpowered case

Figures 4.13, 4.14, 4.15, and 4.16 illustrate the same 16 time steps as above but for an underpowered perturbation with peak amplitude $V = 1.5\mu$ where no vortex dipole is nucleated, beam waist $\sigma = 2.63r_0$ where r_0 is the natural oscillator length, beam separation 3σ and perturbation time equal to the natural oscillation period of the harmonic oscillator. In time step 6 of the critically powered case (figure 4.10 row 2) two distinct phase discontinuities are first visible. By contrast, in frame 6 of the underpowered case (figure 4.14 row 2) no such phase discontinuities are evident. By inspection of the momentum diagram in frame 10 of the critically powered case (figure 4.11 row 2) the rightmost fluid flow direction has already reversed and is in general moving to the left; however, the repulsive barrier is still strong enough to force the returning fluid flow around the

barrier resulting in a dipolar fluid flow. Again by contrast, in frames 10-12 of the under powered case (figure 4.15 rows 2-4) the return fluid flow from the right is able to overcome the repulsive barrier, which is not as high as in the critically powered case and so dipolar fluid flow is almost (particularly in figure 4.15 row 4) but not quite established, hence this series of time steps illustrates an underpowered perturbation.

4.5.3 The overpowered case

Figures 4.17, 4.18, 4.19, and 4.20 illustrate the same time steps for an overpowered perturbation resulting in multiple vortex dipoles and additional sound waves. The peak amplitude $V = 3\mu$, beam waist $\sigma = 2.63r_0$ where r_0 is the natural oscillator length, beam separation 3σ and perturbation time equal to the natural oscillation period of the harmonic oscillator. This example serves to illustrate that in addition to dipolar fluid flow, stray vortex dipoles and unwanted sound waves are also introduced when the vortex dipole imprinting mechanism is overpowered. This is the result of far more energy being imparted on the system than is necessary for a single vortex dipole to be nucleated and in the presence of little or no damping the excess energy must go somewhere. The unwanted excitations in the system are consistently visible by inspecting the phase diagrams but they are also evident as density fluctuations in the second half of the time frames, most notably frames 15-16 (figure 4.20 rows 3-4).

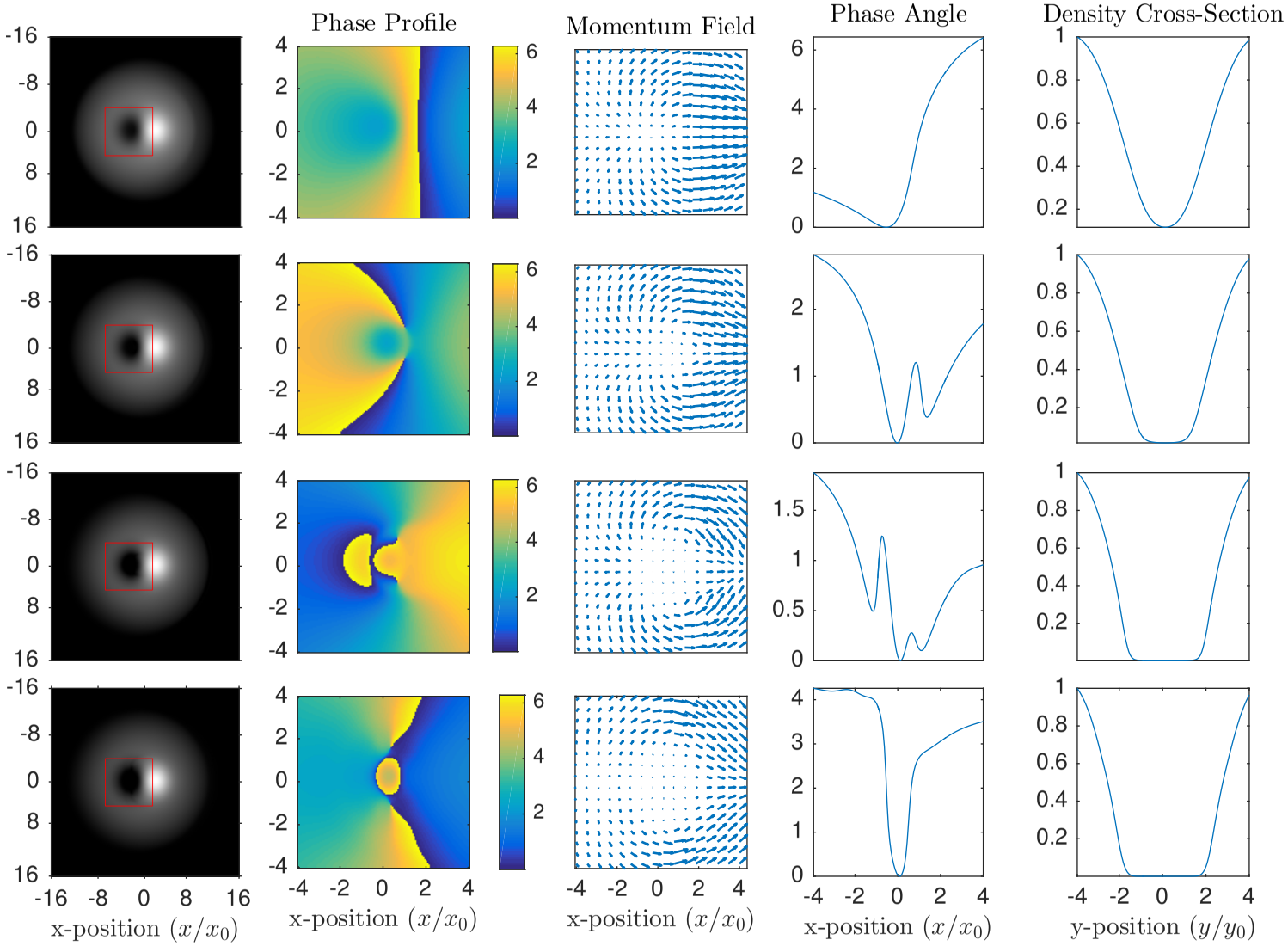

Figure 4.9: Critically powered Vortex Imprinting Case: time steps 1-4. First Row: $t = 0.20T$. Second Row: $t = 0.25T$. Third Row: $t = 0.30T$. Fourth Row: $t = 0.35T$. Lengths are scaled by the natural oscillator length. Column 1: density profile. Red coloring encircles the insets described in columns 2-5. Column 2: phase profile - area corresponds to red square in column 1. Column 3: momentum vector field - area corresponds to red square in column 1. Column 4: phase cross-section corresponding to x-path through center of red square in column 1. Column 5: density cross-section corresponding to y-path through center of red square in column 1.

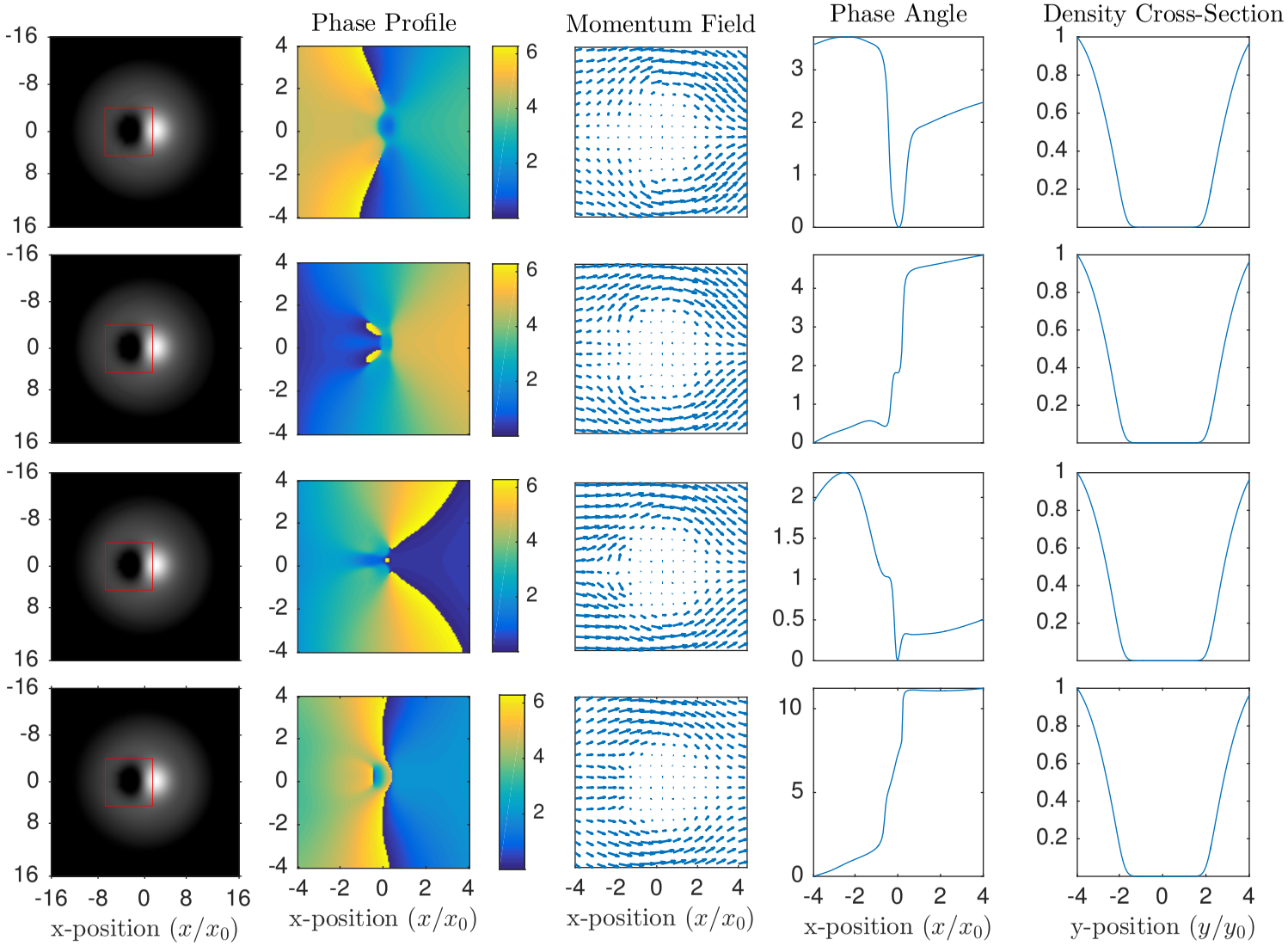

Figure 4.10: Critically powered Vortex Imprinting Case: time steps 5-8. First Row: $t = 0.40T$. Second Row: $t = 0.45T$. Third Row: $t = 0.50T$. Fourth Row: $t = 0.55T$. Lengths are scaled by the natural oscillator length. Column 1: density profile. Red coloring encircles the insets described in columns 2-5. Column 2: phase profile - area corresponds to red square in column 1. Column 3: momentum vector field - area corresponds to red square in column 1. Column 4: phase cross-section corresponding to x-path through center of red square in column 1. Column 5: density cross-section corresponding to y-path through center of red square in column 1.

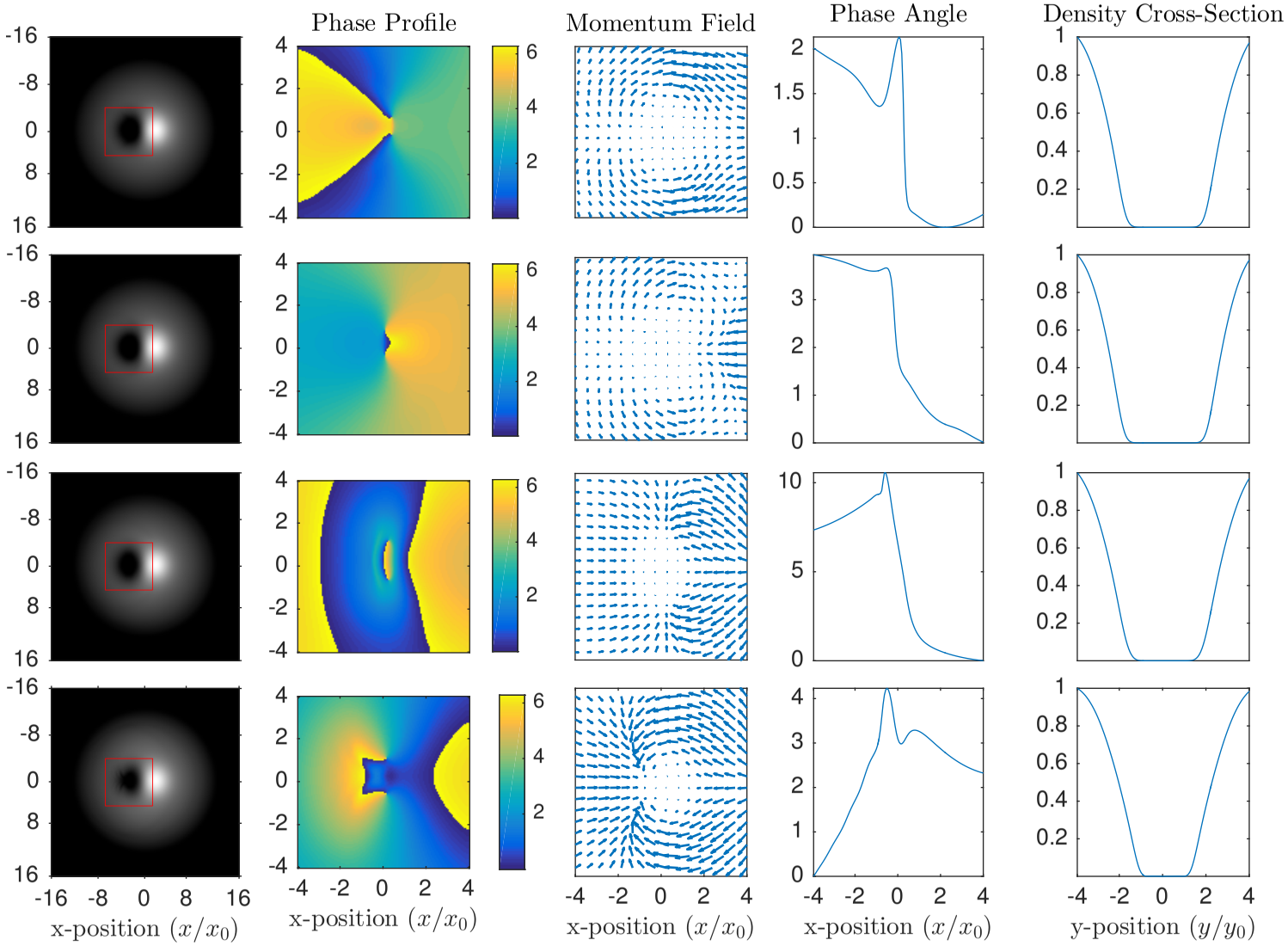

Figure 4.11: Critically powered Vortex Imprinting Case: time steps 9-12. First Row: $t = 0.60T$. Second Row: $t = 0.65T$. Third Row: $t = 0.70T$. Fourth Row: $t = 0.75T$. Lengths are scaled by the natural oscillator length. Column 1: density profile. Red coloring encircles the insets described in columns 2-5. Column 2: phase profile - area corresponds to red square in column 1. Column 3: momentum vector field - area corresponds to red square in column 1. Column 4: phase cross-section corresponding to x-path through center of red square in column 1. Column 5: density cross-section corresponding to y-path through center of red square in column 1.

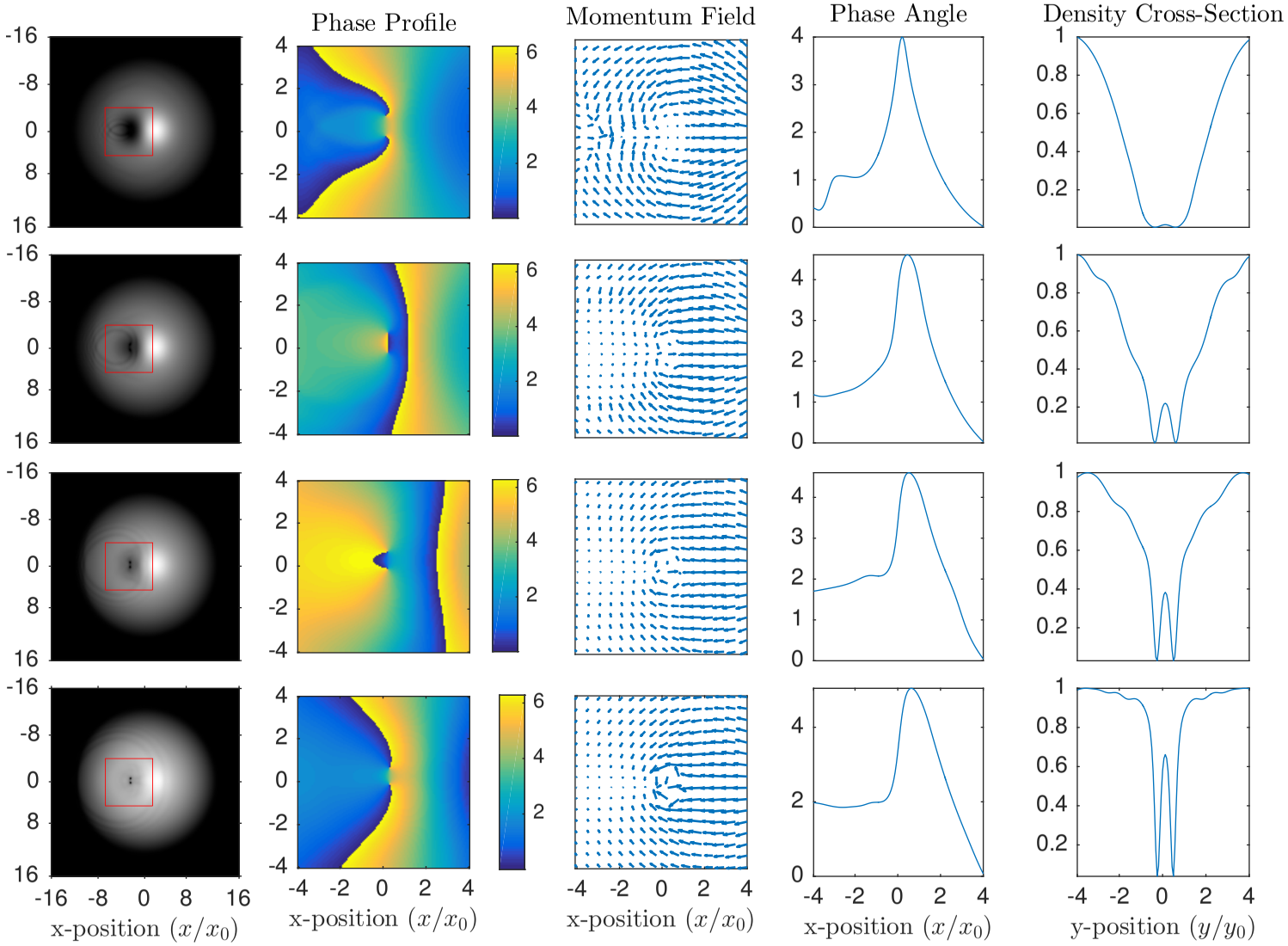

Figure 4.12: Critically powered Vortex Imprinting Case: time steps 13-16. First Row: $t = 0.80T$. Second Row: $t = 0.85T$. Third Row: $t = 0.90T$. Fourth Row: $t = 0.95T$. Lengths are scaled by the natural oscillator length. Column 1: density profile. Red coloring encircles the insets described in columns 2-5. Column 2: phase profile - area corresponds to red square in column 1. Column 3: momentum vector field - area corresponds to red square in column 1. Column 4: phase cross-section corresponding to x-path through center of red square in column 1. Column 5: density cross-section corresponding to y-path through center of red square in column 1.

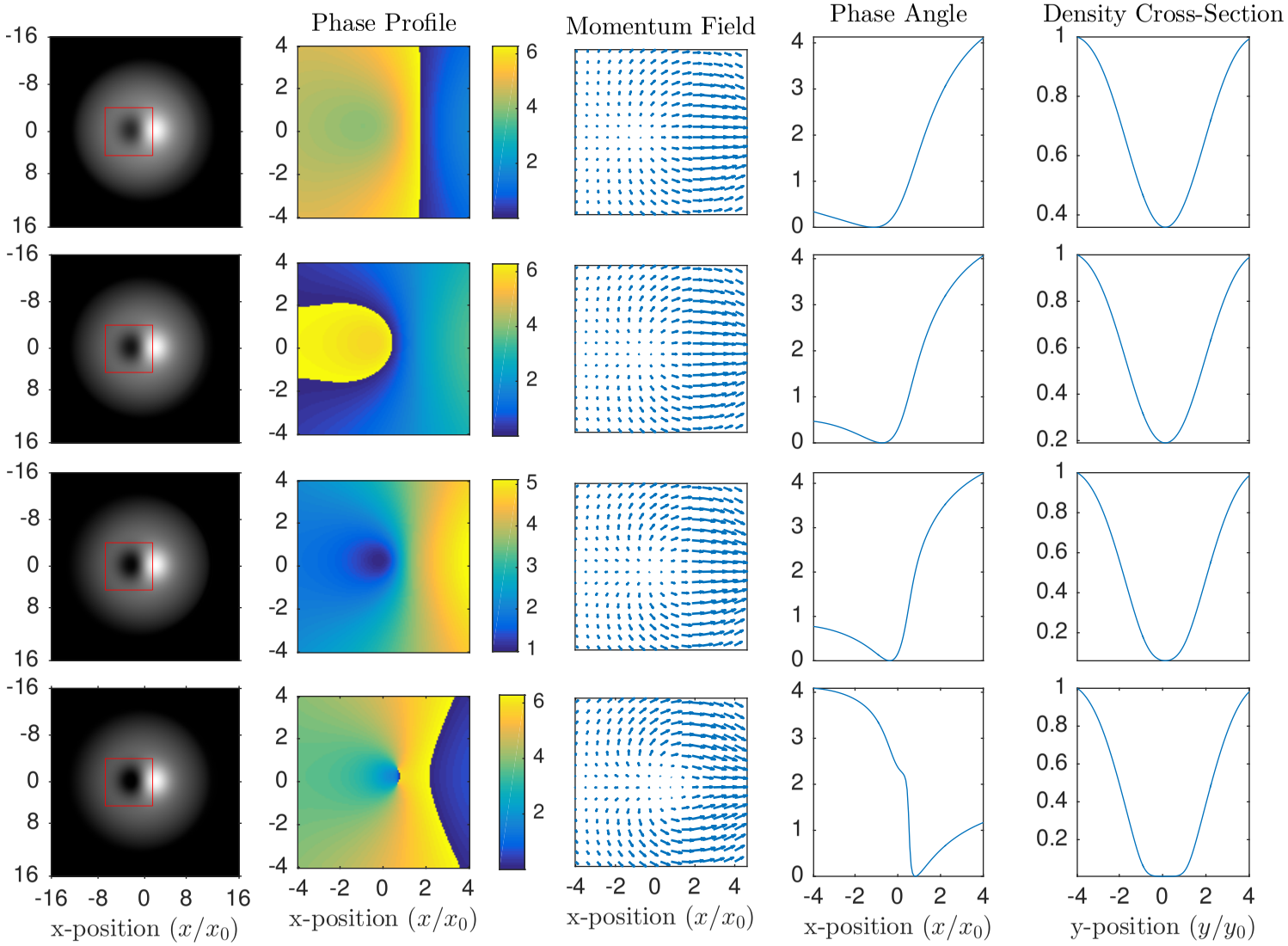

Figure 4.13: Under powered Vortex Imprinting Case: time steps 1-4. First Row: $t = 0.20T$. Second Row: $t = 0.25T$. Third Row: $t = 0.30T$. Fourth Row: $t = 0.35T$. Lengths are scaled by the natural oscillator length. Column 1: density profile. Red coloring encircles the insets described in columns 2-5. Column 2: phase profile - area corresponds to red square in column 1. Column 3: momentum vector field - area corresponds to red square in column 1. Column 4: phase cross-section corresponding to x-path through center of red square in column 1. Column 5: density cross-section corresponding to y-path through center of red square in column 1.

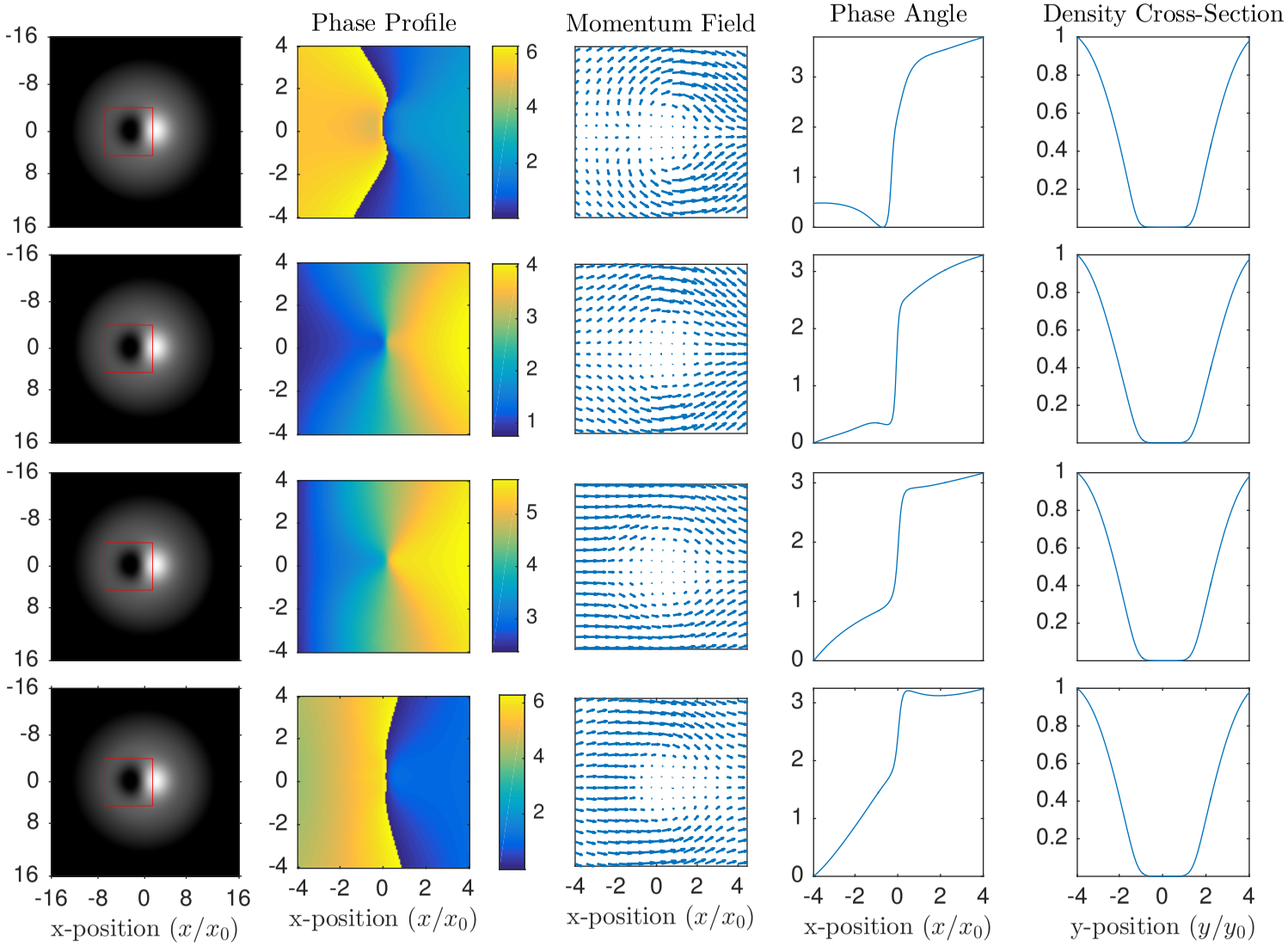

Figure 4.14: Under powered Vortex Imprinting Case: time steps 5-8. First Row: $t = 0.40T$. Second Row: $t = 0.45T$. Third Row: $t = 0.50T$. Fourth Row: $t = 0.55T$. Lengths are scaled by the natural oscillator length. Column 1: density profile. Red coloring encircles the insets described in columns 2-5. Column 2: phase profile - area corresponds to red square in column 1. Column 3: momentum vector field - area corresponds to red square in column 1. Column 4: phase cross-section corresponding to x-path through center of red square in column 1. Column 5: density cross-section corresponding to y-path through center of red square in column 1.

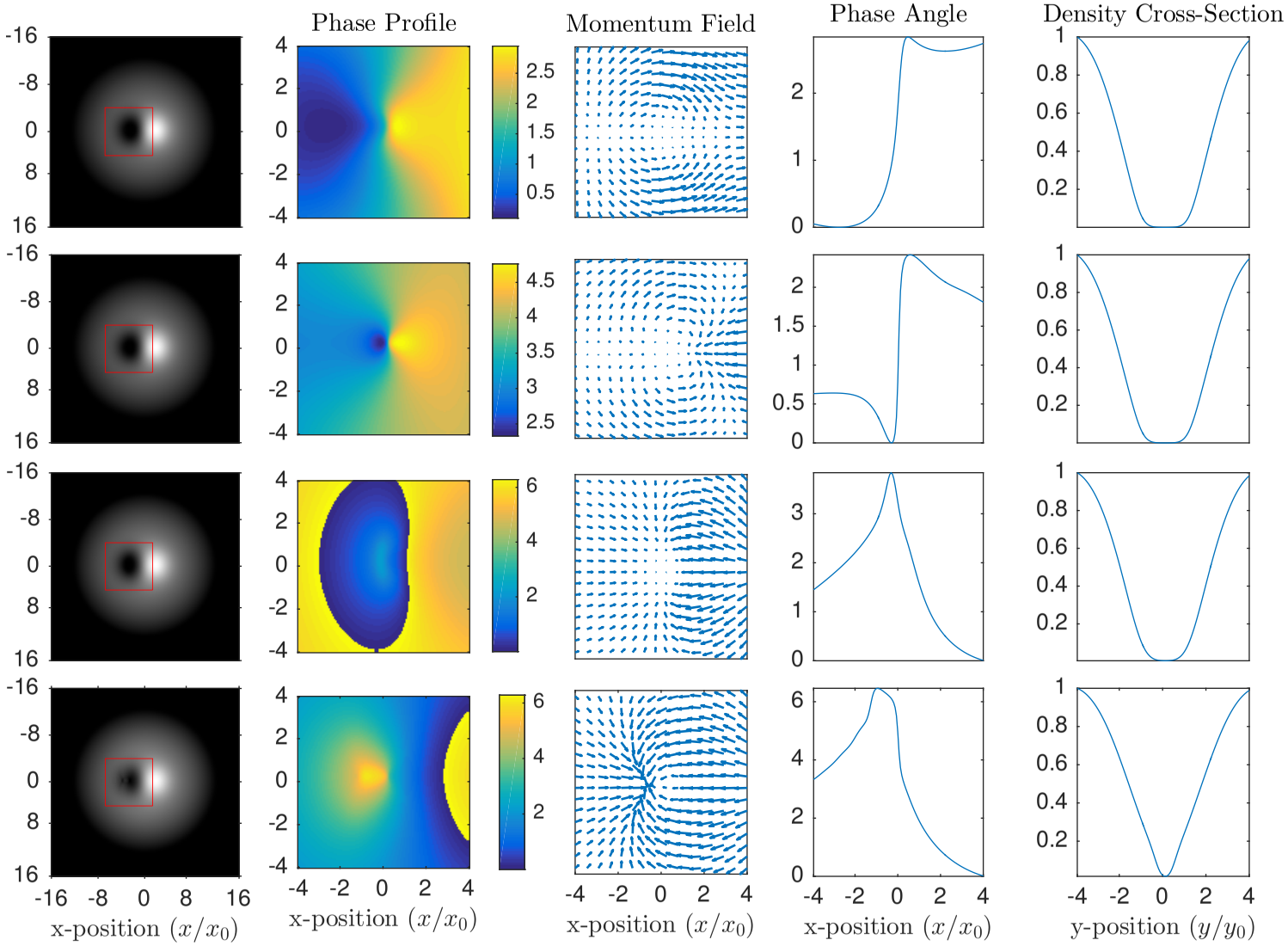

Figure 4.15: Under powered Vortex Imprinting Case: time steps 9-12. First Row: $t = 0.60T$. Second Row: $t = 0.65T$. Third Row: $t = 0.70T$. Fourth Row: $t = 0.75T$. Lengths are scaled by the natural oscillator length. Column 1: density profile. Red coloring encircles the insets described in columns 2-5. Column 2: phase profile - area corresponds to red square in column 1. Column 3: momentum vector field - area corresponds to red square in column 1. Column 4: phase cross-section corresponding to x-path through center of red square in column 1. Column 5: density cross-section corresponding to y-path through center of red square in column 1.

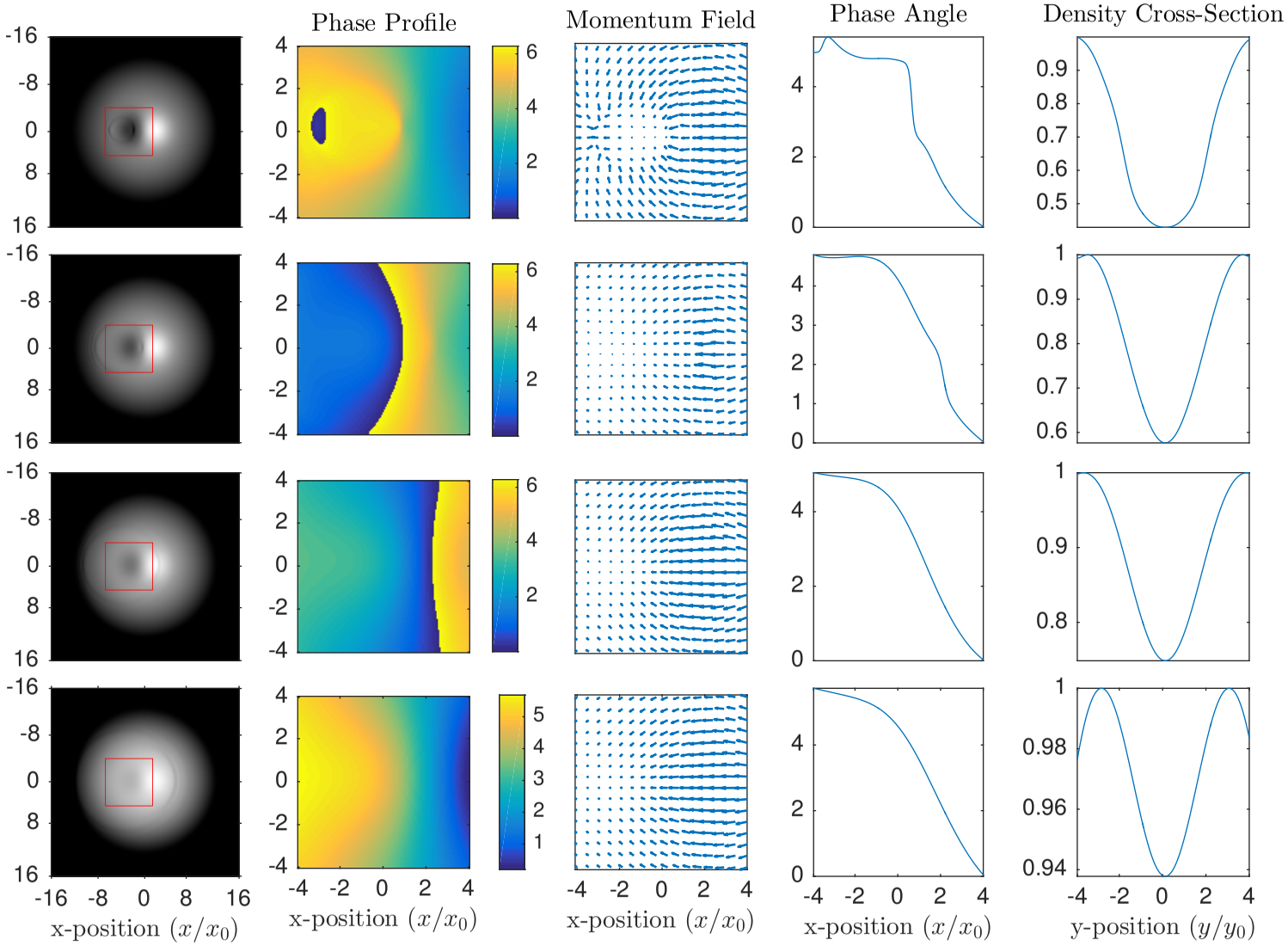

Figure 4.16: Under powered Vortex Imprinting Case: time steps 13-16. First Row: $t = 0.80T$. Second Row: $t = 0.85T$. Third Row: $t = 0.90T$. Fourth Row: $t = 0.95T$. Lengths are scaled by the natural oscillator length. Column 1: density profile. Red coloring encircles the insets described in columns 2-5. Column 2: phase profile - area corresponds to red square in column 1. Column 3: momentum vector field - area corresponds to red square in column 1. Column 4: phase cross-section corresponding to x-path through center of red square in column 1. Column 5: density cross-section corresponding to y-path through center of red square in column 1.

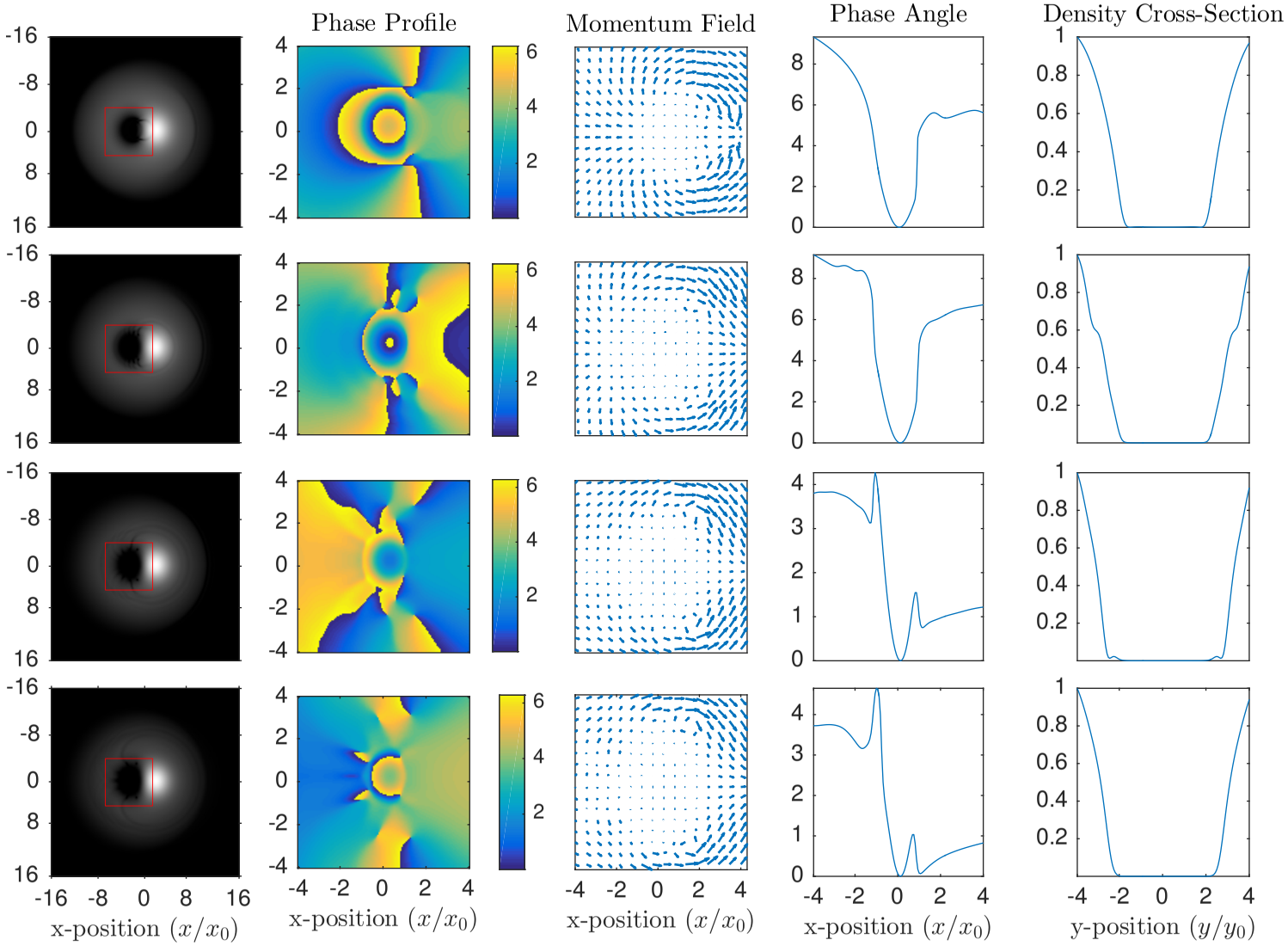

Figure 4.17: Over powered Vortex Imprinting Case: time steps 1-4. First Row: $t = 0.20T$. Second Row: $t = 0.25T$. Third Row: $t = 0.30T$. Fourth Row: $t = 0.35T$. Lengths are scaled by the natural oscillator length. Column 1: density profile. Red coloring encircles the insets described in columns 2-5. Column 2: phase profile - area corresponds to red square in column 1. Column 3: momentum vector field - area corresponds to red square in column 1. Column 4: phase cross-section corresponding to x-path through center of red square in column 1. Column 5: density cross-section corresponding to y-path through center of red square in column 1.

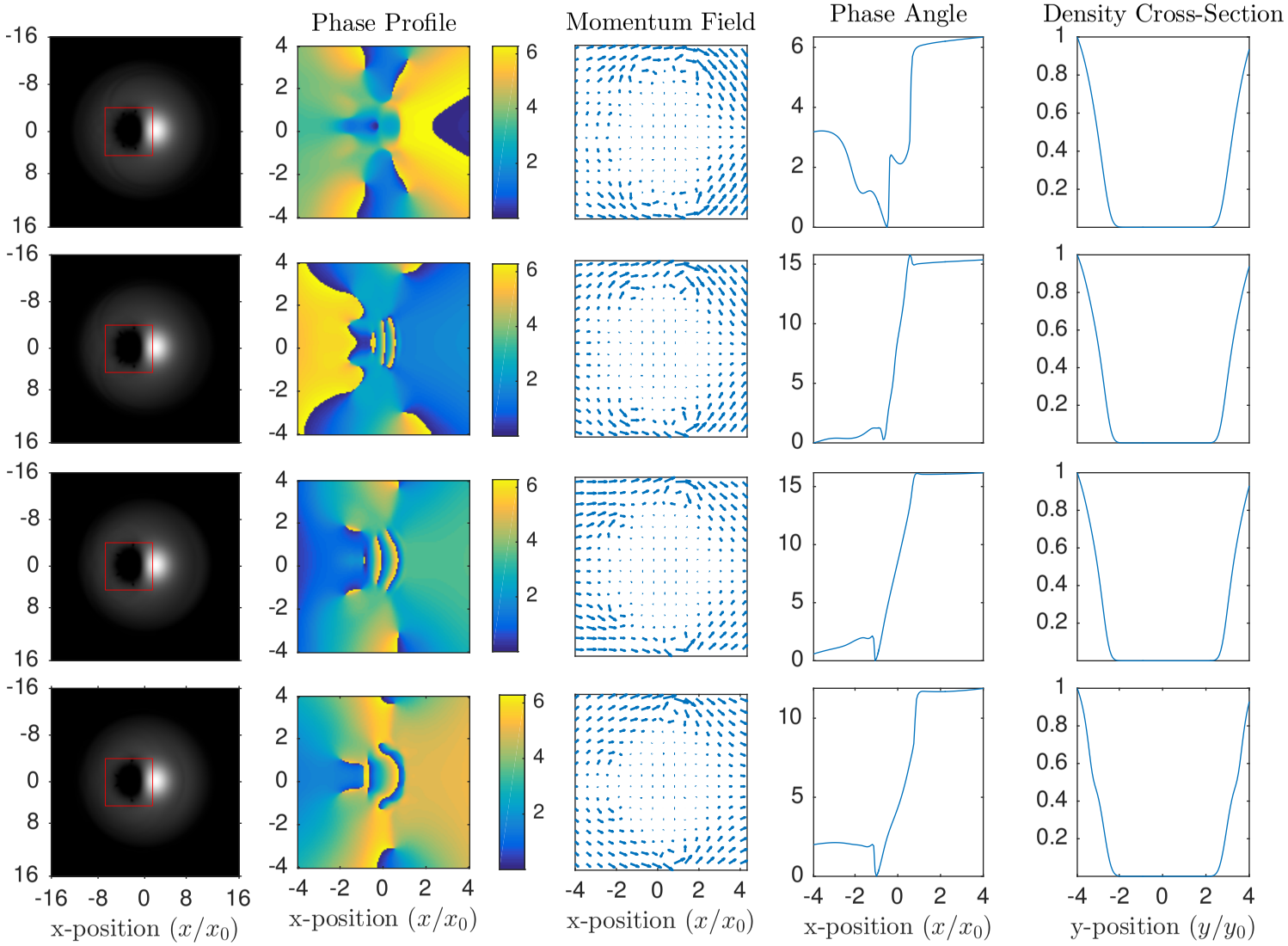

Figure 4.18: Over powered Vortex Imprinting Case: time steps 5-8. First Row: $t = 0.40T$. Second Row: $t = 0.45T$. Third Row: $t = 0.50T$. Fourth Row: $t = 0.55T$. Lengths are scaled by the natural oscillator length. Column 1: density profile. Red coloring encircles the insets described in columns 2-5. Column 2: phase profile - area corresponds to red square in column 1. Column 3: momentum vector field - area corresponds to red square in column 1. Column 4: phase cross-section corresponding to x-path through center of red square in column 1. Column 5: density cross-section corresponding to y-path through center of red square in column 1.

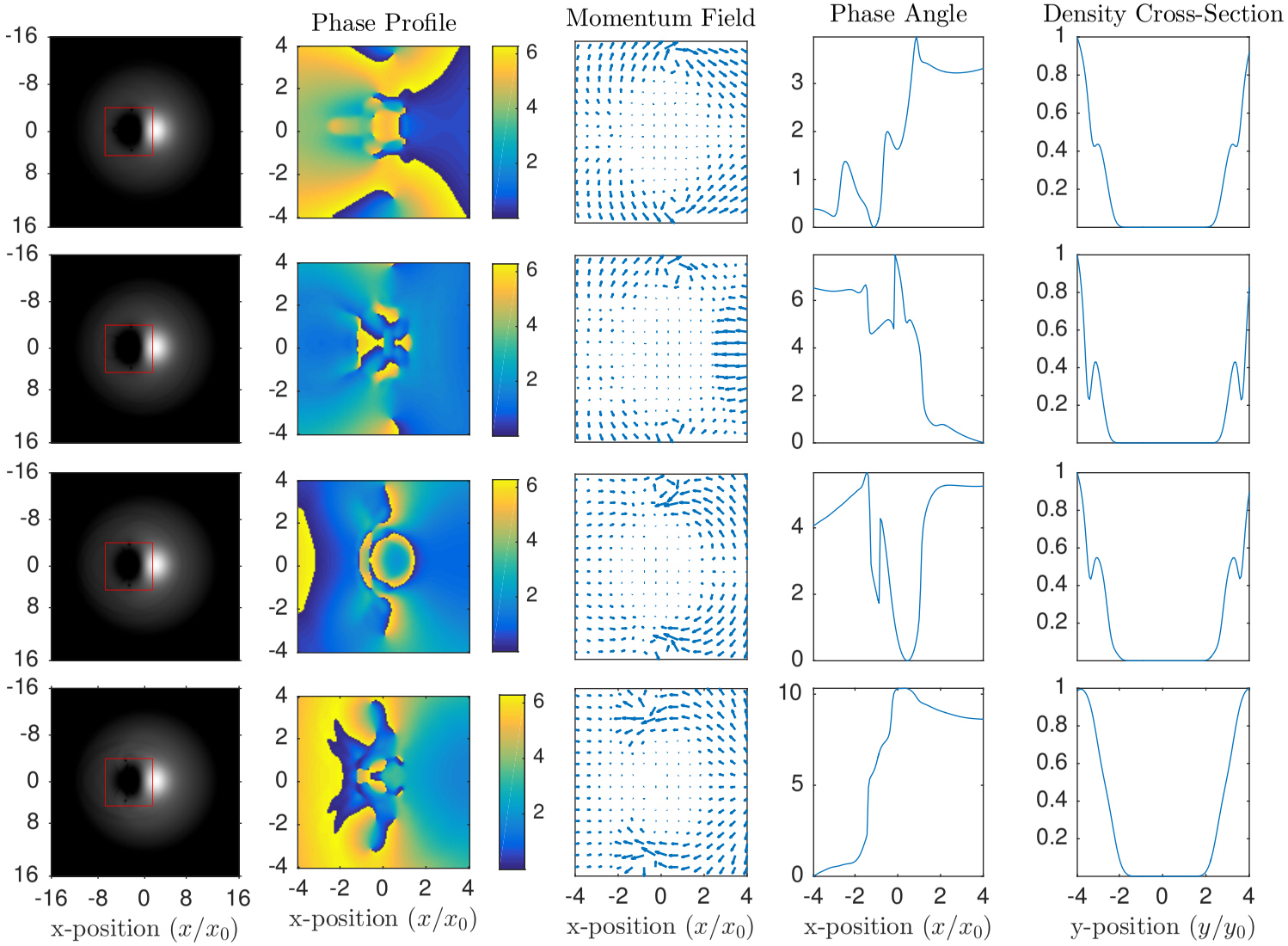

Figure 4.19: Over powered Vortex Imprinting Case: time steps 9-12. First Row: $t = 0.60T$. Second Row: $t = 0.65T$. Third Row: $t = 0.70T$. Fourth Row: $t = 0.75T$. Lengths are scaled by the natural oscillator length. Column 1: density profile. Red coloring encircles the insets described in columns 2-5. Column 2: phase profile - area corresponds to red square in column 1. Column 3: momentum vector field - area corresponds to red square in column 1. Column 4: phase cross-section corresponding to x-path through center of red square in column 1. Column 5: density cross-section corresponding to y-path through center of red square in column 1.

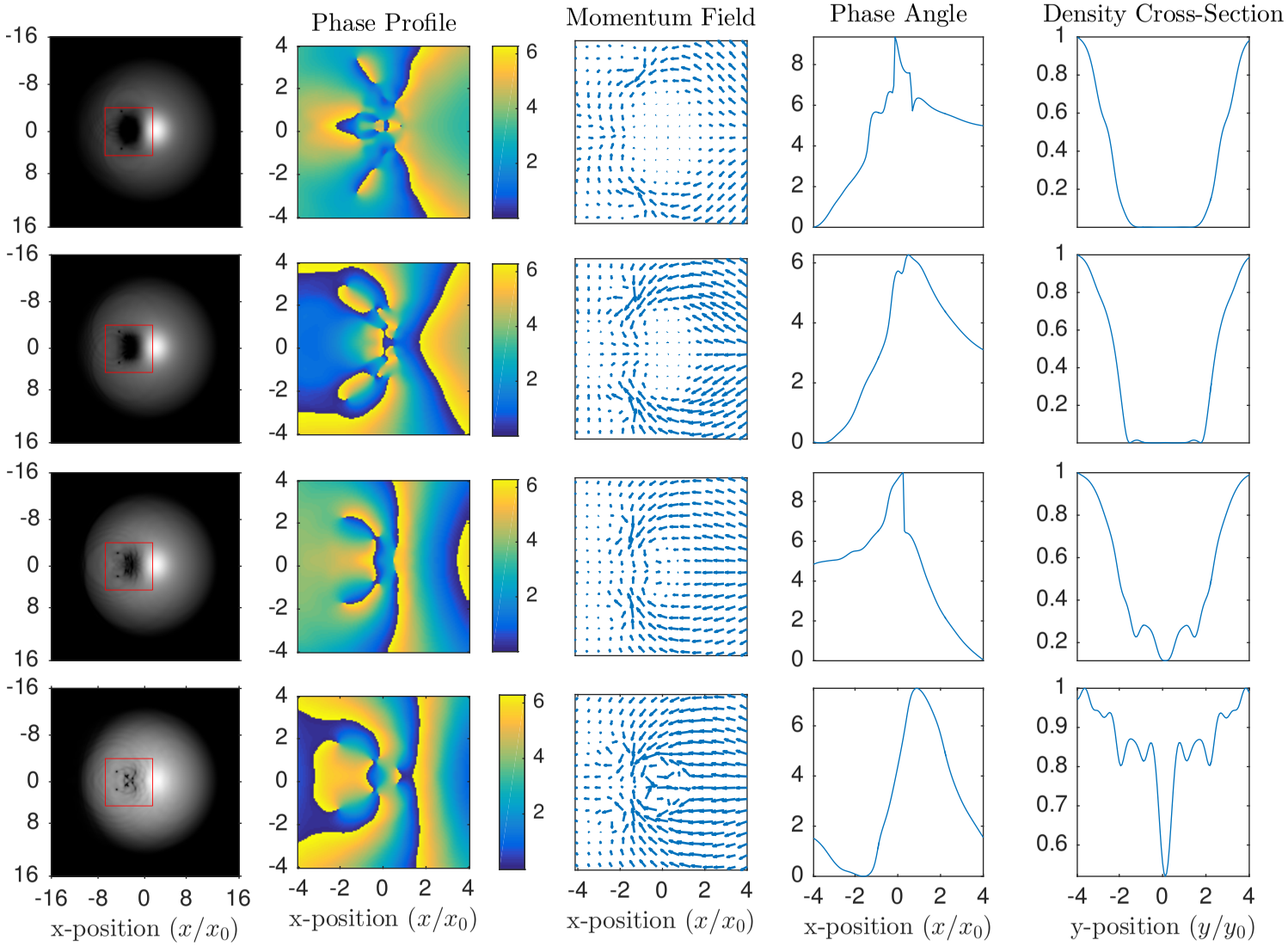

Figure 4.20: Over powered Vortex Imprinting Case: time steps 13-16. First Row: $t = 0.80T$. Second Row: $t = 0.85T$. Third Row: $t = 0.90T$. Fourth Row: $t = 0.95T$. Lengths are scaled by the natural oscillator length. Column 1: density profile. Red coloring encircles the insets described in columns 2-5. Column 2: phase profile - area corresponds to red square in column 1. Column 3: momentum vector field - area corresponds to red square in column 1. Column 4: phase cross-section corresponding to x-path through center of red square in column 1. Column 5: density cross-section corresponding to y-path through center of red square in column 1.

4.6 Single repulsive beam: experimental results

In the previous sections, a numerical study was investigated for a hybrid attractive-repulsive stationary barrier. Prior to beginning this numerical study, a preliminary experimental investigation was done using a stationary repulsive barrier with a time varying amplitude. The study was carried out similarly to the method described above, with the primary difference being that there is only a repulsive barrier and it is centrally located. This method was briefly investigated several years ago in our lab and is currently being revisited to investigate the physical phenomenon observed earlier [88].

This method, unlike the hybrid perturbation, is not observed in numerical GPE simulations to generate a vortex dipole. Furthermore, the physical reasons as to why this method readily generates vortex dipoles it not yet well understood. It is thought that it could be related to trap noise, decoherence, and the thermal atomic background [88]. As it stands, the experimental results described in this section represent a deviation between GPE analysis and the fundamental physics observed in the experiment.

The repulsive blue detuned barrier is ramped sinusoidally on and off once. The e^{-2} beam radius is approximately 15 μm in this study. The beam is always located centrally down the axis of the BEC.

The study is conducted by ramping the beam on and off over a perturbation time Δt. Various peak amplitudes are chosen and the number of resulting vortex cores are counted. The reason for counting vortex cores rather than vortex dipoles is that the circulation of individual cores is not known upon inspection; only their locations. This is repeated for various aspect ratio oblate BECs ranging in aspect ratios from 3 to 7.5, but in all cases the radial Thomas-Fermi radius is about 40 μm.

Figure 4.21 depicts the experimental results for a perturbation of 21 ms, which represents a perturbation time that is approximately $1/6$ of the radial trapping period. Of interest in this case is that for all trapping geometries, there appears to exist an optimal perturbation amplitude for the creation of vortex cores that is approximately $2\mu/3$. Perturbations either above or below this amplitude generate fewer vortex cores regardless of BEC aspect ratio.

Figure 4.22 depicts the experimental results for a perturbation of 62.5 ms, which represents a perturbation that is approximately $1/2$ of the radial trapping period. Unlike the case for very short perturbations, in this scenario the average number of quantized vortices nucleated scales linearly with the perturbation amplitude. For higher aspect ratio BECs, the rate of vortex core nucleation is higher, suggesting that higher aspect ratio BECs are more sensitive to this type of perturbation.

Figure 4.23 depicts the experimental results for a perturbation of 125 ms, which represents a perturbation that is approximately one full period of the radial trapping geometry. Similar to the 62.5 ms perturbation, the average number of quantized vortices nucleated scales linearly with the

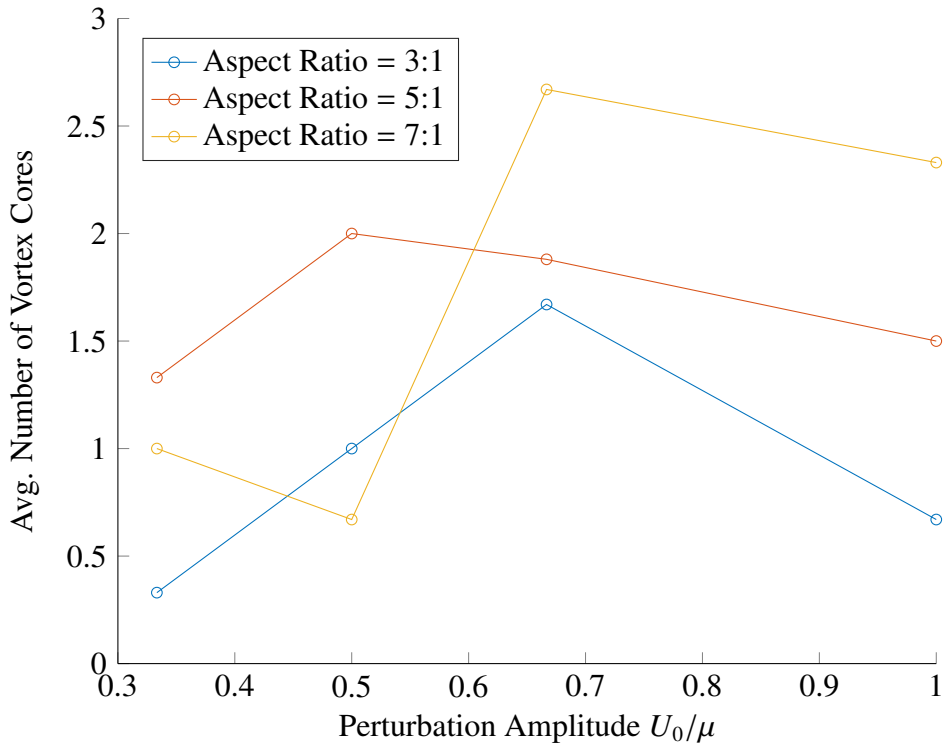

Figure 4.21: Average number of vortex cores observed after a 21 ms perturbation plotted against perturbation amplitude for various aspect ratio BECs.

perturbation amplitude. However, unlike the case for the 62.5 ms perturbation, the dependence in this case on BEC aspect ratio is less pronounced. Additionally, the overall number of vortices nucleated is approximately double that it was for the 62.5 ms perturbation.

This method of using a purely repulsive stationary time-dependent barrier to nucleate vortex dipoles proves to be highly repeatable. There is surely interesting underlying physics behind this mechanism that deserves a thorough experimental and theoretical investigation. The results are not seen in damped GPE numerical simulations and therefore likely due to mechanisms that are not modeled by the damped GPE. Examples of mechanisms not accounted for in the DGPE include finite temperature dynamics and the existence of multiple degenerate modes. Numerical simulations more robust than the DGPE can and are done by research groups dedicated to numerical and theoretical analysis and use for example the Stochastic Projected GPE (SPGPE) [89,90]. Specifically, the Kelvin-Helmholtz instability [91, 92] is one candidate mechanism for vortex dipole nucleation; Kelvin-Helmholtz instability classically predicts a transition to turbulent flow at the interface of two fluids of different densities with a relative velocity. In the case of a quantum superfluid, this could correspond to the counterflow between the degenerate BEC ground state and the thermal reservoir; that is, the non-BEC atoms that account for the finite tempera-

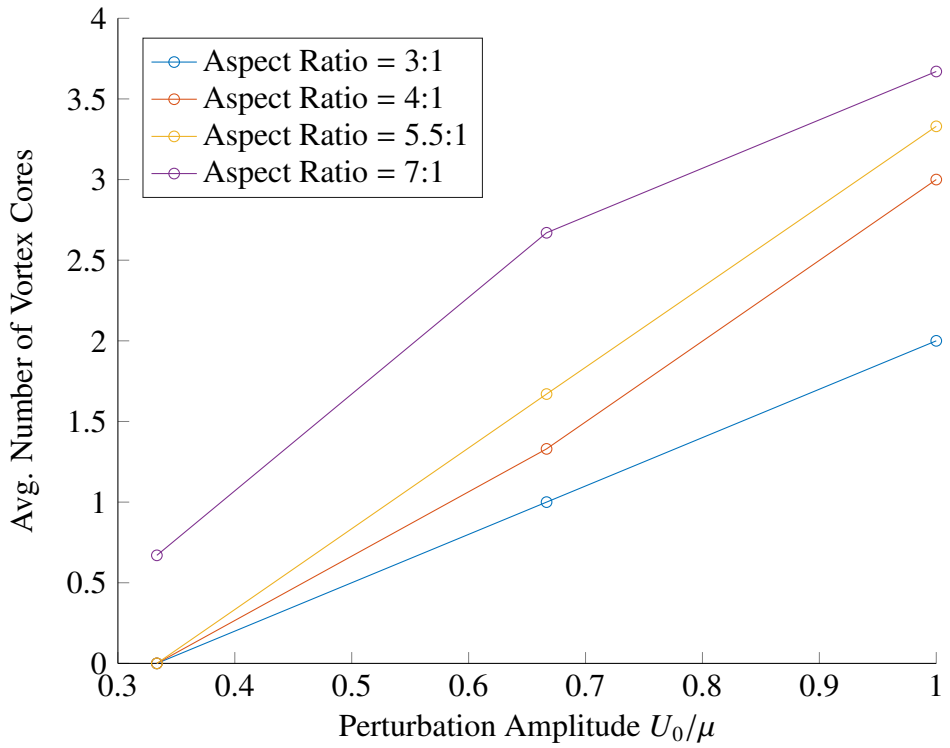

Figure 4.22: Average number of vortex cores observed after a 62.5 ms perturbation plotted against perturbation amplitude for various aspect ratio BECs. A 62.5 ms perturbation represents a half period of the radial harmonic oscillator

ture of the system. It is possible, though uncertain at this point, that SPGPE simulations of this perturbation could corroborate this observation of vortex dipole nucleation.

While this method serves as an interesting physical phenomenon to study, it is will not be a useful technique for architecting an arbitrary waveform until it is more fully understood, thus motivating the hybrid red-blue vortex-imprinting mechanism investigated numerically in this chapter.

4.7 Concluding remarks

To summarize the study, a method was explored numerically for nucleating vortex dipoles. An area in parameter space specifically with respect to beam size, beam separation, beam power, and perturbation time was mapped out. Within the parameter space, a critical regime for vortex dipole nucleation was identified. Outside of the critical regime either vortex dipoles are not nucleated or unwanted excitations in addition to vortex dipoles are nucleated. An optimal area in parameter space is identified where parameter drift would be least likely to drift into a less

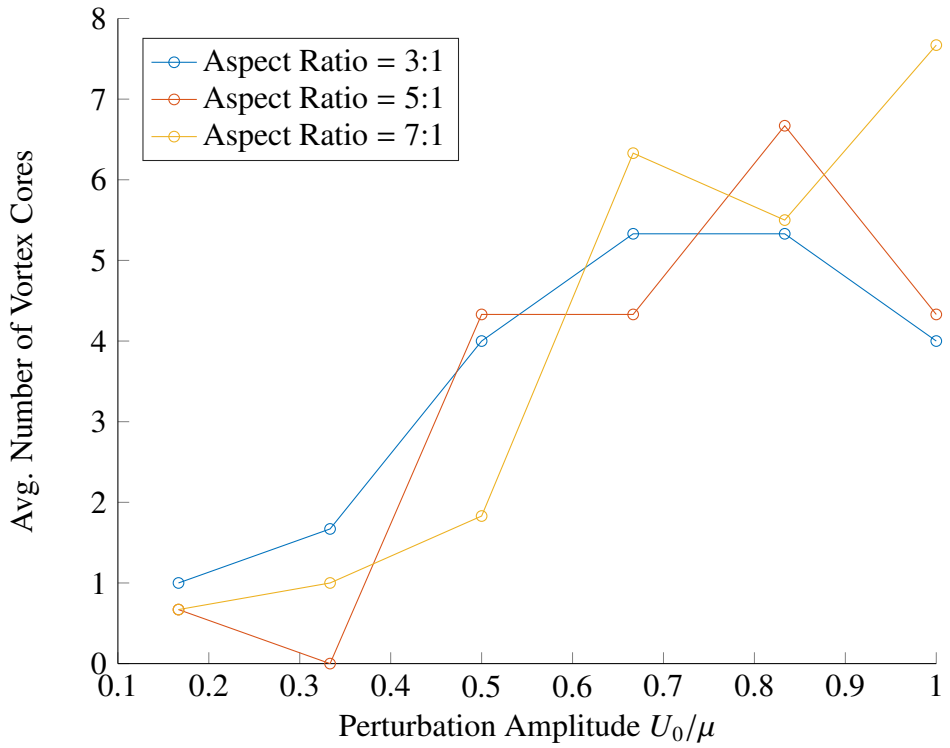

Figure 4.23: Average number of vortex cores observed after a 125 ms perturbation plotted against perturbation amplitude for various aspect ratio BECs. A 125 ms perturbation represents a full period of the radial harmonic oscillator

favorable zone. Lastly, an experimental apparatus is prototyped for executing this experimentally. Experimental parameters for the University of Arizona BEC lab are identified and proposed based on the numerical investigation.

As was mentioned in the beginning of this chapter, several methods already exist for creating vortices or vortex dipoles in a BEC. The key advantage of this method is that it imprints a vortex dipole locally to the perturbation; thus, the perturbation does not need to modify the bulk BEC dynamics as is the case for swiping a repulsive perturbation through the BEC. This new method will be useful for architecting arbitrary vortex distributions in a BEC. A simpler method for introducing a vortex dipole will simplify basic studies of fundamental turbulence such as vortex-antivortex annihilation, which is one of the most basic vortex studies and is not well understood phenomenologically. A simple method for repeatedly generating the same system's initial conditions will make the study of these questions simpler, particularly when used in conjunction with recent abilities developed for the *in situ* detection of vortices in Bose-Einstein condensates discussed earlier in this dissertation.

The device that was discussed and prototyped will also enable additional experiments in the

field of turbulence and vortex physics. In particular, a time-modulated repulsive barrier is known to nucleate vortex dipoles in highly oblate BECs. This system can be used — and was used briefly — to investigate the physics of this vortex dipole nucleation method. The introduction of a steerable red-detuned beam will enable the investigation into whether a time-modulated stationary red-detuned beam will also nucleate vortex dipoles. The red-detuned beam itself can be used to replicate a wide range of previous experiments that used a repulsive barrier to nucleate vortex dipoles, but, instead use an attractive perturbation. For example, does an attractive potential moving through a BEC nucleate vortex dipoles as effectively as a repulsive barrier [14]? Does spiraling a red-detuned beam towards the center of the BEC also nucleate vortices of same-sign [81]? With the combination many steerable repulsive and attractive perturbations, could an arbitrary wave function be architected? An upcoming project in the BEC lab will use a digital micromirror device to generate many attractive and repulsive steerable beams across the extent of the BEC. The study described in this chapter serves as one step towards the long sought after goal of architecting arbitrary waveforms for the sake of studying two-dimensional quantum turbulence.

CHAPTER 5

Second harmonic generation with perfect and imperfect optical vortices

5.1 Introduction

The phenomenon of second harmonic generation has been previously demonstrated to convert two collinear photons of the same orbital angular momenta (OAM), ℓ, and energy $\hbar\omega$ to a single photon with twice the energy $2\hbar\omega$ and twice the OAM 2ℓ in agreement with both conservation of energy and conservation of OAM [93]. It has been further demonstrated both theoretically and experimentally that for two non-collinear input OAM beams interacting at an angle 2θ in a non-linear medium, a second harmonic beam is generated with a reduced conversion efficiency [94, 95]. In this chapter, I expand on this idea to demonstrate theoretically that not only does a nonzero tilt angle reduce the conversion efficiency of the output OAM beam, but that the output second harmonic beam will consist of a spectrum of OAM and the most probable output OAM is not necessarily intuitive.

In my analysis I consider a configuration similar to that reference [94] case (i): two input beams at frequency ω and interacting in a non-linear medium with an interaction angle θ illustrated in figure 5.1. The first input beam is taken to be a Laguerre-Gaussian beam with no azimuthal phase factor and therefore no OAM. The second input beam I consider is a thin ring shaped beam, termed a perfect optical vortex, which is distinct from a Laguerre-Gaussian beam but was chosen because it is experimentally more interesting, was used in the previous study on which I expand, and is easy to generate [94–96]. The optical OAM beams described in this work are experimentally achievable by use of spatial phase modulators, which directly imprint a phase winding on the beam [97]. The ring beam has integer OAM $\ell \neq 0$. Generating ring beams with

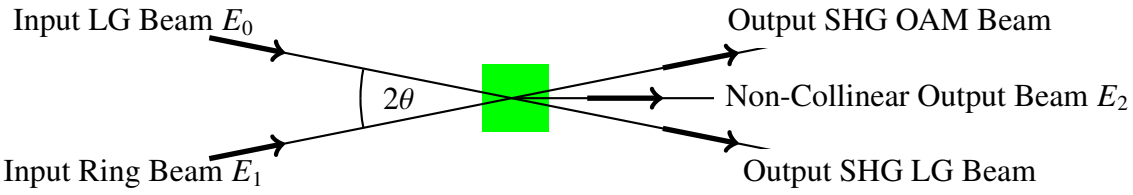

Figure 5.1: The diagram shows an example of how the system is configured. There are two input beams: a Laguerre-Gaussian beam with $\ell = 0$ and a Ring beam with a chosen orbital angular momentum ℓ. There are three output beams resulting from SHG processes, but it is only the non-collinear output beam E_2 that is of interest in this study.

OAM as high as 40 should be experimentally feasible. For the sake of these simulations, type I SHG in a uniaxial crystal, BBO, is assumed. The input waves are ordinary waves and the second harmonic beam is an extraordinary wave. For simplicity, I make the undepleted pump beam and paraxial approximations.

Extremizing the ring size, orbital angular momentum, and interaction angle all come at a cost. As the ring size is decreased, experimental observations become increasingly difficult and diffraction effects become more significant in propagation. Increasing the orbital angular momentum to $\ell \gg 40$ could poses experimental challenges due to the discrete spatial resolution of the spatial light modulator, for example. Increasing the interaction angle reduces the accuracy of propagation approximations.

5.2 Background and analytic theory

An introduction to second harmonic generation is discussed in reference [98], from which I base my analysis. For the scenario described here, an input electric field in a nonlinear medium consists of two fundamental pump fields E_0 and E_1. Additionally, one non-collinear second harmonic field of interest, denoted E_2, is considered. The net fundamental field in the slowly varying envelope approximation can be written as

$$\tilde{E}(\mathbf{r}, t) = \tilde{E}_0(\mathbf{r}, t) + \tilde{E}_1(\mathbf{r}, t), \tag{5.1}$$

where the tildes indicate that the rapidly varying field is being considered. From here forward, the slowly varying amplitudes corresponding to each field are denoted without a tilde. Each of the slowly varying fundamental fields amplitudes E_0 and E_1 in addition to the second harmonic field E_2 can be represented as

$$E_j(\mathbf{r}) = E_j(\mathbf{r})e^{-ik_j z}, \tag{5.2}$$

where k_j represents the ordinary or extraordinary wave number corresponding to the respective field. The slowly varying envelopes of the fundamental components then propagate according to

$$\frac{\partial E_j}{\partial z} = \frac{i}{2k_o}\nabla_\perp^2 E_j \qquad j = 0, 1, \tag{5.3}$$

where k_o represents the wave number for ordinary fields propagating in the crystal.

The second harmonic beam, E_2, is an extraordinary field driven by two source fields (E_0 and E_1) and the corresponding driven wave equation is given by:

$$\frac{\partial E_2}{\partial z} = \frac{i}{2k_e}\nabla_\perp^2 E_2 + i\eta E_0(\mathbf{r})E_1(\mathbf{r})e^{i\Delta k(0)z} \tag{5.4}$$

where k_e represents the extraordinary second harmonic wave number, $\eta = 32\pi d_{\text{eff}}\omega^2/k_e c^2$, d_{eff} is the nonlinear constant, and $\Delta k(0) = (2k_o - k_e)$ is the plane wave vector mismatch projected onto the z-axis. One input beam is taken to be a ring beam with orbital angular momentum ℓ propagating at angle θ with radius R and width W, and the second beam is taken to be a first order gaussian beam propagating at angle $-\theta$. The respective electric fields are given by

$$E_0(\mathbf{r}) = A_\ell(\rho)e^{i\left(k_o - \frac{1}{2k_o}\frac{\ell^2}{R^2}\cos\phi\right)z}e^{i\ell\phi}e^{-ik_o\theta x} \tag{5.5}$$

and

$$E_1(\mathbf{r}) = A_G(\rho)e^{ik_o z}e^{+ik_o\theta x}, \tag{5.6}$$

where ρ represents the radial distance from the optical axis, ϕ represents the azimuthal angle about the optical axis, A_ℓ represents the slowly varying envelope amplitude of the ring beam, A_G represents the slowly varying envelope amplitude of the Laguerre-Gaussian beam, and R represents the radius of the ring beam. The superposition of the two fields contains several terms, one of which serves as the non-collinear source term for the output beam of interest. The other terms act as sources for the output OAM and output LG beams shown in figure 5.1.

The non-collinear output beam of interest is sourced by the product of the two beams:

$$E_0(\mathbf{r})E_1(\mathbf{r}) = A_G(\rho)A_\ell(\rho)\exp\left[i\ell\phi - \frac{iz}{2k_o}\frac{\ell^2}{R^2} + \frac{iz\ell\theta}{R}\cos\phi\right]. \tag{5.7}$$

This result is decomposed into the quantized angular momenta components by the Jacobi-Anger expansion,

$$E_0(\mathbf{r})E_1(\mathbf{r}) = A_G(\rho)A_\ell(\rho)\sum_{n=-\infty}^{\infty} i^n \exp\left[i(\ell+n)\phi - \frac{iz}{2k_o}\frac{\ell^2}{R^2}\right]J_n\left(\frac{z\ell\theta}{R}\right), \tag{5.8}$$

where J_n represents the nth bessel function of the first kind. The generated second harmonic evolves according to

$$\frac{\partial E_2}{\partial z} = \frac{i}{2k_e}\nabla_\perp^2 E_2 + i\eta E_0(\mathbf{r})E_1(\mathbf{r})e^{i\Delta k(0)z}, \tag{5.9}$$

where the far right source term is the product of the ring and Laguerre-Gaussian input beams. By substituting the Jacobi-Anger expression, this is written as:

$$\frac{\partial E_2}{\partial z} = \frac{i}{2k_e}\nabla_\perp^2 E_2 + i\eta A_G(\rho)A_\ell(\rho)\sum_{n=-\infty}^{\infty} i^n \exp\left[i(\ell+n)\phi - \frac{iz}{2k_o}\frac{\ell^2}{R^2}\right]J_n\left(\frac{z\ell\theta}{R}\right)e^{i\Delta k(0)z}. \tag{5.10}$$

We make the following change in variables: $E_2(\mathbf{r}) = \mathcal{E}_2(\rho, z)e^{i\ell\phi}$. The propagation equation can then be written in the form:

$$\frac{\partial \mathcal{E}_2}{\partial z} = \frac{i}{2k_e}\left(\underbrace{\frac{\partial^2}{\partial\rho^2} + \frac{1}{\rho}\frac{\partial}{\partial\rho}}_{\text{Terms negligible}} - \frac{\ell^2}{\rho^2}\right)\mathcal{E}_2 + i\eta A_G(\rho)A_\ell(\rho)\sum_{n=-\infty}^{\infty} i^n \exp\left[in\phi - \frac{iz}{2k_o}\frac{\ell^2}{R^2}\right] J_n\left(\frac{z\ell\theta}{R}\right)e^{i\Delta k(0)z}, \tag{5.11}$$

where the two radial derivative terms are negligible in the case of a thick ring OAM beam with radius $R \gg \lambda$. The medium is much thinner than the Rayleigh range of the propagating fields. If we assume the thickness of the ring beam and to be $W = R/10$, for example, where $R = 500\mu m$ is the ring radius, then the Rayleigh range can be approximated as

$$z_R = \frac{\pi w_0^2}{\lambda} \approx \frac{\pi W^2}{\lambda} \gg L, \tag{5.12}$$

where $L = 500\mu m$ is the length of the crystal. The importance of the Rayleigh range being much larger than the interaction length is so that diffraction effects have negligible influence on the nonlinear interaction in the analytical model.

The form is simplified by assuming the intensity of field to be constant radially across the width of the ring, and then evaluating the SHG at the peak of the ring $\rho = R$,

$$\frac{\partial \mathcal{E}_2}{\partial z} = -\frac{i}{2k_e}\frac{\ell^2}{R^2}\mathcal{E}_2 + i\eta A_G(R)A_\ell(R)\sum_{n=-\infty}^{\infty} i^n \exp\left[in\phi - \frac{iz}{2k_o}\frac{\ell^2}{R^2}\right] J_n\left(\frac{z\ell\theta}{R}\right)e^{i\Delta k(0)z}. \tag{5.13}$$

We make the change of variables $\mathcal{E}_2(\rho = R, z) = A_2(z)e^{-\frac{iz}{2k_e}\frac{\ell^2}{R^2}}$ to express the the form in terms of the slowly varying envelopes:

$$\frac{\partial A_2(z)}{\partial z} = i\eta A_\ell(R)A_G(R)\sum_{n=-\infty}^{\infty} i^n \exp[in\phi]\exp\left[i\Delta k(0)z + \left(\frac{1}{k_e} - \frac{1}{k_o}\right)\frac{i\ell^2 z}{2R^2}\right] J_n\left(\frac{z\ell\theta}{R}\right). \tag{5.14}$$

By defining the k-vector mismatch,

$$\Delta k(\ell) = \Delta k(0) + \frac{1}{2}\left(\frac{1}{k_e} - \frac{1}{k_o}\right)\frac{\ell^2}{R^2}, \tag{5.15}$$

the propagation equation can be expressed as

$$\frac{\partial A_2(z)}{\partial z} = i\eta A_\ell(R)A_G(R)\sum_{n=-\infty}^{\infty} i^n \exp[in\phi]\exp\left[i\Delta k(\ell)z\right] J_n\left(\frac{z\ell\theta}{R}\right). \tag{5.16}$$

Examination of equation 5.16 shows that $A_2(z)$ consists of terms with a spectrum of quantized orbital angular momentum and so the second harmonic field can be written as a superposition of mutually orthogonal OAM terms

$$E_2(\mathbf{r}) = \sum_{n=-\infty}^{\infty} A_2^{(n)}(z) e^{i(n+\ell)\phi} e^{-\frac{iz}{2k_e}\frac{(\ell+n)^2}{R^2}}. \tag{5.17}$$

The angular momenta components propagate according to the differential equation:

$$\frac{dA_2^{(n)}}{dz} = i^{n+1}\eta A_G A_\ell e^{i\Delta k(n,\ell)} J_n\left(\frac{z\ell\theta}{R}\right) \tag{5.18}$$

with boundary condition: $A_2^{(n)}(0) = 0$. Each of the individual angular momenta components can then be computed individually by numerical integration as

$$A_2^{(n)} = i^{n+1}\eta A_G A_\ell \int_0^L \mathrm{d}z\, e^{i\Delta k(n,\ell)} J_n\left(\frac{z\ell\theta}{R}\right), \tag{5.19}$$

which serves as the basis for this chapter.

Previous work in reference [94] investigated both theoretically and experimentally the case of very small angles where all terms other than $n = 0$ could be ignored. The driven equation for the second harmonic in this special case is

$$\frac{dA_2}{dz} = i\eta A_0(R) A_\ell(R) e^{-\frac{iz}{4k_o}\frac{\ell^2}{R}} J_0\left(\frac{z\ell\theta}{R}\right), \tag{5.20}$$

which can be evaluated in two different regimes. The second harmonic power $P_2(\ell)$, can be evaluated at the peak of the ring as $P_2(\ell) = 2\pi RW|E_2(R,z)|^2$ for the limit in which the exponential term is assumed to dominate ($\theta \to 0$) and that in which the Bessel term dominates. Their respective forms vary as

$$P_2(\ell) \propto \mathrm{sinc}^2\left(\frac{\ell^2}{16\pi}\frac{\lambda_1 L}{n_o R^2}\right) \tag{5.21}$$

and

$$P_2(\ell) \propto \left(1 - \frac{\ell^2}{\ell_c^2}\right). \tag{5.22}$$

Both of these regimes have been observed experimentally [94].

I build upon this work by numerically investigating the output power spectrum of orbital angular momenta, $P_2^{(n)} = |A_2^{(n)}|^2$, for the more general case where the nonzero terms cannot all be ignored. In particular, I seek a regime in which neither equation 5.21 nor equation 5.22 adequately represents the output fields.

5.3 Analysis

The results of the previous section indicate that there is a spread of quantized angular momenta in the output beam. The average angular momentum output turns out to be equal to the input orbital angular momentum, $\langle \ell \rangle = \ell_{\text{in}}$. The idea of an OAM output spectrum, however, is a very interesting possibility because it suggests that the OAM is statistically conserved but not necessarily conserved on a photon by photon basis.

I numerically evaluate the output parameter A_2^n, for a given experimental setup to find the output angular momentum spectrum for a given interaction length L, beam radius R, input angle θ, and input angular momentum ℓ.

The experimental setup of reference [94] uses a BBO crystal of length $L = 500\mu m$, with an input angle θ on the order of several degrees, a beam radius of $R = 500\mu m$, and input angular momenta ranging from 1 - 20. In order to relate my study to what can readily be tested, I restrict my search to parameters close to this regime. In my computations I assume a crystal length $L = 500\mu m$, an interaction angle of 10 degrees, and a beam radius of $250\mu m$. I investigate input angular momenta ranging from $\ell = 0$ to $\ell = 40$. These parameters are only slightly more extreme than those of the original theoretical study and experiment, however this deviation revealed a different operating regime when analyzed numerically.

First, I examine the case with a half angle of 5 degrees (full angle 10°) with ring radius 500 microns and input angular momentum $\ell = 10$, the resulting orbital angular momentum spectrum is shown in figure 5.3-a. The findings of this example case are not an extreme case: the input beam angular momentum is $\ell = 10$. It is interesting that there appears to be a spread in angular momenta: about 4.5% of the output power in each of the $\ell = 9$ and $\ell = 11$ modes. This suggests that the angular momentum of a second harmonic photon can increase or decrease relative to the input orbital angular momenta.

I next consider the case where the input orbital angular momentum is $\ell = 20$, all other parameters remain the same. See figure 5.3-c. This case demonstrates an unremarkable but possibly expected change from the $\ell = 10$ case. The output peak is now centered at orbital angular momentum 20 and the spectrum has broadened slightly. There is clearly a finite, but small, amount of power at $\ell + n = 22, 18$. This plot depicts approximately the most extreme case of the experimental study.

I next examine the effect of reducing the ring radius by a factor of 2 to $R = 250\mu m$. I furthermore increase the interaction angle by a factor of 2 to 10 degrees and evaluate the output angular momentum spectrum for an input angular momentum of $\ell = 15$. The output angular momentum spectrum is seen in figure 5.4-b.

This case is now in the regime where more interesting features are revealed. The most obvious being the bimodal spectrum in orbital angular momenta. Note that for this case the input angular momentum is $\ell = 15$. Similarly, the average output angular momentum is $\ell + n = 15$. Curiously,

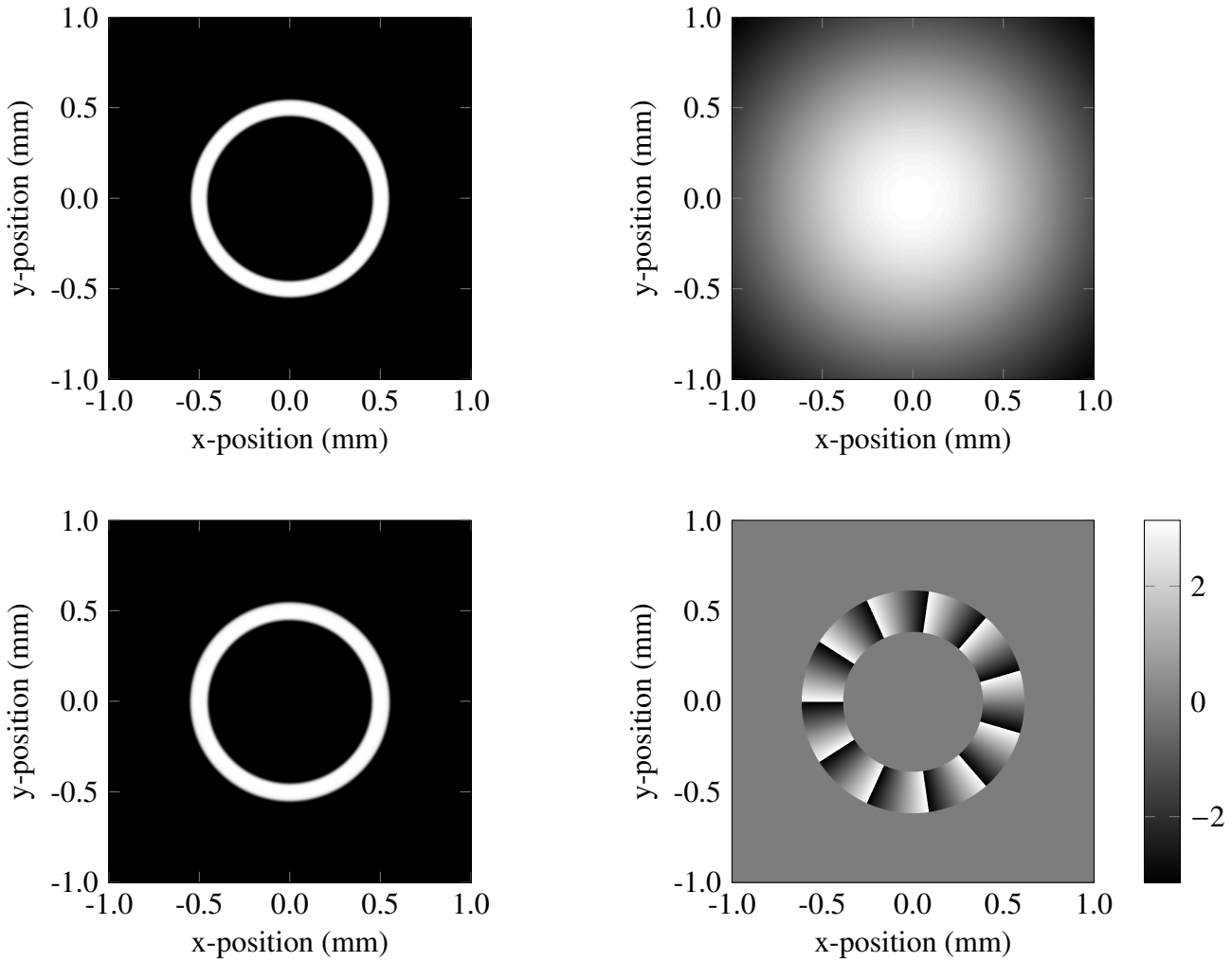

Figure 5.2: Top left is the intensity profile $|E_0|^2$ of a ring beam of radius $R = 500\mu m$ with $\ell = 15$. Top right is the intensity profile $|E_1|^2$ of a Laguerre-Gaussian beam. Bottom left is the intensity profile of the multiplicative field $|E_0E_1|^2$. Bottom right is the phase profile of the beam corresponding to the bottom left profile. The azimuthal nodes are due to the orbital angular momentum $\ell = 15$.

the most *probable* output angular momentum states are $\ell + n = 17$ and $\ell + n = 13$, each being approximately 4 times more likely than $\ell = \langle\ell\rangle = 15$.

This particular case was achieved by reducing the ring beam radius by a factor of two and doubling the interaction angle by a factor of two. The input angular momentum is still within the bounds of the original experimental apparatus. My investigation involved the three independent variables: input angular momentum, beam radius, and interaction angle. I have found that this interesting bimodal behavior may arise when modifying any one of these parameters: increasing

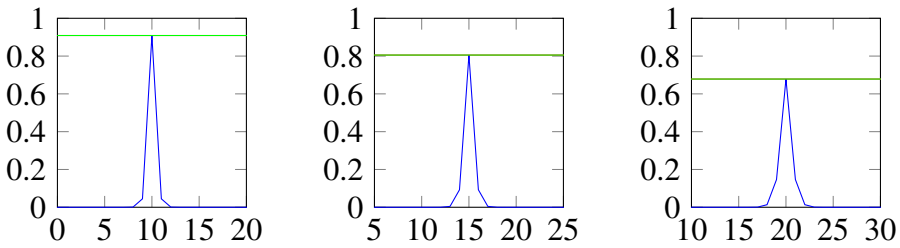

(a) $\ell = 10$ (b) $\ell = 15$ (c) $\ell = 20$

Figure 5.3: For a fixed ring beam radius ($R = 500\mu m$) and a fixed interaction angle $\theta = 5°$, the output orbital angular momentum power spectrum is shown for input angular momenta $\ell = 10$ (left), $\ell = 15$ (center), and $\ell = 20$ (right). For a fixed interaction angle and beam radius, as the input orbital angular momentum increases, the output orbital angular momentum power spectrum spreads out.

the input orbital angular momentum, increasing the interaction angle, or decreasing the ring radius. For the first example that I have shown, I adjust all three parameters in order to keep the overall configuration as close as possible to the current experimental setup in order to make the possibility of experimental testing most realistic.

By holding the beam radius at $R = 500\mu m$ and the interaction angle at $\theta = 5°$, a similar spectrum is achieved when the input orbital angular momentum is $\ell = 60$. It may be difficult to experimentally achieve repeatable beams with $\ell = 60$. See figure 5.4-b.

By holding the beam radius at $R = 500\mu m$ and the input orbital angular momentum at $\ell = 15$, again the result can be achieved by increasing the interaction angle to $\theta = 21°$. At such high interaction angles, the propagation approximations made may be less reliable. See figure 5.4-c.

Lastly, the result is achieved by holding the input angle constant at $\theta = 5°$ and the input orbital angular momentum at $\ell = 15$ while reducing the ring radius to $120\mu m$. At such small beam radii, diffraction effects may dominate and wash out the desired results. See figure 5.4-d.

There are three distinct ways to enter into this regime. Minor adjustments to each of these three experimental parameters make it possible to reach this regime while maintaining an overall parameter choice that should be experimentally achievable.

By further extremizing the parameters, the output OAM spectrum continues to broaden and the number of peaks oscillate. For example, for the parameters $R = 150\mu m$ and $\theta = 10°$, notable features exist when the input OAM is $\ell = 9, 14, 20, 26, 31$, and 37. See figure 5.5.

5.4 Beam propagation method

More could be learned about this phenomenon by a study via Beam Propagation Method. The feasibility of such a study was investigated and a realistic parameter set would require a pro-

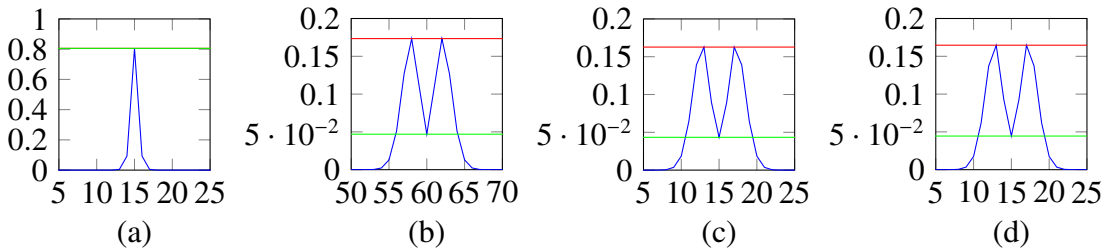

Figure 5.4: There are various ways to achieve the interesting bimodal spectrum. From the left, the first case (a) is that of $R = 500\mu m$, $\ell = 15$, and $\theta = 5°$. This is the nominal case – lacking of interesting features for the purposes of this paper. The second case (b) is that of $R = 500\mu m$, $\ell = 60$, and $\theta = 5°$. The third case (c) is that of $R = 500\mu m$, $\ell = 15$, and $\theta = 21°$. The final case (d) is that of $R = 120\mu m$, $\ell = 15$, and $\theta = 5°$.

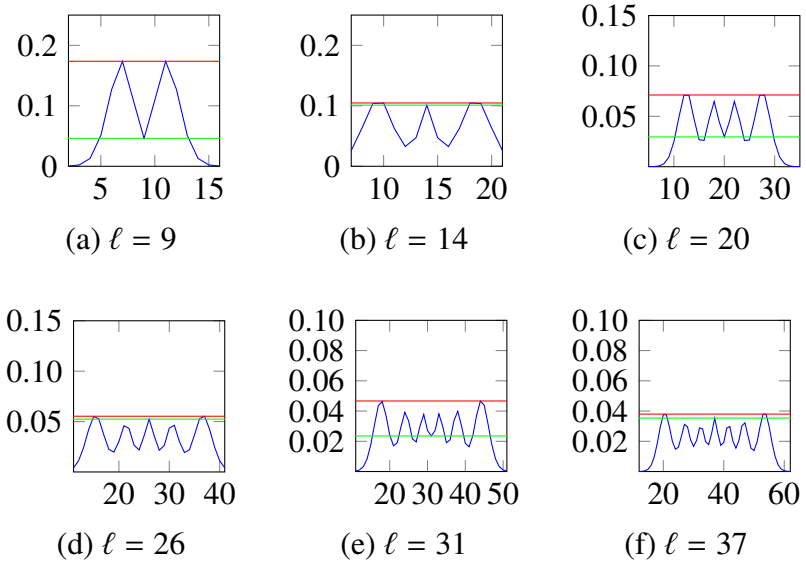

Figure 5.5: Top row from left to right: case of $\ell = 9$, $\ell = 14$, $\ell = 20$. Bottom row: cases of $\ell = 26$, $\ell = 31$, and $\ell = 37$. All cases were calculated with $R = 150\mu m$ and $\theta = 10°$.

hibitively large transverse resolution that cannot be computed with the resources available at the time of this study; however, it is possible to demonstrate the principle for a configuration outside of experimentally realizable parameters. A basic beam propagation was developed with parameters $\lambda_1 = 785nm$, $R = 120\mu m$, input angular momentum $\ell = 40$, and input angle $\theta = 10°$. Figure 5.6 shows the intensity profile of the SHG beam at the beginning of the crystal (a) and at the end of the crystal (b). In the latter image, the intensity profile has clearly developed an asymmetry. This is due to the interference of a range of orbital angular momentum states.

A next step in the beam propagation approach would be to develop an algorithm that decomposes the propagated fields into the constituent orbital angular momentum states in an attempt to

replicate plots similar to that of figures 5.3 and 5.4. This has not yet been done.

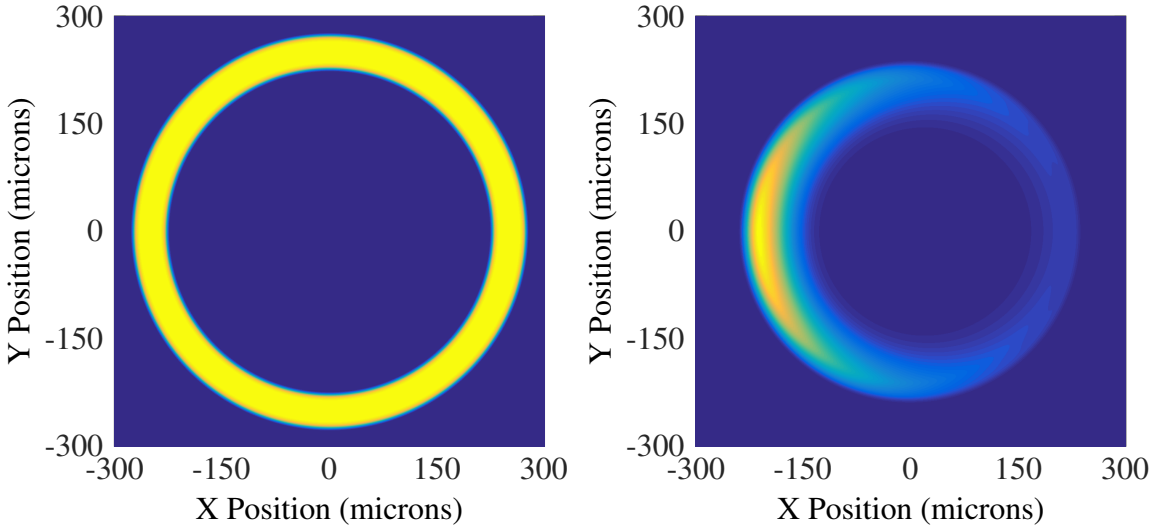

Figure 5.6: A basic beam propagation was developed with parameters $\lambda_1 = 785nm$, $R = 250\mu m$, input angular momentum $\ell = 1$, and input angle $\theta = 10°$. The left image shows the input beam profile. The field is the second harmonic beam generated by the product of the Laguerre-Gaussian beam and the Ring beam with $\ell = 40$. The right image shows the resulting beam after propagating with the source term through the crystal medium. The asymmetry is a result of interference between a the broad pectrum of OAM states.

5.5 Proposed experiment

The hypothesized output orbital angular momentum spread could be tested with an experimental setup similar to the existing one, which is shown in figure 5.7. Such an experimental setup would need to be modified to permit a smaller ring radius on the order of $250\mu m$ as well as accept larger input angles as large as 10 degrees. Additionally, a mechanism to separate out different orbital angular momentum states from the output beam is necessary in order to differentiate between the different OAM states and thus measure the OAM spectrum. The OAM content of an optical beam can be measured experimentally using a multipinhole plate [99–101], biprism beamsplitters [102], Mach-Zehnder interferometers [103, 104], or a single pinhole with computer generated holograms [105].

5.6 Conclusion

To conclude, the orbital angular momentum properties of a second harmonic beam resulting from two non-collinear input beams with orbital angular momentum have been investigated. This

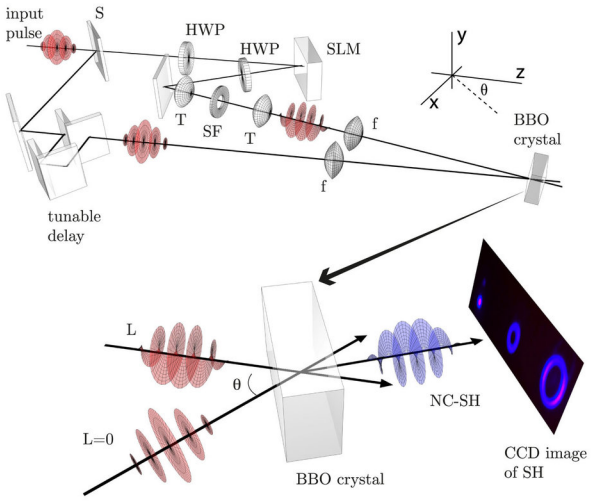

Figure 5.7: Experimental setup and figure taken from reference [94]. Diagram and description reproduced under the Creative Commons 3.0 license [106]: Input pulses are split by a beamsplitter (S), the reflected component, with Gaussian profile (L = 0), passes a tunable delay stage while the second traverses a fixed optical path in which the pulse's phase and amplitude are corrected (by a series of half-wave plates (HWP) and a spatial light modulator (SLM)) to impart OAM onto the beam (L). A spatial filter (an aperture (SF) in the Fourier plane of a 1:1 telescope (T)) removes higher order OAM modes and the beams (L = 0 and L) are loosely focussed (F) and overlapped non-collinearly onto a BBO crystal. The non-collinear output is measured with a photodetector.

investigation suggests that under certain conditions, interesting properties have surfaced with regard to the OAM power spectrum and also the possibility of pseudo non-conservation of orbital angular momentum on an individual photon basis – although a net conservation of orbital angular momentum when considering a statistically large number of photons. The single shot non-conservation of orbital angular momentum most likely does conserve angular momentum, where the gained or lost angular momentum is exchanged with the medium. It would be interesting to develop a more detailed beam propagation method and experiment to verify these peculiar results.

CHAPTER 6

Dichroism for orbital angular momentum using parametric amplification

6.1 Introduction

The term dichroism has two common meanings in optics. The original meaning refers to a material with optical properties that depend on the wavelength of light. For example, a dichroic beamsplitter will reflect one range of wavelengths while transmitting another. A more recent form of dichroism filters not by wavelength but instead by the polarization state of light. A polarizing beamsplitter is the most common example, which transmits one linear polarization of light while reflecting the orthogonal linear polarization of light. This is known as linear dichroism. In addition to filtering based on linear polarization, a material can also filter based on circular polarization state of light, applying a gain to one circular polarization σ_+ while attenuating the other orthogonal circular polarization state, σ_-. The polarization state of light refers to the direction (linear) or the rotation (circular/elliptical) of the electric field vector. In the quantum view, the σ_+ and σ_- polarization states represent two orthogonal spin angular momentum states in the light field. Thus, circular dichroism can also be thought of as a dichroism based on the spin angular momentum (SAM) state of a light field.

SAM is one of two types of angular momentum possessed by light, the other being orbital angular momentum (OAM). The spin angular momentum of light can sustain two orthogonal states, σ_+ and σ_- or horizontal and vertical polarization, whereas the orbital angular momentum of a light beam can possess an infinite number of mutually orthogonal states identified by the quantum number m which can take on any integer value. The advantage of OAM, as opposed to SAM, is that an in principle an infinite number of orthogonal channels can co-propagate at the same wavelength.

The purpose of this chapter is to provide background information and summarize the results of "Dichroism for orbital angular momentum using parametric amplification" [107]. The complete manuscript is reprinted in appendix A. The manuscript theoretically and numerically investigates parametric amplification as a means to produce dichroism based on the orbital angular momentum (OAM) of an incident signal field. The parametric interaction is demonstrated to provide differential gain between signal states of differing OAM with the peak gain occurring at half the pump field OAM. Parametric interactions involving fundamental and second-harmonic fields carrying OAM have previously been explored both experimentally and theoretically but mainly in the context of the conservation of OAM [108–110] as opposed to creating dichroism for OAM.

The manuscript in Appendix A describes the geometry and governing equations for our system, presents a simplified analytic theory of parametric amplification and dichroism for OAM for pump and signal beams that are perfect optical vortices, and lastly presents numerical results generated using beam propagation methods for the case of signal and pump fields that are imperfect optical vortices and also signal fields that are Laguerre-Gaussian beams. Specifically, we demonstrate that parametric amplification can be used to create gain for a band of OAM states of an incident signal beam.

6.2 Summary of numerical and analytical results

The basic system layout is illustrated in figure 6.1. The signal beam, an ordinary wave with slowly varying envelope A_1 at fundamental frequency ω with orbital angular momentum winding m_1, and the pump beam, an extraordinary wave with slowly varying envelope A_2 at the second harmonic frequency 2ω with orbital angular momentum winding m_2, are collinear.

In the nonlinear medium, the coupled fundamental and extraordinary waves propagate according to

$$\frac{\partial A_1}{\partial z} = \frac{i}{2k_1}\nabla_\perp^2 A_1 + i\eta A_2 A_1^* \tag{6.1}$$

and

$$\frac{\partial A_2}{\partial z} = \frac{i}{4k_1}\nabla_\perp^2 A_2 + i\eta A_1^2, \tag{6.2}$$

where $\nabla_\perp^2$ is the transverse Laplacian describing beam diffraction, $\eta = 2\omega_1 d_{\text{eff}}/n_1 c$, d_{eff} is the nonlinear coefficient, k_1 is the z-component of the fundamental wave vector, and n_1 is the index seen by the fundamental beam. The first term in each equation is due to diffractive effects and the second term in each equation accounts for the parametric process.

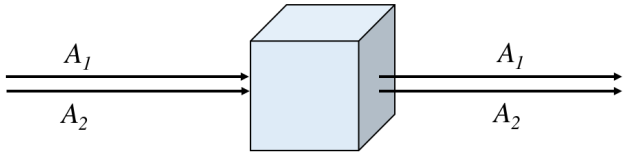

Figure 6.1: Illustration of the optical layout for dichroism for OAM. The signal beam, A_1 at the fundamental frequency ω, and the pump beam, A_2 at second harmonic frequency ω_2, pass through a nonlinear medium.

The difference in orbital angular momentum between the signal and pump beam is characterized by $\Delta = (m_1 - m_2/2)$. The parametric amplification causes the signal beam to experience gain or attenuation that is a function of the orbital angular momentum difference $G(\Delta)$.

A representative gain profile is shown in figure 6.2 for the case of a signal power of 52.8 kW, pump powers with peak intensities 4.4 and 8.8 GW/cm^2, pump OAM winding number $m_2 = 11$. This is with a optical vortex beam radius of 35 μm and medium length of 500 μm. The spiral

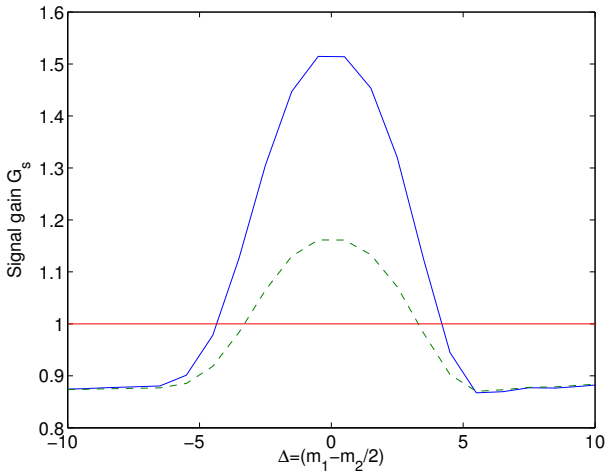

Figure 6.2: Signal gain versus the OAM difference Δ an LBO crystal with pump beam OAM $m_2 = 11$, and a pump intensity of $I_p = 8.8$ GW/cm^2 (solid line) and $I_p = 4.4$ GW/cm^2 (dashed line), the signal power being held constant at $P_{sig} = 0.2P_2(0) = 52.8$ kW. The discrete data points are connected by a solid line as a visual aid. The optical vortex radius is 35 μm and the medium length is 500 μm.

bandwidth of the gain profile is defined to be the width of the gain profile in terms of Δ and is analytically approximated to be

$$\delta\Delta = 2\sqrt{\frac{\pi k_1 R^2}{L}}, \tag{6.3}$$

where k_1 represents the fundamental wave vector, R represents the radius of the optical vortex beam, and L represents the length of the nonlinear medium. The peak gain occurs for a signal OAM equal to half that of the pump field, and the peak signal gain increases with the pump power. The overall analytical gain bandwidth is in good agreement with the numerical profile shown in figure 6.2. The peak gain is found to be

$$G_{\text{peak}} = \cosh^2\left(\sqrt{\beta I_p} L\right), \tag{6.4}$$

where $\beta = (2\omega_1^2 d_{\text{eff}}^2/\epsilon_0 n^3 c^3)$, d_{eff} is the nonlinear coefficient, ω_1 is the fundamental frequency, and I_p is the peak pump intensity. This type of dichroic parametric amplification could be used to provide significant gain to a band of the probe OAM which could be used to bias the OAM content of an incident signal beam or the oscillating OAM states in an active system such as a laser. This dichroism could also be used to vary the gain for a specific probe OAM dependent on the sign of the OAM of the pump, and this could be used for all-optical switching of the probe or multiplexing of OAM states in a communication line, which I will discuss briefly in the following section.

6.3 Applications and potential technologies

One interesting potential application of OAM dichroism is in the field of communications. The ability of an optical fiber to sustain multiple orthogonal spatial modes, such as the OAM states, could multiply the optical fiber data transmission capacity by the number of distinguishable orthogonal OAM states carried by the optical fiber. Space division multiplexing is being explored as one avenue to increase data communications rates [111]. Hollow core fibers have been developed and would be suitable for transmitting OAM beams because of the reduced roughness: the light is traveling in air rather than in a fabricated glass material, thus allowing for more spatial modes to be resolved [112]. Reference [113] has demonstrated the fabrication of optical fibers capable of sustaining multiple OAM modes as well as techniques for coupling free space OAM beams into and out of these fibers. The discrepancy between optical data transmission rates and traffic demand is expected to create a capacity shortage in the near term [114], and as opposed to a technological limit, for single spatial mode optical transmission this is due to a fundamental physical limit for information transmission [115]. Reference [116] describes spatial domain multiplexing, such as OAM multiplexing, as the "last degree of freedom available" to further data capacity limits.

Thus, in the field of communications, the concept of OAM dichroism could be used to optically multiplex a signal containing a range of orthogonal OAM states. An example of how this could be accomplished is illustrated in figure 6.3. The example illustrates the multiplexing of three OAM states, however, the same principle could be applied to an arbitrarily large number of OAM states.

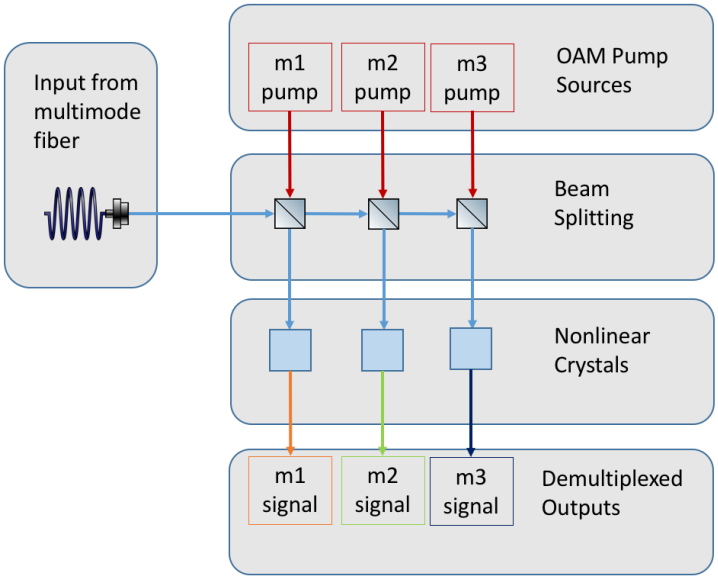

Figure 6.3: A theoretical OAM multiplexer is illustrated. The system receives a signal from a multimode fiber that contains a range of signals each carried by a different OAM state. Beamsplitters are used to split the input signal into multiple channels. Each separate channel is amplified by a pump signal with a specified orbital angular momentum so as to select out a single OAM state for each output by amplifying the OAM of interest and attenuating the others.

CHAPTER 7

Conclusions

This dissertation has described four different studies of the manipulation, modeling, and measurement of nonlinear wave phenomena for both optical and atomic media: (1) minimally destructive *in situ* detection of vortex cores, (2) methods for imprinting vortex dipoles into BECs, (3) a theoretical investigation of a method for generating a spectrum of orbital angular momentum states in an optical beam, and (4) the theoretical development of a method for narrowing the spectrum of orbital angular momentum states in an optical beam termed dichroism for OAM. This final chapter serves to contextualize the key results of each study.

The minimally destructive methods for *in situ* detection of vortex cores serve as a proof of principle; however, the method and apparatus are not yet suitable for scientific studies of 2D vortex dynamics in our highly oblate traps. In particular, detection was only observed repeatedly for vortex lattices in less oblate BEC geometries, whereas the turbulent systems that we are interested in studying contain irregularly spaced vortices and other features in a highly oblate BEC geometry. In the analysis segment of the *in situ* vortex detection chapter, it is discussed that perhaps the reason for vortices being observed in some cases only when regularly spaced is due to the perception of the human visual system to confidently identify a regular structure. The vortex SNR was identified as ranging in example images from 1.5 for dark-filed imaging, to 2.2 for absorption imaging, and 3.1 for Faraday imaging.

While Faraday and dark field imaging demonstrated high signal levels, these two methods both had highly nonuniform signal levels likely due to the dependence on the column density of the BEC, which varies significantly over the BEC's spatial extent in a harmonic confining potential. For this reason, absorption imaging may be the best going forward in future studies in harmonic confining potentials. On the other hand, if studies are pursued in a flat-bottom potential or another trapping geometry that has more spatially uniform bulk BEC density profiles, Faraday or dark-field imaging may prove more optimal.

For each of the imaging methods investigated, I hypothesize that one of the major detractors to the SNR is the low NA of the imaging system, which serves to spatially average out the vortex signal. The NA could be increased by a factor of two in future iterations, which would reduce the area over which the vortex signal is averaged out over by a factor of four if an appropriate magnification is chosen to match the diffraction limited spot size to the detector's pixel pitch. Limitations of physics dictate a maximum possible NA; however, the spatial averaging of the signal could also be further reduced by choosing a system with weaker trapping frequencies

such that the BEC healing length is larger. Future work towards *in situ* detection of vortices is underway in a new lab optimized specifically for studying quantum turbulence.

The mechanism for vortex dipole imprinting through the use of a stationary red-detuned beam and a blue-detuned beam was investigated both numerically and theoretically. Critical regions for optimal vortex dipole nucleation were identified and a physical mechanism for implementing vortex dipole imprinting was prototyped. When the prototyped mechanism is fully implemented we anticipate that it will serve as a more effective means to introduce vortex dipoles in the BECs than any previous methods.

In addition to functioning as a method to imprint vortex dipoles, the introduction of a steerable red-detuned beam will also enable a range of experiments regarding the superfluid flow around dynamic narrow attractive potential wells. Preliminary investigations into another future technology for rapidly architecting arbitrary configurations of vortices are also underway and will involve the use of a digital micromirror device (DMD). With the DMD, in principle it will be possible to independently control many blue-detuned and red-detuned beams with time-dependent positions and amplitudes. With this technological capability and the knowledge of vortex dipole imprinting investigated in this dissertation, it will hopefully be possible to repeatedly implement a wide variety of vortex configurations initial conditions for future studies of quantum turbulence.

Two chapters of this dissertation were spent investigating orbital angular momentum spectra of optical beams. Specifically, the first method uses second harmonic generation of two tilted beams, one with zero orbital angular momentum and the other with nonzero orbital angular momentum. The resulting noncollinear beam is found to be in a superposition of OAM states. On the other hand, the second investigation does the opposite: using parametric amplification a pump beam at the second harmonic frequency with OAM applies a differential gain to a signal beam which could in principle contain a spectrum of OAM states. The differential gain is shown analytically and numerically to have a gain bandwidth termed the spiral bandwidth. The two methods that were theoretically investigated are complementary in that one is designed to broaden an OAM spectrum whereas the other is designed to narrow the OAM spectrum.

To conclude, the various studies described in this body of work represent steps in the understanding of nonlinear wave phenomena. The BEC aspect of this research has advanced the area of vortex detection and secondly the area of engineering arbitrary BEC wave functions. The combination of these new capabilities moves the state-of-the-art of quantized vortex research toward the goal of experimentally investigating fundamental questions regarding two-dimensional quantum turbulence such as those posed by Onsager [117]. The nonlinear optics aspect of this research can draw analogs to the BEC research in that the dynamics of both systems are fundamentally related; however, the utility of the nonlinear optics research is perhaps more relevant to our understanding of the capabilities of OAM-carrying optical beams with the most obvious applications being in the field of telecommunications and these theoretical investigations set the

stage for experimental realization of new capabilities for sculpting the OAM spectra of optical sources.

APPENDIX A

Dichroism for orbital angular momentum using parametric amplification

PHYSICAL REVIEW A **90**, 053828 (2014)

Dichroism for orbital angular momentum using parametric amplification

J. Lowney,[1] T. Roger,[2] D. Faccio,[1,2] and E. M. Wright[1,*]
[1]*College of Optical Sciences, University of Arizona, Tucson, Arizona 85721-0094, USA*
[2]*Institute of Photonics and Quantum Sciences, School of Engineering and Physical Sciences, Heriot-Watt University, EH14 4AS Edinburgh, United Kingdom*
(Received 3 September 2014; published 14 November 2014)

We theoretically analyze parametric amplification as a means to produce dichroism based on the orbital angular momentum (OAM) of an incident signal field. The nonlinear interaction is shown to provide differential gain between signal states of differing OAM, the peak gain occurring at half the OAM of the pump field.

DOI: 10.1103/PhysRevA.90.053828 PACS number(s): 42.50.Tx, 42.65.Lm

I. INTRODUCTION

One usage of the term dichroism in optics is to describe the differential loss of monochromatic light in one of two orthogonal polarization states with respect to some reference axis. This definition encompasses the case of both linear and circular dichroism and also gain and/or loss if one allows for negative absorption. For example, circular dichroism refers to the case in which right-handed circular (RHC) and left-handed circular (LHC) polarizations experience different propagation losses in the dichroic medium. As is well known, the RHC and LHC polarized states represent two orthogonal spin angular momentum (SAM) states for the light field. Then another way to express circular dichroism is that it is a dichroism based on the SAM state of the incident light field, or simply dichroism for SAM.

The goal of this paper is to propose and theoretically investigate parametric amplification as a means to produce dichroism based on the orbital angular momentum (OAM) of an incident signal field. The parametric interaction is shown to provide differential gain between signal states of differing OAM, the peak gain occurring at half the pump field OAM. Parametric interactions involving fundamental and second-harmonic fields carrying OAM have previously been explored both experimentally and theoretically, but mainly in the context of the conservation of OAM [1–3] as opposed to creating dichroism for OAM. A recent paper discussed circular dichroism that has its origin in the OAM of a beam incident on a nonchiral structure [4], whereas here we elucidate a means to produce dichroism that acts on the incident beam OAM directly.

The remainder of this paper is organized as follows. Section II describes the geometry and governing equations for our system and Sec. III presents a simplified analytic theory of parametric amplification and dichroism for OAM for pump and signal beams that are perfect optical vortices. In Sec. IV numerical results are presented for the case of signal and pump fields that are imperfect optical vortices and also signal fields that are Laguerre-Gaussian beams. Specifically, we demonstrate that parametric amplification can be used to create gain for a band of OAM states of an incident signal beam with absorption outside this band. A summary and conclusions are given in Sec. V.

*Corresponding author: ewan@optics.arizona.edu

II. BASIC GEOMETRY AND EQUATIONS

Our basic model involves propagation in the transparency region of a uniaxial nonlinear optical crystal. More specifically, we consider propagation along a principal axis to avoid the effects of beam walkoff and assume type-I phase-matching conditions. In our model of parametric amplification a signal field at the fundamental frequency ω_1 is incident on the crystal along with a pump field at the second-harmonic (SH) frequency $\omega_2 = 2\omega_1$. In this case the parametric interaction will generate an idler field at the fundamental frequency $\omega_3 = \omega_2 - \omega_1 = \omega_1$. For the type-I phase matching assumed, the signal field and idler fields are ordinary waves of refractive index n_1 and the pump is an extraordinary wave with refractive index n_2. Then, choosing the z axis as the propagation direction, denoting the complex slowly varying field amplitudes of the fundamental and SH fields as $A_1(x,y,z)$ and $A_2(x,y,z)$, and following the derivation and notation of Ref. [5], we obtain the paraxial wave equations for the fundamental ($j = 1$) and pump ($j = 2$) fields

$$\begin{aligned}\frac{\partial A_1}{\partial z} &= \frac{i}{2k_1}\nabla_\perp^2 A_1 + \frac{2i\omega_1^2 d_{\rm eff}}{k_1 c^2} A_2 A_1^* e^{-i\Delta k z},\\ \frac{\partial A_2}{\partial z} &= \frac{i}{2k_2}\nabla_\perp^2 A_2 + \frac{i\omega_2^2 d_{\rm eff}}{k_2 c^2} A_1^2 e^{i\Delta k z},\end{aligned} \tag{1}$$

where $\nabla_\perp^2 = \frac{\partial^2}{\partial x^2} + \frac{\partial^2}{\partial y^2}$ is the transverse Laplacian describing beam diffraction, $d_{\rm eff}$ is the effective nonlinear coefficient, $k_j = n_j\omega_j/c$ gives the z component of the wave vector for the two fields, and $\Delta k = 2k_1 - k_2$ is the wave-vector mismatch. We note that in this formulation the fundamental field incorporates both the signal and idler fields. Throughout this paper we assume the case of noncritical phase matching in a lithium triborate (LBO) crystal and a fundamental wavelength of $\lambda_1 = 1.064\ \mu$m for which $n_1 = n_2 = n = 1.6$, $\Delta k = 0$, and $d_{\rm eff} = 0.83$ pm/V. Then introducing the parameter $\eta = 2\omega_1 d_{\rm eff}/n_1 c$, the propagation equations may be written as

$$\begin{aligned}\frac{\partial A_1}{\partial z} &= \frac{i}{2k_1}\nabla_\perp^2 A_1 + i\eta A_2 A_1^*,\\ \frac{\partial A_2}{\partial z} &= \frac{i}{4k_1}\nabla_\perp^2 A_2 + i\eta A_1^2.\end{aligned} \tag{2}$$

These propagation equations for parametric amplification are to be solved for input fields that have cylindrically symmetric intensity profiles and carry OAM specified by the winding

numbers m_1 for the signal and m_2 for the pump

$$A_j(x,y,z=0)=\alpha_j U_j(\rho,z=0)e^{im_j\phi},\quad j=1,2, \tag{3}$$

where (ρ,ϕ) are the transverse coordinates in cylindrical coordinates and the complex coefficients α_j are used to control the input powers of the fundamental and second-harmonic fields along with the relative phase θ between the input fundamental and SH fields. Here $U_j(x,y,z)\equiv U_j(\rho,z)$ are normalized cylindrically symmetric field profiles obeying

$$\int_{-\infty}^{\infty}dx\int_{-\infty}^{\infty}dy|U_j(x,y,z)|^2=\int_0^{\infty}2\pi\rho d\rho|U_j(\rho,z)|^2=1, \tag{4}$$

which describe the input fields at $z=0$ and their linear propagation to the output at $z=L$. The output powers in the fundamental and SH fields can be expressed as

$$P_j(L)=2\epsilon_0 nc\int_{-\infty}^{\infty}dx\int_{-\infty}^{\infty}dy|A_j(x,y,L)|^2,\quad j=1,2, \tag{5}$$

and we note that $P_1(L)$ represents the total fundamental output power, signal plus idler. We furthermore define the output signal power

$$P_s(L)=2\epsilon_0 nc\left|\int_{-\infty}^{\infty}dx\int_{-\infty}^{\infty}dyU_1^*(x,y,L)e^{-im_1\phi}A_1(x,y,L)\right|^2, \tag{6}$$

which represents the power contained in the fundamental field projected onto the normalized input signal mode $U_1(x,y,L)e^{im_1\phi}$ evaluated at the output. In particular, $P_s(L)$ provides a measure of the output power associated with the input signal winding number m_1. In the following we shall examine the net gain for the fundamental field

$$G=\frac{P_1(L)}{P_{\rm sig}}, \tag{7}$$

$P_{\rm sig}=P_1(0)$ being the input signal power, and the signal gain

$$G_s=\frac{P_s(L)}{P_{\rm sig}}. \tag{8}$$

In general, $P_1(z)>P_s(z)$ and $G>G_s$ since the nonlinear interaction will generate an idler field at the fundamental frequency from the pump and signal fields. We shall always choose the input pump power somewhat larger than the signal power to avoid excessive pump depletion.

III. SIMPLIFIED ANALYTIC THEORY

To set the stage for our numerical simulations we first present a simplified analytic theory of parametric amplification with OAM and associated dichroism. In particular, we consider the case that both the signal and pump beams are perfect optical vortices (POVs) [6,7]. A perfect optical vortex of winding number m has a narrow ring intensity profile with an azimuthal phase twist of $2\pi m$ in the transverse plane of the field. The key to using POVs is that the ring radius R should be independent of winding number and the same for all interacting fields. This choice maximizes the spatial overlap of the interacting fields and allows for a treatment that removes issues related to the radial profile of the fields while retaining the azimuthal variation.

A. Perfect optical vortices

We first present a representation of a monochromatic POV with frequency $\omega=2\pi c/\lambda$ and winding number m propagating in a medium of refractive index n. The POV has a ring-shaped intensity profile of radius R and width W, $R\gg W\gg\lambda$, along with a helical phase front of winding number m. (In the ideal case the ring width W would be zero [6].) We assume that the width W of the POV is sufficiently narrow compared to the ring radius that we may evaluate the properties of the beam around the peak of the ring. Then, for a POV with azimuthal variation $e^{im\phi}$ propagating along the z axis, the corresponding spiraling wave vector may be written as [8]

$$\begin{aligned}\vec{K}&=K_x\vec{e}_x+K_y\vec{e}_y+K_z\vec{e}_z\\&=\frac{m}{R}\cos(\phi)\vec{e}_x+\frac{m}{R}\sin(\phi)\vec{e}_y+K_z\vec{e}_z,\end{aligned} \tag{9}$$

with $R\gg\lambda$ the ring radius. By demanding that $K=k=2\pi n/\lambda$ we obtain for a forward propagating field

$$K_z=\sqrt{k^2-\frac{m^2}{R^2}}\approx k-\frac{1}{2k}\frac{m^2}{R^2}, \tag{10}$$

so we get the expected reduction in the z component of the wave vector due to the skewing associated with the helical phase front of the POV [9].

Based on the above results, the slowly varying electric field envelope for a POV evaluated around the peak of the ring may be written as

$$A(\rho=R,\phi,z)=a(z)e^{im\phi}e^{-(iz/2k)(m^2/R^2)}. \tag{11}$$

Then approximating the field of the POV as constant over its cross section, the power may be evaluated as

$$P(z)=2\epsilon_0 nc2\pi RW|a(z)|^2. \tag{12}$$

The utility of this solution rests on the Rayleigh range $z_R=kW^2/2$ being larger than the medium length L so that the ring width will vary little under propagation through the medium.

In the next subsection we consider a superposition of POVs at the fundamental frequency but with different winding numbers to capture both the signal and idler fields.

B. Parametric amplification

For this development we assume that the pump field ($j=2$) is much stronger than the signal field ($j=1$). Then the parametric amplification process, which produces one signal and one idler photon from one pump photon, generates an idler field ($j=3$) that has winding number $m_3=m_2-m_1$. Assuming that all fields are described by POVs, we then write the slowly varying electric fields for the fundamental and second harmonic fields, with $\rho=R$, as

$$\begin{aligned}A_1(\phi,z)&=a_1(z)e^{im_1\phi}e^{-(iz/2k_1)(m_1^2/R^2)}\\&\quad+a_3(z)e^{im_3\phi}e^{-(iz/2k_1)(m_3^2/R^2)},\\A_2(\phi,z)&=a_2e^{im_2\phi}e^{-(iz/2k_2)(m_2^2/R^2)},\end{aligned} \tag{13}$$

with a_2 independent of z in the undepleted pump beam approximation and $a_3(0) = 0$ with no idler present at the input. Here we have set $k_3 = k_1$ since the signal and idler have the same frequency, and type-I phase matching is employed so the signal and idler experience the same refractive index. In the Appendix we show that using the fields in Eqs. (13) along with the propagation equations (2) yields the linearized signal-idler equations

$$\frac{da_1}{dz} = i(\eta a_2)a_3^* e^{i\kappa z}, \quad \frac{da_3}{dz} = i(\eta a_2)a_1^* e^{i\kappa z}, \tag{14}$$

where the OAM-dependent wave-vector mismatch for the process is

$$\kappa = \frac{(m_1 - m_2/2)^2}{k_1 R^2} \tag{15}$$

and we note that phase matching $\kappa = 0$ requires $m_1 = m_2/2$. These equations may be solved for the fields at the output of the crystal of length L [5],

$$\begin{aligned} a_1(L) &= a_1(0)\left(\cosh(gL) - \frac{i\kappa}{2g}\sinh(gL)\right)e^{i\kappa L/2}, \\ a_3(L) &= a_1^*(0)\left(\frac{i\eta a_2}{g}\right)\sinh(gL)e^{i\kappa L/2}, \end{aligned} \tag{16}$$

where $g = \sqrt{\eta^2|a_2|^2 - \kappa^2/4}$ is the growth rate if the argument of the square root is positive. The field intensities are given by $I_j(z) = 2\epsilon_0 nc|a_j(z)|^2$ in terms of which the growth rate may be written as

$$g = \sqrt{\beta I_p - \kappa^2/4}, \tag{17}$$

with $I_p = I_2(0)$ is the pump intensity at the peak of the ring and $\beta = 2\omega_1^2 d_{\rm eff}^2/\epsilon_0 n^3 c^3$. Using Eq. (12), the input signal power is $P_{\rm sig} = 2\epsilon_0 nc2\pi RW|a_1(0)|^2$, the output fundamental power is $P_1(L) = 2\epsilon_0 nc2\pi RW[|a_1(L)|^2 + |a_3(L)|^2]$, and the output signal power is $P_s(L) = 2\epsilon_0 nc2\pi RW|a_1(L)|^2$. Then the net gain for the fundamental field may be expressed as

$$G = \frac{P_1(L)}{P_{\rm sig}} = \left|\cosh(gL) - \frac{i\kappa}{2g}\sinh(gL)\right|^2 + \left|\frac{\eta a_2}{g}\sinh(gL)\right|^2 \tag{18}$$

and the signal gain becomes

$$G_s = \frac{P_s(L)}{P_{\rm sig}} = \left|\cosh(gL) - \frac{i\kappa}{2g}\sinh(gL)\right|^2. \tag{19}$$

Note that under phase matching $\kappa = 0$ the peak signal gain is

$$G_{\rm peak} = \cosh^2(\sqrt{\beta I_p}L), \tag{20}$$

which increases with pump intensity.

In summary, the simplified analytic solution demonstrates that phase matching for the parametric amplification process depends on the combination of the winding numbers of the signal and pump beams

$$\Delta = m_1 - \frac{m_2}{2}, \tag{21}$$

whereas the peak signal gain varies with the input intensity.

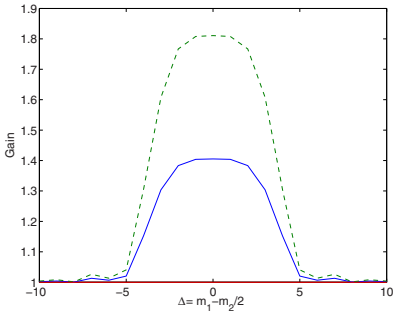

FIG. 1. (Color online) Signal gain G_s (solid line) and net gain (dashed line) versus the OAM difference $m_1 - m_2/2$ for a LBO crystal of length $L = 2$ mm, pump intensity $I_2 = 2$ GW/cm^2, and ring radius $R = 35$ μm. The discrete data points are connected by a solid line as a visual aid.

C. Dichroism for OAM

Figure 1 shows an illustrative example of the signal gain G_s (solid line) and net gain G (dashed line) versus the OAM difference $\Delta = m_1 - m_2/2$ for a LBO crystal of length $L = 2$ mm, pump intensity $I_p = 2$ GW/cm^2, and a ring radius $R = 35$ μm. We have chosen the example of a LBO crystal as it allows for the assumed noncritical phase matching and has a damage threshold that exceeds the intensities used for pulses shorter than a nanosecond. Figure 1 reveals that significant gain occurs for a limited range of OAM values centered on $\Delta = 0$, that is, around $m_1 = m_2/2$. The fact that the peak of the net gain defined in Eq. (7), which includes both the signal and idler, exceeds the peak of the signal gain defined in Eq. (8) reflects the fact that a significant idler intensity is generated in this example, but we note that gain appears over a similar range in both cases. The full width for the parametric gain profile may be estimated by requiring $\kappa L = \pi$ at the edges for the phase mismatch to diminish the gain, which yields

$$\delta\Delta = 2\sqrt{\frac{\pi k_1 R^2}{L}}. \tag{22}$$

This full width scales as $\delta\Delta \propto R/\sqrt{\lambda_1 L}$, which is analogous to the spiral bandwidth used in spontaneous parametric down-conversion if we replace the Gaussian waist of the pump beam with the ring radius [10–12]. For this reason we refer to $\delta\Delta$ as the spiral bandwidth. For the chosen parameters this yields a spiral bandwidth of $\delta\Delta = 9$ in reasonable agreement with Fig. 1. Note also that the spiral bandwidth is independent of the winding numbers of the incident fields.

The parametric amplification therefore provides differential gain between different OAM states of the signal beam and in this sense acts as a dichroic element based on the signal OAM with the peak gain centered at $m_1 = m_2/2$ and spiral bandwidth given by Eq. (22). Furthermore, if we choose $|m_2| > \delta\Delta$, then for $m_2 > 0$ we can create the situation such

that only OAM states with $m_1 > 0$ experience significant gain and vice versa for $m_2 < 0$.

This concludes our discussion of the simplified analytic theory. Next we turn to numerical simulations using more realistic and practical beam profiles that will expose more general features of parametric amplification and associated dichroism for OAM.

IV. NUMERICAL SIMULATIONS

In this section we present numerical simulations of parametric amplification for more realistic types of input beams. The simulations are based on Eqs. (2) with initial conditions corresponding to signal and pump beams carrying OAM as in Eqs. (3). A standard beam propagation method is employed for the nonlinear propagation [13].

A. Imperfect optical vortices

Here we consider input beams that have a ring structure plus helical phase fronts, but they are not ideal POVs, so we term them imperfect optical vortices (IOVs). In particular, with reference to Eqs. (3), we write the radial profiles of the input fields as

$$U_j(\rho,z=0) = \mathcal{N}_j \rho^{m_r} e^{-\rho^2/w_0^2}, \quad j = 1,2, \qquad (23)$$

where $\mathcal{N}_j$ are normalization constants, w_0 is a Gaussian beam waist, and m_r is a positive integer. Equations (23) describe annular beams of ring radius $R = w_0\sqrt{m_r/2}$ and for our numerics we choose $w_0 = 15$ μm, in which case the ring radius is $R = 35$ μm for $m_r = 11$. We note that these initial conditions do not coincide with the familiar Laguerre-Gaussian modes of free space unless $|m_{1,2}| = m_r$, so these IOVs will generally change their functional form under linear propagation. For our parameters the fundamental Rayleigh range is $z_R \simeq 1$ mm, whereas the medium length is $L = 2$ mm, so the IOVs experience non-negligible diffraction over the medium length.

Figure 2 shows illustrative examples of parametric amplification using IOVs with parameters $m_r = 11$ and $w_0 = 15$ μm giving $R = 35$ μm, an input pump power of $P_2(0) = 264$ kW, and a signal power of $P_{\rm sig} = 0.2P_2(0) = 52.8$ kW, these parameters yielding an intensity of $I_p = 8.8$ GW/cm^2 around the peak of the pump beam. The signal gain G_s given in Eq. (8) is plotted as a function of the OAM difference $\Delta = m_1 - m_2/2$ for the cases with $m_2 = 0$ (dotted line) and $m_2 = 11$ (solid line).

The results in Fig. 2(a) display qualitative similarities and differences with the simplified analytic theory in Fig. 1 that we now discuss. First, except for $\Delta = 0$, the results for the two different pump winding numbers $m_2 = 0,11$ agree very well, this being expected from the simplified theory. However, for the case of zero winding number for both the pump and probe $m_1 = m_2 = \Delta = 0$ (dashed line), the signal gain shows an absorption dip. This arises since under this condition there is a resonant interaction between the injected fundamental field and the SH field that preserves the winding number of each field and depends on the relative phase θ between the signal and SH. For the case shown $\theta = \pi/4$ this yields absorption, whereas for $\theta = -\pi/4$ signal gain occurs [3]. In contrast, the

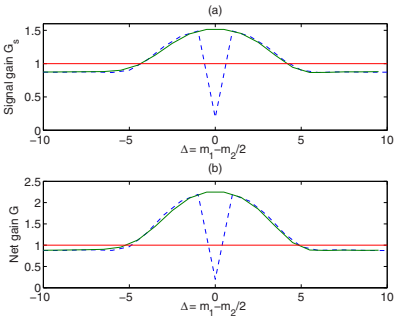

FIG. 2. (Color online) (a) Signal gain G_s versus the OAM difference $\Delta = m_1 - m_2/2$ for $m_2 = 0$ (dotted line) and $m_2 = 11$ (solid line) and (b) same as (a) but for the net gain G. The parameters used are for LBO and $m_r = 11$, $w_0 = 15$ μm, giving $R = 35$ μm, an input pump power of $P_2(0) = 264$ kW, and a signal power of $P_{\rm sig} = 0.2P_2(0) = 52.8$ kW, giving a peak intensity $I_p = 8.8$ GW/cm^2. The discrete data points are connected by a solid line as a visual aid.

case with $m_2 = 11$ shows no such absorption at $\Delta = 0$. This is because the resonant interaction between the fundamental and SH fields at $\Delta = 0$ requires $m_1 = m_2/2$, which cannot be satisfied for integer m_1 if m_2 is odd, but the absorption dip does appear at $\Delta = 0$ if m_2 is even. So excluding the dip at $\Delta = 0$, the results for $m_2 = 0,11$ agree well. Note also that in Fig. 2(a) the signal gain turns to absorption for larger values of $|\Delta|$. This background absorption arises from conversion of the fundamental field with OAM m_1 to SH with OAM $2m_1$ (generally distinct from the input SH with OAM m_2.) The magnitude of this background absorption increases as the input signal power is increased. Furthermore, the width of the central peak in Fig. 2(a) is around 9, which is close to the spiral bandwidth $\delta\Delta = 9$ obtained from Eq. (22), the parameters being the same as in Fig. 1.

Figure 2(b) is the same as Fig. 2(a) but for the net gain given by the total fundamental output power divided by the input signal power. Figures 2(a) and 2(b) show the same features, but the net gains are larger than the signal gains due to the inclusion of the idler power in the net gain. The reason for this figure is to demonstrate that the common features appear in both gains and it is simpler to measure the net gain experimentally than to isolate the signal gain. Both gain measurements would demonstrate that the differential gain or loss between different signal OAM states depends on the OAM difference $\Delta = m_1 - m_2/2$.

Further features of the signal gain G_s are illustrated in Fig. 3. This figure shows the signal gain versus the OAM difference $\Delta = m_1 - m_2/2$ for the same parameters as in Fig. 2(a) with $m_2 = 11$ and pump intensities of $I_p = 8.8$ GW/cm^2 (solid line) and $I_p = 4.4$ GW/cm^2 (dashed line), the signal power being held constant at $P_{\rm sig} = 52.8$ kW. As expected on the basis of Eq. (20), the peak signal gain increases with

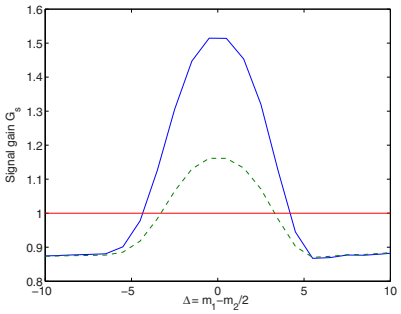

FIG. 3. (Color online) Signal gain G_s versus the OAM difference $\Delta = m_1 - m_2/2$ for the same parameters as in Fig. 2(a) with $m_2 = 11$ and a pump intensity of $I_p = 8.8$ GW/cm^2 (solid line) and $I_p = 4.4$ GW/cm^2 (dashed line), the signal power being held constant at $P_{sig} = 0.2P_2(0) = 52.8$ kW. The discrete data points are connected by a solid line as a visual aid.

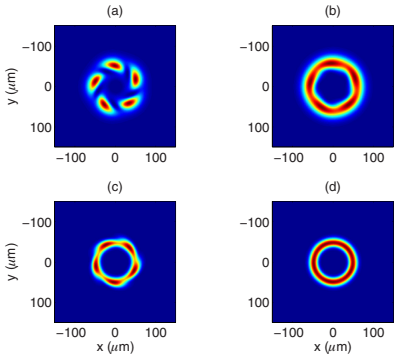

FIG. 4. (Color online) Examples of the (a) and (b) fundamental and (c) and (d) SH output transverse intensity profiles for two different values of the pump power: (a) and (c) $P_2(0) = 264$ kW and (b) and (d) $P_2(0) = 2.64$ kW, with $P_{sig} = 0.2P_2(0)$, all other parameters being the same as in Fig. 2. The winding numbers of the fundamental and SH fields were chosen as $m_1 = 8$ and $m_2 = 11$ so that $\Delta = 2.5$ and the generated idler will have winding number $m_3 = m_2 - m_1 = 5$.

pump intensity and given a peak signal gain of $G_{peak} = 1.5$ for the higher pump intensity, Eq. (20) predicts $G_{peak} = 1.23$ for the lower pump intensity, in reasonable agreement with the numerics [recall that the simple theory does not account for the background absorption due to second-harmonic generation (SHG) that is present in the numerics]. In contrast, we see that the background absorption is the same in both cases. This follows since the background absorption arises from SHG of the fundamental field of winding number m_1 to create a SH field with winding number $2m_1$, distinct from the pump SH field with winding number $m_2 = 11$, and this depends dominantly on the signal properties alone, not the pump properties.

Figure 4 shows illustrative examples of the fundamental (top row) and SH (bottom row) output transverse intensity profiles for two different values of the pump power $P_2(0) = 2.64$ and 264 kW, with $P_{sig} = 0.2P_2(0)$, all other parameters being the same as in Fig. 2. The winding numbers of the fundamental and SH fields were chosen as $m_1 = 8$ and $m_2 = 11$ so that $\Delta = 2.5$, and the generated idler will have winding number $m_3 = m_2 - m_1 = 3$. For Figs. 4(a) and 4(c) the pump power is $P_2(0) = 264$ kW and the fundamental intensity profile in Fig. 4(a) shows a five-lobe structure that arises from azimuthal beating between the signal and idler fields with azimuthal periodicity $2\pi/|m_1 - m_3| = 2\pi/5$. The pronounced lobes reflect the fact that a strong idler is generated in this case (as also evidenced by the difference between the net gain and signal gain in Fig. 2 for $\Delta = 2.5$). The five-lobe structure is also evident, but to a lesser degree, in the corresponding intensity profile for the SH shown in Fig. 4(c). Figures 4(b) and 4(d) show the same thing for a pump power $P_2(0) = 2.64$ kW, the key difference being that a weaker idler is generated and the five-lobe structure is less well pronounced. For even lower pump powers the intensity profiles tend closer to rings. In summary, many of the features present in the simplified analytic model are also present using signal and pump beams that are IOVs. The simplified theory did not include the SHG process, so it did not account for the resonant SHG that occurs for $m_1 = m_2/2$ or the background absorption of the signal due to generation of a SH field at $m_2 = 2m_1$. The simplified model did capture the spiral bandwidth of the parametric amplification process. It then follows that the dichroism for OAM displayed by the simple model may also be realized using IOVs. A key distinction is that whereas the simplified analytic theory only shows differential gain between signal OAM states, the full theory with IOVs shows gain for a band of OAM states and loss outside that band and in this sense the full theory is richer.

B. Laguerre-Gaussian signal

For our second example we consider the case that the pump beam is an IOV as in Eq. (23) but the signal beam is a Laguerre-Gaussian (LG) beam. For input beams other than POVs or IOVs the spatial overlap of the signal and pump beams introduces features beyond the simplified theory and we use the LG beams as an illustrative example due to their relative ease of generation in the laboratory. In particular we consider LG signal modes with radial mode index $p = 0$ and winding number m_1,

$$U_1(\rho, z = 0) = \mathcal{N}_j \rho^{|m_1|} e^{-\rho^2/w_0^2}, \tag{24}$$

the pump IOV and signal LG beam being based on the same Gaussian spot size w_0. For $m_1 = 0$ this is a Gaussian beam peaked on axis, whereas for $m_1 \neq 0$ this is a ring beam with radius $R_1 = w_0\sqrt{|m_1|/2}$, so the ring radius varies with

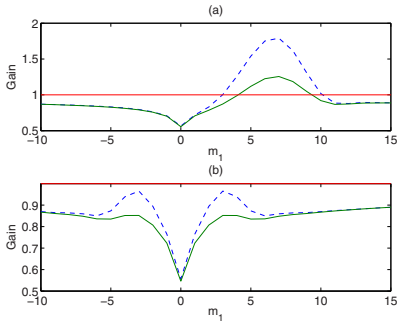

FIG. 5. (Color online) Plot of the signal gain G_s (solid line) and net gain G (dashed line) as functions of the signal beam winding number m_1 for a pump winding number (a) $m_2 = 11$ and (b) $m_2 = 0$. The parameter values are $m_r = 11$ and $w_0 = 15\mu$m, giving $R = 35\mu$m, an input pump power of $P_2(0) = 264$ kW, and a signal power of $P_{\rm sig} = 0.2P_2(0) = 52.8$ kW. The discrete data points are connected by a solid line as a visual aid.

winding number in contrast to the IOVs. For a pump beam that is an IOV as in Eq. (23) the ring sizes of the LG signal and pump beam will coincide when $m_r = |m_1|$.

Figure 5 shows illustrative examples of parametric amplification using LG signal beams with parameters $m_r = 11$ and $w_0 = 15\ \mu$m giving $R = 35\ \mu$m, an input pump power of $P_2(0) = 264$ kW, and a signal power of $P_{\rm sig} = 0.2P_2(0) = 52.8$ kW, these parameters yielding an intensity of $I_p = 8.8$ GW/cm^2 around the peak of the pump beam. In Fig. 5(a) the signal gain G_s (solid line) and net gain G (dashed line) are shown as a function of the signal beam winding number m_1 for a pump winding number $m_2 = 11$. This figure shows that parametric gain occurs over a band of winding numbers with peak gain centered around $m_1 \simeq 7$, with absorption outside of this gain band. The gain peak is shifted with respect to the phase-matching condition $m_1 = m_2/2 = 5.5$, but this is not surprising since the overlap between the interacting fields, which enters into the strength of the parametric wave interaction, varies with m_1. Although the gain profile is asymmetric, the results in Fig. 5(a) largely conform to the findings based on the using IOVs. This example demonstrates that by judicious choice of signal mode structure we can create the dichroism for OAM we elucidated using POVs.

The big difference for LG beams occurs when the winding number of the pump is changed and is illustrated for $m_2 = 0$ in Fig. 5(b), which shows the signal gain G_s (solid line) and net gain G (dashed line) as a function of the signal beam winding number m_1. In contrast to the case of IOVs where changing m_2 would simply shift the gain profile along the m_1 axis (see Fig. 2), the gain profiles in Fig. 5(b) are distinctly different from those in Fig. 5(a). In particular, for the chosen example the signal field experiences absorption for all values of m_1 (we chose the relative phase $\theta = \pi/4$ so that there is absorption at $m_1 = 0$). This arises since the phase-matching condition for peak gain now occurs at $m_1 = 0$, but there is little overlap between the signal and SH fields at that point and therefore little concomitant parametric gain to overcome losses due to second-harmonic generation. The main observation is that for more general signal and pump beam profiles the gain profile depends on the signal and probe winding numbers independently and not just through the OAM difference $\Delta = m_1 - m_2/2$.

V. SUMMARY AND CONCLUSIONS

In summary, we have investigated parametric amplification as a means to produce dichroism based on the orbital angular momentum of an incident signal field. Specifically, we have demonstrated that parametric amplification can be used to create gain for a band of OAM states of an incident signal beam with absorption outside this band. The spiral bandwidth of the gain was shown to depend on beam parameters and the medium length, whereas the peak gain occurs for a signal OAM equal to half that of the pump field and the peak signal gain increases with the pump power. This illustrates that parametric amplification can be used to provide significant gain to a particular sign of the probe OAM, which could in turn be used, for example, to sculpt the OAM content of an incident signal beam or bias the oscillating OAM states in an active system such as a laser. In a similar manner this dichroism could be used to vary the gain for a specific probe OAM dependent on the sign of the OAM of the pump and this could be used for all-optical switching of the probe.

To conclude, we remark that the results in Fig. 5 bear some resemblance to those predicted by Zel'dovich in the early 1970s [14]. More specifically, the Zel'dovich effect involves light scattering from an absorbing cylinder. If the cylinder is not rotating then a probe field incident radially onto it will suffer some absorption. Zel'dovich showed that if the cylinder is rotating then the probe can experience gain over a range of probe winding numbers, the required energy coming from the energy that needs to be added to sustain the rotation [14,15]. The Zel'dovich effect is therefore another system that can display dichroism for OAM. Another, closely related effect is Penrose superradiance, i.e., amplified scattering waves with angular momentum falling into a rotating black hole [16]. To elucidate the analogy for the parametric amplification system, the role of the cylinder is played by the second-harmonic pump and the role of the probe is played by the signal. In this analogy the probe experiences the refractive-index perturbation induced in the medium by the pump field via the second-order nonlinearity: This perturbation is rotating if $m_2 \neq 0$. More technically, parametric gain around the pump beam ring creates an ergoregion in which energy can be exchanged between fields of differing OAM as dictated by phase matching. Then the results in Fig. 5(b) show that if the cylinder (SH pump) is nonrotating, $m_2 = 0$, the probe is absorbed for all incident winding numbers, as expected for waves impinging on an absorbing, nonrotating cylinder or on a nonrotating black hole. In contrast, when the cylinder (pump beam) is rotating, gain becomes possible. Parametric amplification therefore provides a *nonlinear* analog system for the Zel'dovich effect. It is worth noting the similarities and

differences of the two systems: In the Zel'dovich effect, loss and gain are described by the same *linear* loss coefficient that changes sign depending only on the relative rotation frequencies of the cylinder and probe beam. In the nonlinear parametric amplification system, loss is represented by SHG that funnels energy from the probe into a SH signal that has different OAM with respect to the pump. Gain, on the other hand, is observed when the correct spatial phase relations are imposed between the pump and probe. Orbital angular momentum dichroism due to parametric amplification therefore depends on the phase properties of the probe (as in the Zel'dovich effect) and also of the pump. Notwithstanding this difference, the two processes are intriguingly similar, in that both display dichroism for OAM.

ACKNOWLEDGMENTS

D.F. acknowledges financial support from the European Research Council under the European Unions Seventh Framework Programme No. (FP/2007-2013)/ERC GA 306559 and EPSRC (UK) Grant No. EP/J00443X/1.

APPENDIX: LINEARIZED SIGNAL-IDLER EQUATIONS

The utility of the POV solution introduced in Sec. III A rests on the Rayleigh range $z_R = kW^2/2$ being larger than the medium length L so that the ring width W will vary little under propagation through the medium. Within this approximation, the transverse Laplacian in cylindrical coordinates becomes $\nabla_\perp^2 \to \frac{1}{R^2}\frac{\partial^2}{\partial\phi^2}$, thereby neglecting radial expansion of the ring. Then treating the POV field in the vicinity of the ring radius R as approximately constant over the cross section, $A_j(\rho = R,\phi,z) \approx A_j(\phi,z)$, the field equations (2) may be written along the top of the ring as

$$\frac{\partial A_1}{\partial z} - \frac{i}{2k_1R^2}\frac{\partial^2 A_1}{\partial\phi^2} - i\eta A_2 A_1^* = 0, \tag{A1}$$

$$\frac{\partial A_2}{\partial z} - \frac{i}{4k_1R^2}\frac{\partial^2 A_2}{\partial\phi^2} = 0, \tag{A2}$$

where we have used the undepleted pump beam approximation in Eq. (A2) and ignored the nonlinearity. Next the POV solutions in Eqs. (13) given by

$$A_1(\phi,z) = a_1(z)e^{im_1\phi}e^{-(iz/2k_1)(m_1^2/R^2)} + a_3(z)e^{im_3\phi}e^{-(iz/2k_1)(m_3^2/R^2)}, \tag{A3}$$

$$A_2(\phi,z) = a_2e^{im_2\phi}e^{-(iz/2k_2)(m_2^2/R^2)} \tag{A4}$$

are used to express the propagating fields and note that, given $k_2 = 2k_1$, Eq. (A4) automatically satisfies (A2) with a_2 a constant. Substituting Eqs. (A3) and (A4) into Eq. (A1) and using $m_3 = m_2 - m_1$ yields

$$e^{im_1\phi}e^{-(iz/2k_1)(m_1^2/R^2)}[da_1/dz - i(\eta a_2)a_3^*e^{i\kappa z}] + e^{im_3\phi}e^{-(iz/2k_1)(m_3^2/R^2)}\left[\frac{da_3}{dz} - i(\eta a_2)a_1^*e^{i\kappa z}\right] = 0, \tag{A5}$$

with κ given by Eq. (15). Then setting terms with the same exponential azimuthal variation individually to zero, assuming $m_1 \neq m_3$, yields the linearized signal-idler equations (14).

[1] D. P. Caetano, M. P. Almeida, P. H. Souto Ribeiro, J. A. O. Huguenin, B. Coutinho dos Santos, and A. Z. Khoury, Phys. Rev. A **66**, 041801(R) (2002).

[2] J. A. O. Huguenin *et al.*, J. Mod. Opt. **53**, 647 (2006).

[3] F. Devaux and R. Passier, Eur. Phys. J. D **42**, 133 (2007).

[4] X. Zambrana-Puyalto, X. Vidal, and G. Molina-Terriza, Nat. Commun. **5**, 4922 (2014).

[5] R. W. Boyd, *Nonlinear Optics*, 3rd ed. (Academic, New York, 2008), Chap. 2.

[6] A. S. Ostrovsky, C. Rickenstorff-Parrao, and V. Arrizon, Opt. Lett. **38**, 534 (2013).

[7] M. Chen *et al.*, Opt. Lett. **38**, 4919 (2013).

[8] T. Roger, J. F. Heitz, E. M. Wright, and D. Faccio, Sci. Rep. **3**, 3491 (2013).

[9] K. Dholakia, N. B. Simpson, M. J. Padgett, and L. Allen, Phys. Rev. A **54**, R3742 (1996).

[10] F. M. Miatto, A. M. Yao, and S. M. Barnett, Phys. Rev. A **83**, 033816(R) (2011).

[11] M. McLaren, J. Romero, M. J. Padgett, F. S. Roux, and A. Forbes, Phys. Rev. A **88**, 033818 (2013).

[12] R. Ramírez-Alarcón, H. Crus-Ramírez, and A. B. U'Ren, Laser Phys. **23**, 055204 (2013).

[13] M. D. Fleck and J. A. Fleck, Appl. Opt. **19**, 1154 (1980).

[14] Y. B. Zel'dovich, Pis'ma Zh. Eksp. Teor. Fiz. **14**, 270 (1971) [JETP Lett. **14**, 180 (1971)]; Zh. Eksp. Teor. Fiz. **62**, 2076 (1972) [Sov. Phys. JETP **35**, 1085 (1972)].

[15] Ya. B. Zel'dovich, L. V. Rozhanskii, and A. A. Starobinskii, Izv. Vyssh. Uchebn. Zaved. Radiofiz. **29**, I008 (1986).

[16] R. Penrose, Gen. Relativ. Gravit. **34**, 1141 (2002) [reprinted from Riv. Nuovo Cimento Num. Spez. I, 257 (1969)].

REFERENCES

[1] P. A. Franken, A. E. Hill, C. W. Peters, and G. Weinreich, "Generation of optical harmonics," *Phys. Rev. Lett.*, vol. 7, pp. 118–119, Aug 1961.

[2] K. B. Davis, M. O. Mewes, M. R. Andrews, N. J. van Druten, D. S. Durfee, D. M. Kurn, and W. Ketterle, "Bose-Einstein condensation in a gas of sodium atoms," *Phys. Rev. Lett.*, vol. 75, pp. 3969–3973, Nov 1995.

[3] M. H. Anderson, J. R. Ensher, M. R. Matthews, C. E. Wieman, and E. A. Cornell, "Observation of Bose-Einstein condensation in a dilute atomic vapor," *Science*, vol. 269, pp. 198–201, 07 1995.

[4] C. C. Bradley, C. A. Sackett, J. J. Tollett, and R. G. Hulet, "Evidence of Bose-Einstein condensation in an atomic gas with attractive interactions," *Phys. Rev. Lett.*, vol. 75, pp. 1687–1690, Aug 1995.

[5] C. C. Bradley, C. A. Sackett, and R. G. Hulet, "Bose-Einstein condensation of lithium: Observation of limited condensate number," *Phys. Rev. Lett.*, vol. 78, pp. 985–989, Feb 1997.

[6] P. G. Kevrekidis, D. J. Frantzeskakis, and R. Carretero-González, eds., *Emergent Nonlinear Phenomena in Bose-Einstein Condensates*. Springer, Berlin, Heidelberg, 2008.

[7] B. P. Abbott *et al*, "Observation of gravitational waves from a binary black hole merger," *Phys. Rev. Lett.*, vol. 116, p. 061102, Feb 2016.

[8] L. Pitaevskii, "Vortex lines in an imperfect Bose gas," *Sov. Phys. JETP*, vol. 13, no. 2, pp. 451–454, 1961.

[9] E. P. Gross, "Hydrodynamics of a superfluid condensate," *Journal of Mathematical Physics*, vol. 4, no. 2, 1963.

[10] E. P. Gross, "Structure of a quantized vortex in boson systems," *Il Nuovo Cimento (1955-1965)*, vol. 20, no. 3, pp. 454–477, 1961.

[11] L. Onsager, "Statistical hydrodynamics," *Il Nuovo Cimento*, vol. 6, Supplement 2, p. 279, Mar 1949.

[12] C. J. Pethick and H. Smith, *Bose-Einstein Condensation in Dilute Gases*. Cambridge University Press, Cambridge (second edition), 2008.

[13] R. J. Donnelly, *Quantized Vortices in Helium II*. Cambridge University Press, Cambridge, 1991.

[14] T. W. Neely, E. C. Samson, A. S. Bradley, M. J. Davis, and B. P. Anderson, "Observation of vortex dipoles in an oblate Bose-Einstein condensate," *Phys. Rev. Lett.*, vol. 104, p. 160401, Apr 2010.

[15] M. R. Matthews, B. P. Anderson, P. C. Haljan, D. S. Hall, C. E. Wieman, and E. A. Cornell, "Vortices in a Bose-Einstein condensate," *Phys. Rev. Lett.*, vol. 83, p. 2498, Sep 1999.

[16] K. W. Madison, F. Chevy, W. Wohlleben, and J. Dalibard, "Vortex formation in a stirred Bose-Einstein condensate," *Phys. Rev. Lett.*, vol. 84, p. 806, Jan 2000.

[17] W. J. Kwon, G. Moon, S. W. Seo, and Y. Shin, "Critical velocity for vortex shedding in a Bose-Einstein condensate," *Phys. Rev. A*, vol. 91, p. 053615, May 2015.

[18] W. J. Kwon, S. W. Seo, and Y.-i. Shin, "Periodic shedding of vortex dipoles from a moving penetrable obstacle in a Bose-Einstein condensate," *Phys. Rev. A*, vol. 92, p. 033613, Sep 2015.

[19] E. C. Samson, K. E. Wilson, Z. L. Newman, and B. P. Anderson, "Deterministic creation, pinning, and manipulation of quantized vortices in a Bose-Einstein condensate," *Phys. Rev. A*, vol. 93, p. 023603, Feb 2016.

[20] E. C. C. Samson, *Generating and Manipulating Quantized Vortices in Highly Oblate Bose-Einstein Condensates*. PhD thesis, University of Arizona, 2012.

[21] W. Ketterle, D. S. Durfee, and D. M. Stamper-Kurn, "Making, probing and understanding Bose-Einstein condensates," *eprint arXiv:cond-mat/9904034*, Apr. 1999.

[22] W. Ketterle and D. Stamper-Kurn, "Making, probing and understanding Bose-Einstein condensates," in *Bose-Einstein condensation in atomic gases* (M. Inguscio, S. Stringari, and C. Wieman, eds.), vol. CXL, pp. 67–176, IOS Press, 1999.

[23] M. R. Andrews, C. G. Townsend, H.-J. Miesner, D. S. Durfee, D. M. Kurn, and W. Ketterle, "Observation of interference between two Bose condensates," *Science*, vol. 275, no. 5300, pp. 637–641, 1997.

[24] E. W. Hagley, L. Deng, M. Kozuma, M. Trippenbach, Y. B. Band, M. Edwards, M. Doery, P. S. Julienne, K. Helmerson, S. L. Rolston, and W. D. Phillips, "Measurement of the coherence of a Bose-Einstein condensate," *Phys. Rev. Lett.*, vol. 83, pp. 3112–3115, Oct 1999.

[25] Y.-J. Wang, D. Z. Anderson, V. M. Bright, E. A. Cornell, Q. Diot, T. Kishimoto, M. Prentiss, R. A. Saravanan, S. R. Segal, and S. Wu, "Atom Michelson interferometer on a chip using a Bose-Einstein condensate," *Phys. Rev. Lett.*, vol. 94, p. 090405, Mar 2005.

[26] G. D. McDonald, H. Keal, P. A. Altin, J. E. Debs, S. Bennetts, C. C. N. Kuhn, K. S. Hardman, M. T. Johnsson, J. D. Close, and N. P. Robins, "Optically guided linear Mach-Zehnder atom interferometer," *Phys. Rev. A*, vol. 87, p. 013632, Jan 2013.

[27] H. Müntinga, H. Ahlers, M. Krutzik, A. Wenzlawski, S. Arnold, D. Becker, K. Bongs, H. Dittus, H. Duncker, N. Gaaloul, C. Gherasim, E. Giese, C. Grzeschik, T. W. Hänsch, O. Hellmig, W. Herr, S. Herrmann, E. Kajari, S. Kleinert, C. Lämmerzahl, W. Lewoczko-Adamczyk, J. Malcolm, N. Meyer, R. Nolte, A. Peters, M. Popp, J. Reichel, A. Roura, J. Rudolph, M. Schiemangk, M. Schneider, S. T. Seidel, K. Sengstock, V. Tamma, T. Valenzuela, A. Vogel, R. Walser, T. Wendrich, P. Windpassinger, W. Zeller, T. van Zoest, W. Ertmer, W. P. Schleich, and E. M. Rasel, "Interferometry with Bose-Einstein condensates in microgravity," *Phys. Rev. Lett.*, vol. 110, p. 093602, Feb 2013.

[28] Y. Shin, M. Saba, T. A. Pasquini, W. Ketterle, D. E. Pritchard, and A. E. Leanhardt, "Atom interferometry with Bose-Einstein condensates in a double-well potential," *Phys. Rev. Lett.*, vol. 92, p. 050405, Feb 2004.

[29] T. Schumm, S. Hofferberth, L. M. Andersson, S. Wildermuth, S. Groth, I. Bar-Joseph, J. Schmiedmayer, and P. Kruger, "Matter-wave interferometry in a double well on an atom chip," *Nature Physics*, vol. 1, pp. 57–62, 10 2005.

[30] G.-B. Jo, Y. Shin, S. Will, T. A. Pasquini, M. Saba, W. Ketterle, D. E. Pritchard, M. Vengalattore, and M. Prentiss, "Long phase coherence time and number squeezing of two Bose-Einstein condensates on an atom chip," *Phys. Rev. Lett.*, vol. 98, p. 030407, Jan 2007.

[31] G.-B. Jo, J.-H. Choi, C. A. Christensen, T. A. Pasquini, Y.-R. Lee, W. Ketterle, and D. E. Pritchard, "Phase-sensitive recombination of two Bose-Einstein condensates on an atom chip," *Phys. Rev. Lett.*, vol. 98, p. 180401, Apr 2007.

[32] F. Baumgärtner, R. J. Sewell, S. Eriksson, I. Llorente-Garcia, J. Dingjan, J. P. Cotter, and E. A. Hinds, "Measuring energy differences by bec interferometry on a chip," *Phys. Rev. Lett.*, vol. 105, p. 243003, Dec 2010.

[33] M. Lesieur, *Turbulence in fluids*, vol. 40. Springer Science & Business Media, 2012.

[34] A. S. Bradley and B. P. Anderson, "Energy spectra of vortex distributions in two-dimensional quantum turbulence," *Phys. Rev. X*, vol. 2, p. 041001, Oct 2012.

[35] T. W. Neely, A. S. Bradley, E. C. Samson, S. J. Rooney, E. M. Wright, K. J. H. Law, R. Carretero-González, P. G. Kevrekidis, M. J. Davis, and B. P. Anderson, "Characteristics of two-dimensional quantum turbulence in a compressible superfluid," *Phys. Rev. Lett.*, vol. 111, p. 235301, Dec 2013.

[36] B. P. Anderson and P. Meystre, "Nonlinear atom optics," *Contemporary Physics*, vol. 44, no. 6, pp. 473–483, 2003.

[37] C. V. Raman, "The Angular Momentum of Light.," *Nature*, vol. 128, no. 3230, pp. 545–545, 1931.

[38] J. H. Poynting, "The wave motion of a revolving shaft, and a suggestion as to the angular momentum in a beam of circularly polarised light," *Proceedings of the Royal Society of London A: Mathematical, Physical and Engineering Sciences*, vol. 82, no. 557, pp. 560–567, 1909.

[39] R. A. Beth, "Mechanical detection and measurement of the angular momentum of light," *Phys. Rev.*, vol. 50, pp. 115–125, Jul 1936.

[40] J. Vaughan and D. Willetts, "Interference properties of a light beam having a helical wave surface," *Optics Communications*, vol. 30, no. 3, pp. 263 – 267, 1979.

[41] F. Chevy, K. W. Madison, and J. Dalibard, "Measurement of the angular momentum of a rotating Bose-Einstein condensate," *Phys. Rev. Lett.*, vol. 85, p. 2223, Sep 2000.

[42] K. Madison, F. Chevy, W. Wohlleben, and J. Dalibard, "Vortices in a stirred Bose-Einstein condensate," *J. Mod. Opt.*, vol. 47, p. 2715, Nov 2000.

[43] J. R. Abo-Shaeer, C. Raman, J. M. Vogels, and W. Ketterle, "Observation of vortex lattices in Bose-Einstein condensates," *Science*, vol. 292, p. 476, Apr 2001.

[44] C. Raman, J. R. Abo-Shaeer, J. M. Vogels, K. Xu, and W. Ketterle, "Vortex nucleation in a stirred Bose-Einstein condensate," *Phys. Rev. Lett.*, vol. 87, p. 210402, Nov 2001.

[45] E. Hodby, G. Hechenblaikner, S. A. Hopkins, O. M. Maragò, and C. J. Foot, "Vortex nucleation in Bose-Einstein condensates in an oblate, purely magnetic potential," *Phys. Rev. Lett.*, vol. 88, p. 010405, Dec 2001.

[46] D. R. Scherer, C. N. Weiler, T. W. Neely, and B. P. Anderson, "Vortex formation by merging of multiple trapped Bose-Einstein condensates," *Phys. Rev. Lett.*, vol. 98, p. 110402, Mar 2007.

[47] C. N. Weiler, T. W. Neely, D. R. Scherer, A. S. Bradley, M. J. Davis, and B. P. Anderson, "Spontaneous vortices in the formation of Bose-Einstein condensates," *Nature*, vol. 455, p. 948, Oct 2008.

[48] D. V. Freilich, D. Bianchi, A. M. Kaufman, T. K. Langin, and D. S. Hall, "Real-time dynamics of single vortex lines and vortex dipoles in a Bose-Einstein condensate," *Science*, vol. 329, p. 1182, Sep 2010.

[49] G. E. Marti, *Scalar and Spinor Excitations in a Ferromagnetic Bose-Einstein Condensate*. PhD thesis, University of California, Berkeley, 2014.

[50] T. W. Neely, A. S. Bradley, E. C. Samson, S. J. Rooney, E. M. Wright, K. J. H. Law, R. Carretero-González, P. G. Kevrekidis, M. J. Davis, and B. P. Anderson, "Characteristics of two-dimensional quantum turbulence in a compressible superfluid," *Phys. Rev. Lett.*, vol. 111, p. 235301, Dec 2013.

[51] W. J. Kwon, G. Moon, J.-y. Choi, S. W. Seo, and Y.-i. Shin, "Relaxation of superfluid turbulence in highly oblate Bose-Einstein condensates," *Phys. Rev. A*, vol. 90, p. 063627, Dec 2014.

[52] S. Moulder, S. Beattie, R. P. Smith, N. Tammuz, and Z. Hadzibabic, "Quantized supercurrent decay in an annular Bose-Einstein condensate," *Phys. Rev. A*, vol. 86, p. 013629, Jul 2012.

[53] K. C. Wright, R. B. Blakestad, C. J. Lobb, W. D. Phillips, and G. K. Campbell, "Driving phase slips in a superfluid atom circuit with a rotating weak link," *Phys. Rev. Lett.*, vol. 110, p. 025302, Jan 2013.

[54] K. J. H. Law, T. W. Neely, P. G. Kevrekidis, B. P. Anderson, A. S. Bradley, and R. Carretero-González, "Dynamic and energetic stabilization of persistent currents in Bose-Einstein condensates," *Phys. Rev. A*, vol. 89, p. 053606, May 2014.

[55] Z. Hadzibabic, P. Kruger, M. Cheneau, B. Battelier, and J. Dalibard, "Berezinskii-Kosterlitz-Thouless crossover in a trapped atomic gas," *Nature*, vol. 441, p. 1118, Jun 2006.

[56] R. Desbuquois, L. Chomaz, T. Yefsah, J. Leonard, J. Beugnon, C. Weitenberg, and J. Dalibard, "Superfluid behaviour of a two-dimensional Bose gas," *Nature Physics*, vol. 8, pp. 645–648, 09 2012.

[57] J.-y. Choi, S. W. Seo, and Y.-i. Shin, "Observation of thermally activated vortex pairs in a quasi-2d Bose gas," *Phys. Rev. Lett.*, vol. 110, p. 175302, Apr 2013.

[58] K. E. Wilson, *Developing a Toolkit for Experimental Studies of Two- Dimensional Quantum Turbulence in Bose-Einstein Condensates*. 2015.

[59] A. C. White, C. F. Barenghi, and N. P. Proukakis, "Creation and characterization of vortex clusters in atomic Bose-Einstein condensates," *Phys. Rev. A*, vol. 86, p. 013635, Jul 2012.

[60] M. T. Reeves, T. P. Billam, B. P. Anderson, and A. S. Bradley, "Inverse energy cascade in forced two-dimensional quantum turbulence," *Phys. Rev. Lett.*, vol. 110, p. 104501, Mar 2013.

[61] T. P. Billam, M. T. Reeves, B. P. Anderson, and A. S. Bradley, "Onsager-Kraichnan condensation in decaying two-dimensional quantum turbulence," *Phys. Rev. Lett.*, vol. 112, p. 145301, Apr 2014.

[62] Princeton Instruments Imaging Group, *PIXIS: 1024 Datasheet*, 2012.

[63] Photometrics, *Cascade 512B Datasheet*.

[64] A. L. Gaunt, T. F. Schmidutz, I. Gotlibovych, R. P. Smith, and Z. Hadzibabic, "Bose-Einstein condensation of atoms in a uniform potential," *Phys. Rev. Lett.*, vol. 110, p. 200406, May 2013.

[65] W. Schottky, "Aber spontane stromschwankungen in verschiedenen elektrizittsleitern," *Annalen der Physik*, vol. 362, no. 23, pp. 541–567, 1918.

[66] QImaging, *EMCCD Technical Note*.

[67] Andor, *Sensitivity of CCD cameras*.

[68] H. Nyquist, "Certain Topics in Telegraph Transmission Theory," vol. 90, no. 2, 2002.

[69] C. E. Shannon, "Communication in the Presence of Noise," *Proceedings of the IRE*, vol. 37, no. 1, pp. 10–21, 1949.

[70] V. Kotelnikov, "On the transmission capacity of the 'ether' and of cables in electrical communications," pp. 1–23, 1933.

[71] D. Gabor, "Theory of communication. Part 1: The analysis of information," *Journal of the Institution of Electrical Engineers-Part III: Radio and Communication Engineering*, vol. 93, no. 26, pp. 429–441, 1946.

[72] M. R. Andrews, M.-O. Mewes, N. J. van Druten, D. S. Durfee, D. M. Kurn, and W. Ketterle, "Direct, nondestructive observation of a Bose condensate," *Science*, vol. 273, no. 5271, pp. 84–87, 1996.

[73] M. Pappa, P. C. Condylis, G. O. Konstantinidis, V. Bolpasi, A. Lazoudis, O. Morizot, D. Sahagun, M. Baker, and W. von Klitzing, "Ultra-sensitive atom imaging for matter-wave optics," *New Journal of Physics*, vol. 13, no. 11, p. 115012, 2011.

[74] K. E. Wilson, Z. L. Newman, J. D. Lowney, and B. P. Anderson, "*In situ* imaging of vortices in Bose-Einstein condensates," *Phys. Rev. A*, vol. 91, p. 023621, Feb 2015.

[75] M. Gajdacz, P. L. Pedersen, T. Mrch, A. J. Hilliard, J. Arlt, and J. F. Sherson, "Non-destructive faraday imaging of dynamically controlled ultracold atoms," *Review of Scientific Instruments*, vol. 84, no. 8, 2013.

[76] J. W. Goodman, *Introduction to Fourier optics*. Roberts and Company Publishers, 2005.

[77] Thorlabs. V-Coating Specifications: Coating code 780nm.

[78] M. D. Feit and J. A. Fleck, "Computation of mode properties in optical fiber waveguides by a propagating beam method," *Appl. Opt.*, vol. 19, pp. 1154–1164, Apr 1980.

[79] K. K. Das, "Highly anisotropic Bose-Einstein condensates: Crossover to lower dimensionality," *Phys. Rev. A*, vol. 66, p. 053612, Nov 2002.

[80] S. J. Rooney, P. B. Blakie, B. P. Anderson, and A. S. Bradley, "Suppression of Kelvon-induced decay of quantized vortices in oblate Bose-Einstein condensates," *Phys. Rev. A*, vol. 84, p. 023637, Aug 2011.

[81] E. C. Samson, K. E. Wilson, Z. L. Newman, and B. P. Anderson, "Deterministic creation, pinning, and manipulation of quantized vortices in a Bose-Einstein condensate," *Phys. Rev. A*, vol. 93, p. 023603, Feb 2016.

[82] E. M. Wright, *Unviersity of Arizona Optical Sciences 550 Course Notes*. 2015.

[83] D. Yan, R. Carretero-González, D. J. Frantzeskakis, P. G. Kevrekidis, N. P. Proukakis, and D. Spirn, "Exploring vortex dynamics in the presence of dissipation: Analytical and numerical results," *Phys. Rev. A*, vol. 89, p. 043613, Apr 2014.

[84] A. S. Bradley, C. W. Gardiner, and M. J. Davis, "Bose-Einstein condensation from a rotating thermal cloud: Vortex nucleation and lattice formation," *Phys. Rev. A*, vol. 77, p. 033616, Mar 2008.

[85] C. A. Jones and P. H. Roberts, "Motions in a Bose condensate: Axisymmetric solitary waves," *Journal of Physics A: Mathematical and General*, vol. 15, no. 8, p. 2599, 1982.

[86] R. Grimm, M. Weidemüller, and Y. B. Ovchinnikov, "Optical Dipole Traps for Neutral Atoms," *Advances in Atomic Molecular and Optical Physics*, vol. 42, pp. 95–170, 2000.

[87] B. E. Schultz, *Measurement of the rubidium D2 natural transition linewidth*. PhD thesis, York University, 2010.

[88] E. C. C. Samson, *Generating and Manipulating Quantized Vortices in Highly Oblate Bose-Einstein Condensates*. 2012.

[89] A. S. Bradley, S. J. Rooney, and R. G. McDonald, "Low-dimensional stochastic projected Gross-Pitaevskii equation," *Phys. Rev. A*, vol. 92, p. 033631, Sep 2015.

[90] C. W. Gardiner and M. J. Davis, "The stochastic Gross-Pitaevskii equation," *Journal of Physics B: Atomic, Molecular and Optical Physics*, vol. 36, no. 23, p. 4731, 2003.

[91] G. Volovik, "On the Kelvin-Helmholtz instability in superfluids," *JETP Letters*, vol. 75, pp. 418–422, 2002.

[92] R. Blaauwgeers, V. B. Eltsov, G. Eska, A. P. Finne, R. P. Haley, M. Krusius, J. J. Ruohio, L. Skrbek, and G. E. Volovik, "Shear flow and Kelvin-Helmholtz instability in superfluids," *Phys. Rev. Lett.*, vol. 89, p. 155301, Sep 2002.

[93] K. Dholakia, N. B. Simpson, M. J. Padgett, and L. Allen, "Second-harmonic generation and the orbital angular momentum of light," *Phys. Rev. A*, vol. 54, pp. R3742–R3745, Nov 1996.

[94] T. Roger, J. J. F. Heitz, E. M. Wright, and D. Faccio, "Non-collinear interaction of photons with orbital angular momentum," *Scientific Reports*, vol. 3, p. 3491, 12 2013.

[95] T. Roger, J. Heitz, J. Lowney, E. Wright, and D. Faccio, *Spiral phase matching*. Optics InfoBase Conference Papers, Optical Society of America, 2014.

[96] J. García-García, C. Rickenstorff-Parrao, R. Ramos-García, V. Arrizón, and A. S. Ostrovsky, "Simple technique for generating the perfect optical vortex," *Opt. Lett.*, vol. 39, pp. 5305–5308, Sep 2014.

[97] A. S. Ostrovsky, C. Rickenstorff-Parrao, and V. Arrizón, "Generation of the "perfect" optical vortex using a liquid-crystal spatial light modulator," *Opt. Lett.*, vol. 38, pp. 534–536, Feb 2013.

[98] R. W. Boyd, *Nonlinear Optics, Third Edition*. Academic Press, 3rd ed., 2008.

[99] S. Fu, S. Zhang, T. Wang, and C. Gao, "Measurement of orbital angular momentum spectra of multiplexing optical vortices," *Opt. Express*, vol. 24, pp. 6240–6248, Mar 2016.

[100] C.-S. Guo, S.-J. Yue, and G.-X. Wei, "Measuring the orbital angular momentum of optical vortices using a multipinhole plate," *Applied Physics Letters*, vol. 94, no. 23, 2009.

[101] G. C. G. Berkhout and M. W. Beijersbergen, "Method for probing the orbital angular momentum of optical vortices in electromagnetic waves from astronomical objects," *Phys. Rev. Lett.*, vol. 101, p. 100801, Sep 2008.

[102] M. Harris, C. A. Hill, P. R. Tapster, and J. M. Vaughan, "Laser modes with helical wave fronts," *Phys. Rev. A*, vol. 49, pp. 3119–3122, Apr 1994.

[103] J. Leach, M. J. Padgett, S. M. Barnett, S. Franke-Arnold, and J. Courtial, "Measuring the orbital angular momentum of a single photon," *Phys. Rev. Lett.*, vol. 88, p. 257901, Jun 2002.

[104] J. Leach, J. Courtial, K. Skeldon, S. M. Barnett, S. Franke-Arnold, and M. J. Padgett, "Interferometric methods to measure orbital and spin, or the total angular momentum of a single photon," *Phys. Rev. Lett.*, vol. 92, p. 013601, Jan 2004.

[105] A. Mair, A. Vaziri, G. Weihs, and A. Zeilinger, "Entanglement of the orbital angular momentum states of photons," *Nature*, vol. 412, pp. 313–316, 07 2001.

[106] This work is licensed under a Creative Commons Attribution 3.0 Unported License. To view a copy of this license, visit http://creativecommons.org/licenses/by/3.0/.

[107] J. Lowney, T. Roger, D. Faccio, and E. M. Wright, "Dichroism for orbital angular momentum using parametric amplification," *Phys. Rev. A*, vol. 90, p. 053828, Nov 2014.

[108] D. P. Caetano, M. P. Almeida, P. H. Souto Ribeiro, J. A. O. Huguenin, B. Coutinho dos Santos, and A. Z. Khoury, "Conservation of orbital angular momentum in stimulated down-conversion," *Phys. Rev. A*, vol. 66, p. 041801, Oct 2002.

[109] J. A. O. Huguenin, M. Martinelli, D. P. Caetano, B. C. dos santos, M. P. Almeida, P. H. S. Ribeiro, P. Nussenzveig, and A. Z. Khoury, "Orbital angular momentum exchange in parametric down conversion," *Journal of Modern Optics*, vol. 53, no. 5-6, pp. 647–658, 2006.

[110] F. Devaux and R. Passier, "Phase sensitive parametric amplification of optical vortex beams," *The European Physical Journal D*, vol. 42, no. 1, pp. 133–137, 2007.

[111] D. J. Richardson, J. M. Fini, and L. E. Nelson, "Space-division multiplexing in optical fibres," *Nature Photonics*, vol. 7, pp. 354–362, 05 2013.

[112] P. J. Roberts, F. Couny, H. Sabert, B. J. Mangan, D. P. Williams, L. Farr, M. W. Mason, A. Tomlinson, T. A. Birks, J. C. Knight, and P. S. Russell, "Ultimate low loss of hollow-core photonic crystal fibres," *Opt. Express*, vol. 13, pp. 236–244, Jan 2005.

[113] C. Brunet, P. Vaity, Y. Messaddeq, S. LaRochelle, and L. A. Rusch, "Design, fabrication and validation of an oam fiber supporting 36 states," *Opt. Express*, vol. 22, pp. 26117–26127, Oct 2014.

[114] R. J. Essiambre and R. W. Tkach, "Capacity trends and limits of optical communication networks," *Proceedings of the IEEE*, vol. 100, pp. 1035–1055, May 2012.

[115] P. P. Mitra and J. B. Stark, "Nonlinear limits to the information capacity of optical fibre communications," *Nature*, vol. 411, pp. 1027–1030, 06 2001.

[116] X. Zambrana-Puyalto, X. Vidal, and G. Molina-Terriza, "Angular momentum-induced circular dichroism in non-chiral nanostructures," *Nature Communications*, vol. 5, 09 2014.

[117] G. L. Eyink and K. R. Sreenivasan, "Onsager and the theory of hydrodynamic turbulence," *Rev. Mod. Phys.*, vol. 78, pp. 87–135, Jan 2006.